PROPOSAL
for a Nosecone Calorimeter (NCC)
for the PHENIX Experiment

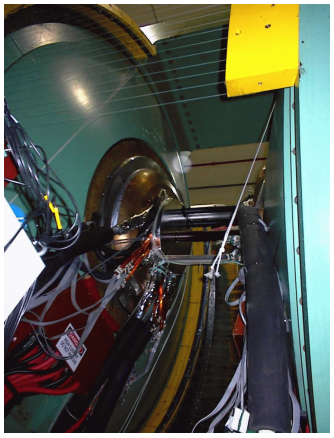
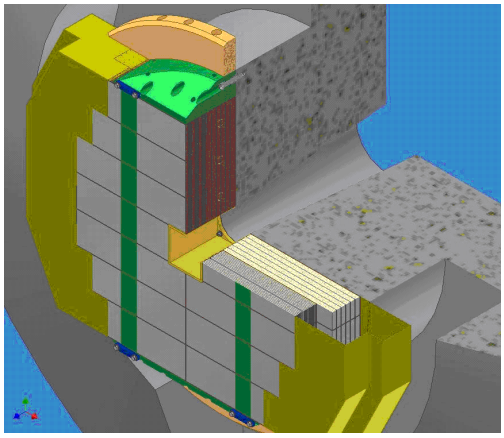

Brookhaven National Laboratory
Relativistic Heavy Ion Collidier
March, 2006

Spokesperson:	William A. Zajc, *Columbia University*
Deputy Spokesperson:	Yasuyuki Akiba, *RIKEN*
Deputy Spokesperson:	Matthias Grosse-Perdekamp, *University of Illinois, Urbana-Champaign*
Operations Manager:	Edward J. O'Brien, *Brookhaven National Laboratory*
Upgrades Manager:	Axel Drees, *Stony Brook University*

PHENIX

PHENIX Nosecone Calorimeter

Participants

February, 2006

Chemistry Dept., Brookhaven National Laboratory, *Upton, NY 11973-5000, USA*
R. Nouicer, R. Pak, A. Sukhanov

Instrumentation Dept., Brookhaven National Laboratory, *Upton, NY 11973-5000, USA*
Z. Li, V. Radeka, S. Rescia

Physics Dept., Brookhaven National Laboratory, *Upton, NY 11973-5000, USA*
S. Boose, B. Johnson, E.P. Kistenev, D. Lynch, S.P. Stoll, C.L. Woody

University of California, *Riverside, CA 92521, USA*
K. Barish, S. Bathe, V. Dzordzhadze, O. Eyser, T. Hester, A. Moreale, Ken Sedgewick, R. Seto, Z. Yasin

Charles University, *Ovocny trh 5, Praha 1, 116 36, Prague, Czech Republic*
Michael Finger, Miroslav Finger, P, Mikes,

University of Colorado, *Boulder, CO 80309, USA*
E. Kinney, J. Nagle

Columbia University and Nevis Laboratories, *Irvington, NY 10 533, USA*
C.Y. Chi

Institute of Physics, Academy of Sciences of Czech Republic, *Na Slovance 2, 182 21 Prague 8, Czech Republic*
J. Popule, L. Tomasek, M. Tomasek, V. Vrba

Czech Technical University, *Zikova 4, 166 36 Prague 6, Czech Republic*
M. Virius, J. Klaus, T. Liska

Ewha Women's University, *Seoul, Korea*
S. Nam, I. Park

FNAL - Fermi National Accelerator Laboratory, *Batavia, IL 60510, USA*
W. E. Cooper, M. Demarteau, M. Hrycyk, K. Krempetz, Y. Orlov

University of Illinois Urbana-Champaign, *Urbana, IL 61801, USA*
M. Chiu, M. Grosse-Perdekamp, J. Koster, J.C. Peng

Iowa State University, *Ames, IA 50011, USA*
J.C. Hill, J.L. Lajoie, F. Wei

Joint Institute for Nuclear Research- Dubna *Moscow Region, Russia*
S. Afanasiev, S. Basilev, A. Baskakov, A. Bychkov, A. Isupov, N. Kotsev, A. Litvinenko, A. Malakhov, V. Peresedov, P. Rukoyatkin, V. Slepnev, I. Slepnev, L. Zolin

Korea University, *Seoul, 136-701, Korea*
B. Hong, B.I. Kim, K.S. Sim

RIKEN, The Institute of Physical and Chemical Research, *Wako, Saitama 351-0198, Japan*
I. Nakagawa, A. Taketani

Skobeltsyn Institute of Nuclear Physics, Lomonosov Moscow State University, *Voro b'evy Gory, Moscow 119992, Russia*
G.A. Bogdanova, D. Karmanov, M. Merkin, V. Volkov, A. Voronin

Dept. of Physics and Astronomy, Stony Brook University, *SUNY, Stony Brook, NY 11794, USA*
A. Deshpande

Institute of Physics, University of Tsukuba, *Tsukuba, Ibaraki 305, Japan*
S. Esumi

Yonsei University, *IPAP, Seoul 120-749, Korea*
J.H. Kang, D.J. Kim, S. Kim

Contents

Chapter 1

Introduction and Executive Summary

Over the first five years of data taking at RHIC, numerous interesting measurements and discoveries have been made. In particular,

- The medium created in gold-gold reactions equilibrates very rapidly on times scales $\leq$2 fm/c as indicated by comparisons of the collective motion of created particles and hydrodynamic model calculations. In fact, these calculations may indicate the medium after equilibration behaves like a nearly perfect liquid (low viscosity). In addition, the initial energy densities are extremely high, perhaps 2 orders of magnitude greater than an ordinary nucleus. The state of matter has been given the name Strongly Interacting Quark Gluon Plasma (sQGP)

- The cold nuclear matter viewed at large virtually may exhibit exciting features of gluon saturation - as described in the color glass condensate framework (CGC).

These conclusions have come from several experimental observations using the initial suite of PHENIX detector subsystems [1, 2].

1. The suppression of high energy particles in central heavy ion collisions at *mid-rapidity* together with the lack of suppression in deuteron nucleus collisions - jet quenching - indicating energy densities of 10-20 GeV/fm^3 - far above the critical energy density predicted by lattice calculations.

2. The large values of elliptic flow - indicating that the initial system thermalizes rapidly and has nearly zero viscosity.

3. The large baryon to meson ratio at moderate values of momentum (several GeV).

4. The suppression of high energy particles at *forward rapidity* in deuteron nucleus collisions.

In addition, the polarized p+p program has made initial steps in the measurement of the gluon contribution to the spin structure of the nucleon.

These observations are currently rather qualitative. Further understanding and discovery will require precision measurements. This will be made possible by an upgrade of the machine luminosity (RHIC II) and significant upgrades of the detectors. The demands of the program require that the unique capabilities of the PHENIX Experiment at RHIC - that is the ability to make precision measurements of leptons and photons - be extended to larger coverage.

We have designed a pair of PHENIX Nosecone Calorimeters (NCC). However, a single NCC will significantly enhance the physics capabilities of the PHENIX detector by extending calorimetric coverage to forward rapidities and increasing the coverage by more than a factor of 10. A key advantage for the NCC is the presence of the muon spectrometer in the forward (and backward) regions. Together with the Forward Silicon vertex Detector, the NCC will make PHENIX a nearly 4π spectrometer, capable of detecting photons, electrons, muons, and hadrons. Our prime motivation is to provide precision measurements of direct photons, π^0s and dielectrons in A+A, p(d)+A, and polarized p+p collisions. The upgrade will provide access to the physics observables that are not currently accessible to PHENIX or are now available only indirectly with very limited accuracy. The primary measurements addressed by the NCC are:

1. The Strongly Interacting Quark Gluon Plasma - Heavy Ion Collisions
   (a) The opacity of the sQGP via studies of γ-jet events
   (b) The suppression of the charmonium and bottomonium states due to screening via measurements of the χ_c and χ_b states
2. The structure of very high energy density cold nuclear matter and the fate of the gluon structure function over a large x-range as a precursor to the sQGP. These studies will be done in p(d)+A Collisions via measurements of
   (a) direct photons and jets
   (b) hadrons (particularly π^0s and ηs)
   (c) dielectrons
3. The spin structure of the nucleon - polarized p+p collisions via
   (a) Direct photons and jets
   (b) hadrons (particularly π^0s and ηs)
   (c) W isolation

The main benefits of the NCC are in the following areas. Firstly, by correctly identifying multiphoton showers in the high position resolution layers built into the calorimeters we will measure π^0 yields at large rapidities thus extending the PHENIX sensitivity to jet quenching studies. Secondly, by increasing acceptance for the direct photons we will make possible the study of correlated photon-jet production, which is a critical process for understanding the Color Glass Condensate and its relevance to initial state modifications in heavy ion collisions. The NCC will extend the measurement of the gluon structure function to low-x values $\approx 10^{-3}$.

Finally, by providing energy measurements within a cone around lepton or photons, the NCC will dramatically improve background conditions for the identification of leptons from W and charm decays, and direct photons, *i.e.* particles being emitted from the initial hard processes being studied.

The NCC replaces the present Copper Nosecones in front of the muon spectrometer. The NCC is a silicon-tungsten sandwich sampling calorimeter, which is longitudinally composed of 3 calorimeter sections read out by Si pads 1.5×1.5 cm^2. In addition there are two precision readout sections readout by strip-pixels at 468 μm pitch. These are located at a depth of 2 and 7 radiation lengths and enable us to identify, and measure π^0s to high energy even when there is an overlap of showers in the pads. This also allows the separation of direct photons and high energy π^0s.

To avoid cost intensive and time consuming R&D, we relied heavily on established technologies and expertise already available in collaborating laboratories. For the calorimeter we propose to use silicon sensors closely resembling those currently in use for prototyping future calorimeter for ILC and a number of cosmic ray experiments. For coordinate detectors we follow the lead of the PHENIX Silicon Vertex Tracker and use pixilated strips with 2-D sensitivity. As a backup to this latter solution we are working with the NUCLON experiment in Russia on implementing standard one-coordinate strip detectors with the identical strip width of 468 μm. We plan to use hybrid preamplifier chips developed at BNL for the ATLAS experiment at CERN as a base solution for signal conditioning in calorimeter and the SVX4 readout chip developed at FNAL to readout the strip detectors.

Over 70 NCC participants from 20 institutions are cooperating to design, construct, install, and operate the NCC. Among these participants are many experts with extensive experience in calorimetry, in silicon detector technology, the design, fabrication and operations of modern readout electronics, mechanical and integration issues, software experts as well as physicists who are well versed in the different aspects of analysis necessary to extract physics from this detector. With the help of institutional contributions, PHENIX was able to maintain a small but well focused effort over the past two years to aid in the design of the detector, and to establish expertise in the relevant technologies.

We propose to construct our NCC detector over a period of three years, U.S. FY08, FY09, and FY10. To carry out this project we seek funding of a total of \$4M through the DOE Office of Nuclear Physics. While the plan is to eventually construct an NCC for both the North and South arms of the PHENIX spectrometer, we propose to initially build only one NCC using funds from the DOE. We are actively working to secure funding for a second NCC from our Japanese and European colleagues, in particular the RIKEN Institute of Japan which is already participating in the R&D effort. In addition, we expect smaller contributions from the Czech Republic and Russia. A majority of the physics topics discussed in this proposal will be addressed using just one NCC. However, there are significant advantages to having two NCC detectors available. These include (a) in p+A collisions - the ability to simultaneously study the proton and the heavy ion side of the collision, (b) in p+p collisions - the ability to provide isolation cuts for W boson physics for the measurement of anti-quark spin, and (c) a factor of 2 in rate for rare processes such as high momentum direct photons and the χ_c.

The structure of this document is detailed in the Table of Contents on pages *iii* to *v*:

- Chapter 2 discusses the physics motivation.
- Chapter 3 presents a detailed description of the NCC and technical aspects of the project.
- Chapter 4 gives a preliminary management plan of the project, including the roles and responsibilities of the participating institutions.
- Chapter 5 shows the Budgets and Schedule.
- Appendix A presents event rate estimates
- Appendix B describes several simulation studies.
- Appendix C gives details on the Silicon Strip Sensors.
- Lists of Figures, Tables, and References conclude the document.

Chapter 2

Physics Overview

The NCC increases the calorimetric coverage of the PHENIX detector to forward and backward rapidities so that the total coverage is increased by more than an order of magnitude. This impacts the entire PHENIX physics program in Å, p(d)+A, and polarized p+pcollisions. This section gives an overview of the physics program relevant to the NCC in each of these three areas. For the study of heavy-ion collisions - the essential questions revolve around our understanding of the sQGP state of matter. High $p_\perp$ photons opposite a jet can be used as a calibrated probe to measure the energy loss of quarks or gluons in the plasma. The yield of charmonium and bottomoniunm states - particularly the χ_c measured in conjunction with the muon spectrometer, will give information on the deconfinement temperatures. The NCC can be used to find the reaction plane with great accuracy, all such signatures can be studied as a function of the geometry of the colliding system. This should lead to very accurate measurements of the energy loss of high momentum partons in the plasma.

As mentioned in the introduction the physics program at the Relativistic Heavy Ion Collider (RHIC) has given us a wealth of new information. The emerging picture is as follows: The initial state of the nucleus relevant to bulk system in AA collisions at RHIC energies is a state of saturated gluons - this has been given the name of a Colored Glass Condensate (CGC). This CGC state allows for a rapid thermalization of the colliding partons forming perfect fluid - that is - a system with viscosity near zero. This system - called the Strongly Interacting Quark Gluon Plasma (sQGP) is almost opaque to high momentum partons and has an energy density 50 times that of normal nuclear matter. These exciting results immediately lead to many questions which demand quantitative answers- among them: a)what is the energy loss mechanism of partons as they traverse this matter. How much energy is lost b) What is the mechanism by which the CGC thermalizes so rapidly? c) Can we explicitly observe the deconfinement of quarks and gluons?

Direct photons, jets, and high momentum particles in polarized $p + p$ collisions are an effective way to make measurements of the gluon spin contribution. In addition transversely polarized protons will give access to the transverse structure functions in of the nucleon. In conjunction with the muon spectrometer the NCC will allow us to make isolation cuts for the study of W bosons to measure anti-quark spin structure functions.

The electromagnetic calorimeter in the central region (EMC) has been a critical element in these discoveries - the strongest and cleanest understanding of the suppression of high

momentum hadrons - i.e. "jet quenching" comes from $\pi^0 s$ measured by the EMC. The demands of the program require that the unique capabilities of the PHENIX Experiment at RHIC - that is the ability to make precision measurements of leptons and photons - be extended to larger coverage.

2.1 Heavy Ion Physics

2.1.1 Hard Scattering

Hard scattered partons are an important probe of the matter created in heavy-ion collisions. Because the hard scattering event occurs early in the evolution of the collisions ($\tau < 1$ fm/c), the scattered partons can be affected by the evolution of the surrounding QCD matter, particularly if this matter passes through a deconfined phase. The scattered partons will be sensitive to the medium primarily through the mechanism of energy loss through medium-induced gluon radiation [3, 4, 5, 6, 7, 8, 9, 10], resulting in a reduction of the energy available to the parton when it fragments into hadrons. This phenomenon was predicted to lead to a suppression of particles with large transverse momentum in heavy-ion collisions at RHIC and this suppression has been quantified by excellent measurements from the first RHIC runs [11, 12, 13, 14]. Measurements in d+Au collisions have demonstrated that the suppression is not due to initial state effects [15].

The four RHIC experiments have measured charged particle spectra from Au+Au collisions at $\sqrt{s_{NN}} = 130$ and 200 GeV, with measurements for unidentified hadrons extending out to $p_T \sim 12$ GeV/c. All of these measurements show a suppression of high transverse momentum hadrons in central collisions when compared to data from p+p collisions (suitably scaled by the number of binary collisions and the energy difference). The PHENIX detector is also capable of reconstructing the decay of the π^0 meson to two photons using the electromagnetic calorimeter in both central arms. Using the measured production of π^0 mesons in both p+p and Au+Au collisions, we can construct a ratio known as the nuclear modification factor R_{AA}:

$$R_{AA} = \frac{dN_{AA}}{< N_{coll} > \times dN_{pp}} \tag{2.1}$$

where dN_{AA} is the differential yield for a point-like process in an AA collision, and dN_{pp} is the differential yield for the same process in nucleon-nucleon collisions. The number of binary collisions for a given centrality class N_{coll} is estimated using a Glauber model of the nuclear overlap. In the naive limit that a nucleus-nucleus collision can be though of as a superposition of independent nucleon-nucleon collisions, the nuclear modification faction at high p_T should be unity. The nuclear modification factor for charged hadrons and neutral pions as measured by the PHENIX collaboration is shown in Figure 2.1. There is a significant suppression of high transverse momentum hadrons observed in Au+Au collisions, consistent with substantial energy loss of the scattered partons. A similar suppression was observed in data taken at $\sqrt{s_{NN}} = 130$ GeV [11]. Models of energy loss that incorporate the expansion of the system indicate the energy loss in the matter created in heavy-ion collisions at RHIC may be as much as fifteen times larger than the energy loss of a comparable parton in ordinary

nuclear matter [16]. Since the energy loss is proportional to the gluon density, this implies the gluon density created in a heavy ion collision is more than an order of magnitude larger than in cold nuclei.

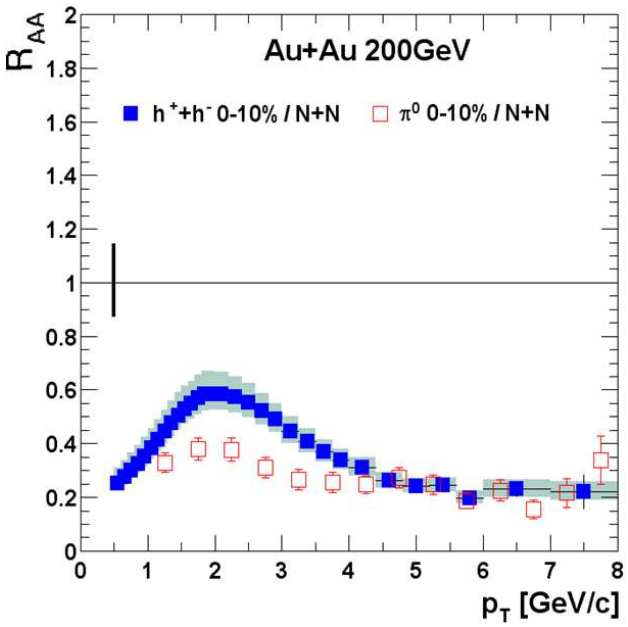

Figure 2.1: (left) $R_A A$ for π_0 mesons and inclusive charged particles from as measured by PHENIX. The difference in the observed suppression for charged hadrons and neutral pions between 1-4 GeV/c is due to the changing particle composition of the charged hadrons, highlighting the importance of pi^0 measurement.

In heavy-ion collisions at RHIC energies direct detection of jets is complicated by large backgrounds from particles in the underlying event. However, jets of hadrons can still be identified using two-particle correlation techniques, which take advantage of the fact that hadrons resulting from a parton cascade will be correlated in azimuthal angle and pseudorapidity. Such techniques make use of the "leading hadron" effect in jet fragmentation, where a single hadron often ends up with a large fraction of the parton momentum. Selecting high transverse momentum hadrons provides a good proxy for the jet direction and momentum. At high-p_T inclusive charged particles can often be subject to background processes that result in a low-p_T particle being reconstructed at high momentum. In contrast, the measurement of π^0 mesons becomes essentially background-free at high-p_T. In addition, at RHIC the particle composition of the inclusive charged measurements change dramatically for transverse momenta between 2 and 5 GeV/c [17], further complicating the physics interpretation.

The PHENIX experiment used the central arm electromagnetic calorimeters (EMCal) to measure π^0 production to very high transverse momentum in a variety of colliding systems. These measurements demonstrated the power of exploiting the measurement of π^0 mesons with an electromagnetic calorimeter in relativistic heavy-ion collisions.

2.1.1.1 Photon-Tagged Jets

The suppression of high-p_T hadrons seen at RHIC is a complicated interplay between the density and time evolution of the created matter, the collision geometry, and the transverse momentum of the probe. Disentangling these effects in such a way as to allow detailed comparisons between theoretical models of energy loss is complicated by the number of factors that affect the suppression observed in the final state. One way to simply the observables is to use jets that are produced in coincidence with photons via a QCD-Compton process (see Figure 2.2). The photon escapes the colored medium essentially unmodified and without undergoing energy loss, and therefore provides a measure of the total energy of its partner jet. The cross-section for such a process is substantially smaller than the full dijet cross section, however, and the detection of direct photons in such an environment is difficult.

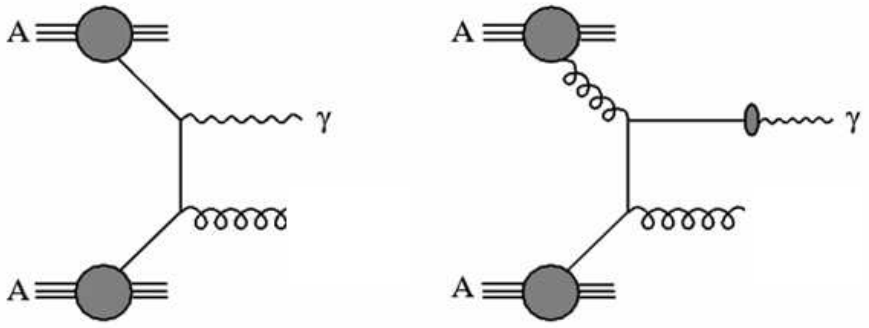

Figure 2.2: Tree level diagrams for the production of direct photons by QCD-Compton processes. The photon produced in the hard scattering only interacts electromagnetically and will escape the surrounding medium produced in nucleus-nucleus collisions without interacting. The jet produced by the partner parton in the interaction will, however, interact and suffer energy loss. Measuring both the photon and jet in the final state allows for a calibration of the energy loss.

Direct photons at mid-rapidity in AuAu collisions at $\sqrt{s_{NN}} = 200$ GeV have already been measured by the PHENIX collaboration, as shown in Figs. 2.3 and 2.4. These initial measurements demonstrate not only the feasibility of measuring direct photons in a heavy-ion environment but the observed scaling with the number of binary collisions indicates that the photons do indeed survive unmodified to the final state. Future studies with photon-tagged jets will allow a detailed, quantitative study of the energy loss suffered by the partner jet, further elucidating the nature of the matter created at RHIC.

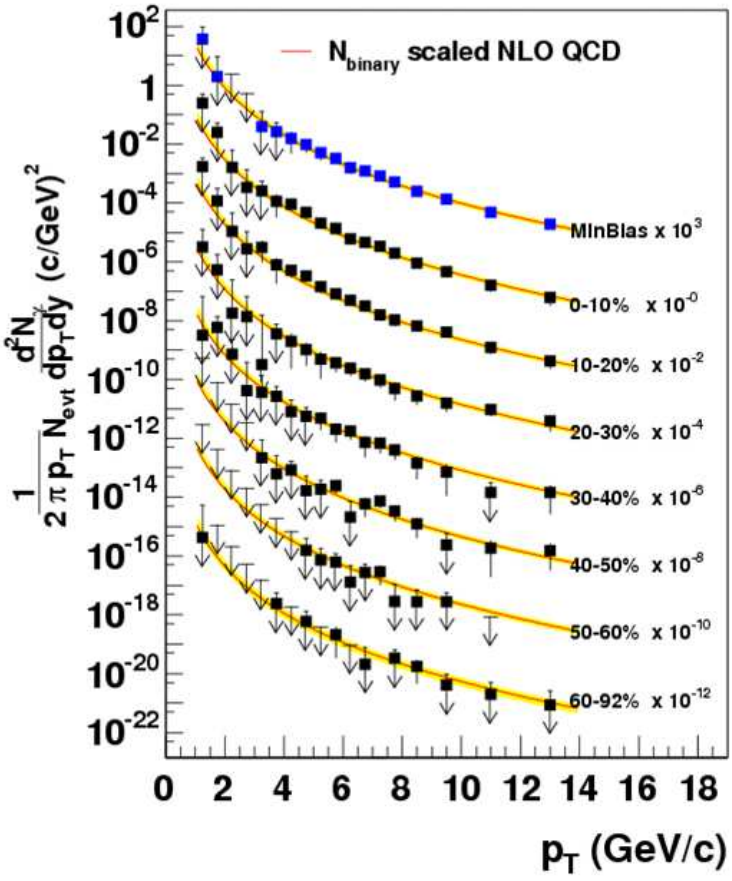

Figure 2.3: Measured direct photon invariant multiplicity at mid-rapidity as a function of centrality in AuAu collisions. R_{AA} for direct photons as a function of transverse momentum.

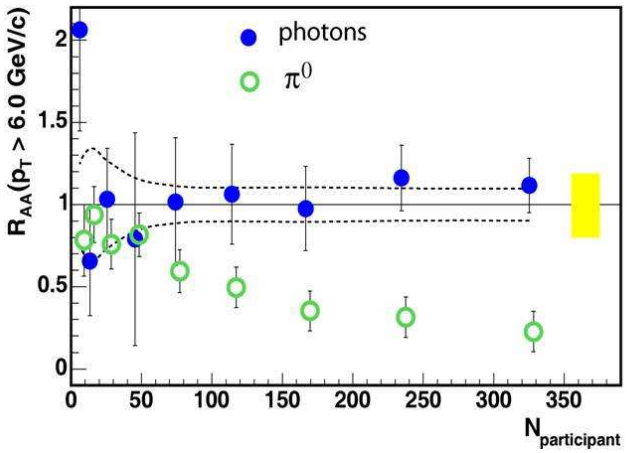

Figure 2.4: R_{AA} for direct photons as a function of transverse momentum.

2.1.1.2 Contribution of the NCC

The NCC would add substantial rapidity coverage to the PHENIX detector for the detection of photons and π_0 mesons, covering $1 < |\eta| < 3$, and increasing the overall coverage PHENIX acceptance about a factor of 10. Jet physics and energy loss studies using both photon-tagged jets as well as leading π_0 mesons will be possible with the NCC. This additional pseudorapidity coverage will allow for the study of physics observables away from central rapidity. Because the effective energy density of the created matter decreases as a function of pseudorapidity, when combined with measurements in the central arms, the NCC observables will provide a robust picture of the created matter for a variety of energy densities within a single colliding system.

2.1.2 Heavy Quarkonia

Heavy quarkonia states are amongst the best probes created in heavy ion collisions for understanding modifications of the interactions amongst partons in the medium - perhaps a quark gluon plasma. The formation of charm-anticharm $c\overline{c}$ and bottom-antibottom $b\overline{b}$ quark pairs occurs on very short time scales given the inverse mass ($t \approx 0.1$ fm/c). A small fraction of the time the pair evolves into a physical bound quarkonia state with a time scale given by the relative momentum of the heavy quarks in the bound state ($t \approx 1$ fm/c). Since charm and bottom quarks have a mass much larger than the expected temperature of the medium, they are only abundantly created in the earliest stage of the nuclear collision. Thus, we can unambiguously ascribe the final yield of heavy quarkonia to how the quarks and antiquarks interact with the surrounding cold and hot nuclear medium between their creation time and the final freeze-out of the system ($t \approx 10$ fm/c).

The original suggestion [18] that color screening in a deconfined medium should lead to a suppression of heavy quarkonia states has evolved significantly over the past 20 years. New evidence from studies of lattice QCD reveal that many of the quarkonia states continue to exist, in modified form, inside the deconfined medium of a quark gluon plasma up to temperatures well beyond the expected 170 MeV transition value [19]. The current state of the art in lattice QCD yields a somewhat ambiguous picture where considerations of free energy give a different melting point for quarkonia than studies of the spectral functions [20, 21]. However, it is common amongst the pictures that the more weakly bound ψ' and χ_c should be modified and melt at a lower temperature compared with the J/ψ and Υ states. This is shown from two different calculations in Table 2.1 [22]. The sequential suppression expected as one increases the temperature of the medium is shown in Figure 2.5 [23].

Particular interest in the χ_c state, in addition to the J/ψ, is twofold. First, in the different lattice calculations is a likely that the χ_c and J/ψ states span the binding energy range where one of the states at least will have some color screening effects. Second, it is expects from hadron-hadron and hadron-nucleus measurements that of order 40% of the reconstructed J/ψ are from χ_c decay feeddown. Thus, the measurement of both states is likely necessary to disentangle various effects and extract the fundamental physics from this probe.

There are three P wave quarkonia states ($\chi_{c1}, \chi_{c2}, \chi_{c3}$) all of which can decay via $\chi_c \longrightarrow \gamma J/\psi$, though only the first two have appreciable branching fractions, 0.27 and

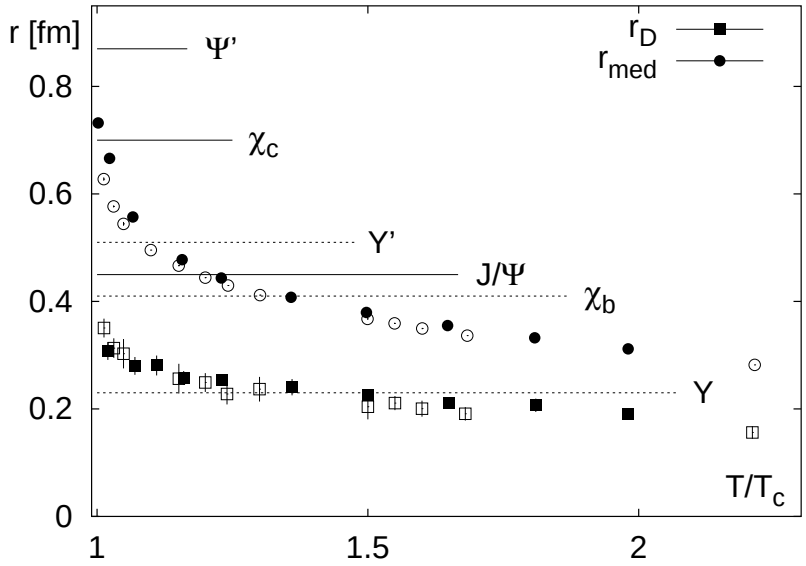

Figure 2.5: The scale r_{med} which gives an estimate for the distance beyond which the force between a static quark anti-quark pair is strongly modified by temperature effects and the Debye screening radius, $R_D = 1/m_D$. Open (closed) symbols correspond to SU(3) (2-flavor QCD) calculations. The horizontal lines give the mean squared charge radii of some charmonium and bottomonium states.

Table 2.1: Dissociation temperatures obtained from different analyses in quenched QCD.

Heavy Quarkonium	$U^{(1)}_{Q\bar{Q}}(\mathbf{r},T)$ Potential	$F_1(\mathbf{r},T)$ Potential	$U_1(\mathbf{r},T)$ Potential	Spectral Analysis
$J/\psi, \eta_c$	$1.62\,T_c$	$1.40\,T_c$	$2.60\,T_c$	$\sim 1.6\,T_c$
χ_c	unbound in QGP	unbound in QGP	$1.19\,T_c$	dissolved below $1.1\,T_c$
ψ', η_c'	unbound in QGP	unbound in QGP	$1.20\,T_c$	
Υ, η_b	$4.10\,T_c$	$3.50\,T_c$	$\sim 5.0\,T_c$	
χ_b	$1.18\,T_c$	$1.10\,T_c$	$1.73\,T_c$	
Υ', η_b'	$1.38\,T_c$	$1.19\,T_c$	$2.28\,T_c$	

0.17 respectively. The PHENIX experiment currently measures the J/ψ away from mid-rapidity via reconstruction of the two decay muons, and needs to add the capability to measure the associated photon. The photon from the radiative decay of the χ_c has a small relative momentum to that of its parent and therefore the proposed nosecone calorimeter has good acceptance (58%) for γ when the J/ψ is accepted into the existing PHENIX forward

spectrometer. In addition, due to the forward rapidity of these χ_c, the photon is boosted and can have an appreciable momentum.

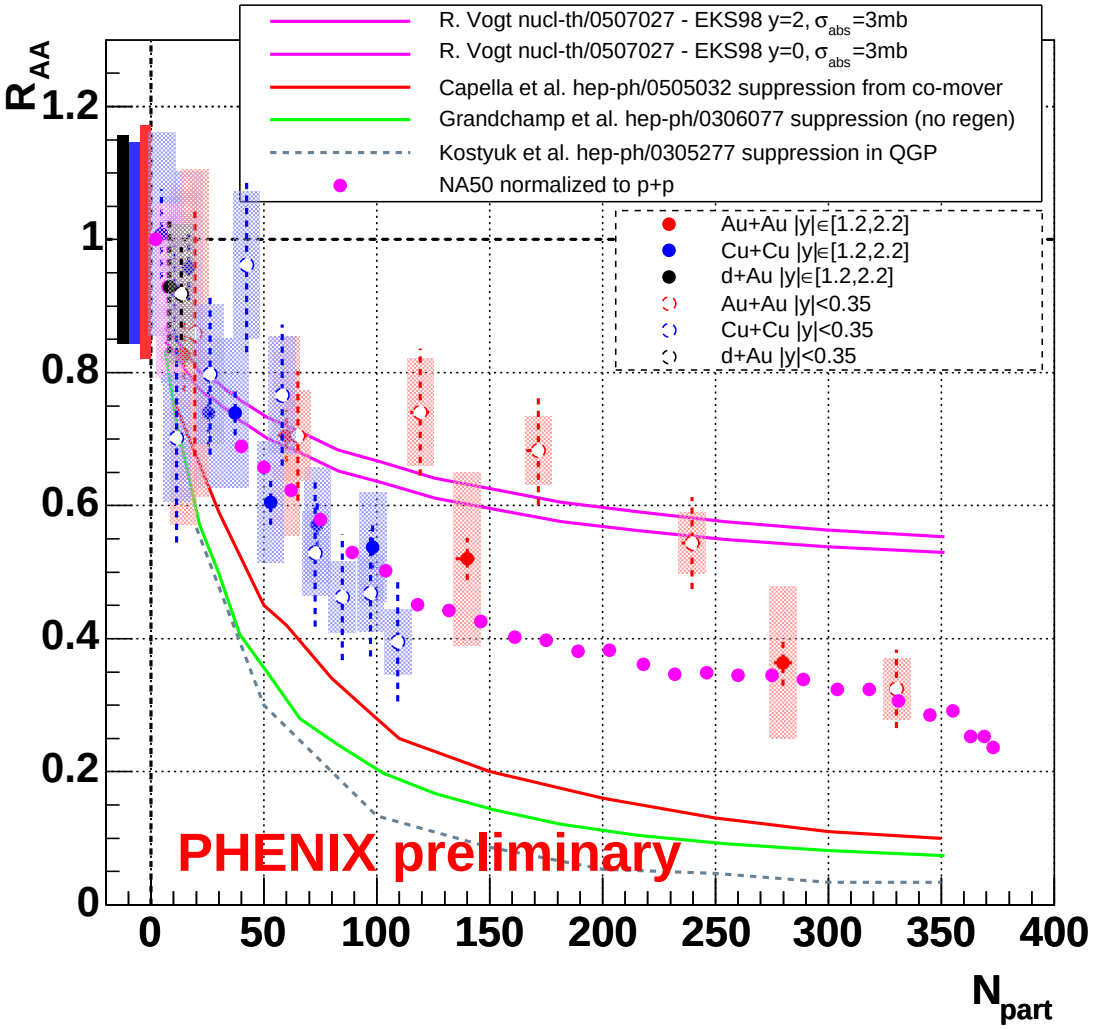

Figure 2.6: PHENIX Preliminary R_{AA} for J/ψ in $Au+Au$ and $Cu+Cu$ 200 GeV reactions.

The first statistically significant results on heavy quarkonia in heavy ion collisions at RHIC come from the PHENIX experiment [24]. Although the results are currently in preliminary form, a very striking and perhaps surprising observation has been made. As shown in the figure below, the nuclear suppression factor is quite similar at RHIC energies as the results from the NA50 and NA60 experiments [25, 26] at the CERN-SPS, almost an order of magnitude lower in collision energy. Most model calculations of expected J/ψ production, whether via color screening or co-mover absorption, predicted a substantially larger suppression at RHIC due to the higher energy density and also higher temperature. In fact, there

were many predictions that the J/ψ might be so suppressed as to make any observation difficult, and thus turning the focus to the more tightly bound and thus less suppression Υ(1s) state. However, this new experimental information, drives us to make precision measurements not just of the more tightly bound states, but the less tightly bound χ_c and ψ'.

2.1.3 Charm via Electrons

Further PHENIX upgrades include a silicon vertex detector with coverage matching that of the forward muon spectrometer. With the additional capability to statistically tag displaced vertices's, we greatly extend our ability to measure charm and bottom via single muon semi-leptonic decays by rejecting much longer lifetime muon backgrounds from pion and kaons decays. Additionally, one can then separate J/ψ contributions from B meson decay. Putting this information from the forward silicon detector with the nosecone calorimeter, may allow for the tagging of forward rapidity electrons which has a displaced vertex. In principle, one can then separate the charm and bottom semi-leptonic decay electrons from the very prompt Dalitz decays and conversions. This could be complementary to the single muon program. In reality the kinematic coverage for both is limited by the coverage of the silicon detector and both measure essentially the same thing with quite different kinematics.

We note that with a limited number of layers in the silicon detector, significant detailed studies on whether a clean electron sample can be obtained in proton-proton or heavy ion reactions must be completed.

2.2 p+A Physics, Nucleon Structure, and Saturation

A system of very low viscosity is formed very early (t $\approx$ 1 fm/c) in the collisions of heavy ions. As mentioned above, pQCD calculations predict thermalization times longer than this. How then, can the system thermalize so quickly? An exciting new development has emerged, in that non-perturbative methods of calculating the early stages of such collisions are now available in a formulation often referred to as the Colored Glass Condensate. Such calculations indicate that the low-x partons in nuclear collisions are packed together such that their nuclear wavefunctions overlap and saturation occurs - thereby distorting the wavefunctions. It is precisely these low-x partons which lead to the formations of most of the low momentum partons in a RHIC collisions which make up the dense sQGP. Various ideas have been formulated which allow for the thermalization of the system starting from the CGC. [27, 28, 29, 30]

The NCC upgrade will offer many exciting new opportunities for the study of this regime by studying p(d)+A collisions. It is important to note that the c.m. energy at RHIC is more than a factor of 5 greater than any existing fixed-target experiments. This fact, together with the forward rapidity acceptance of the NCC makes accessible kinematic regions not accessible before - in particular - the low-x region where CGC calculations are applicable.

In the following we briefly discuss the CGC model and measurements which have been made by the present PHENIX detector. It will be made clear why the measurement of

the CGC must be made in the forward rapidity region. In addition, several other topics of interest in pA collisions will be discussed.

2.2.1 The Colored Glass Condensate

Recently, Mclerran and his collaborators [31, 32, 33] have used a classical approximation for the initial stage of a heavy ion collision, arguing that the occupation numbers at low x where much of the particle production occurs are rather high (see Fig. 2.7). This model - which they have named the "Colored Glass Condensate"- shows the phenomenon of gluon saturation and makes predictions which can be used to calculate the initial conditions in a heavy ion collision which in turn can then be used as input to the hydrodynamical calculations. This calculation relies on the fact that very early in the collision, gluon saturation effects at low x set a value of Q$\sim$Q$_S$ where α_S can be considered small but the occupation numbers are high. The value of Q_S at RHIC is 1-2 GeV so $\alpha_S^2 \sim \frac{1}{10}$. Fig. 2.8 shows the region of of x and Q where this saturation should take place. The saturation assumed by these authors is present in the initial state before the nuclei collide. Hence the study of proton-nucleus collisions will be important in distinguishing these effects, from final state effects such as the formation of a quark-gluon plasma.

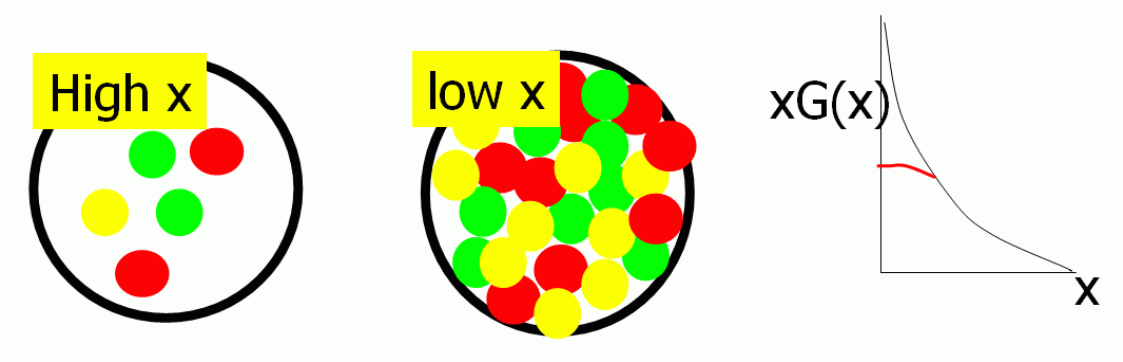

Figure 2.7: A schematic showing the saturation of the gluons at low-x. This has the effect of suppressing very low x gluons and pushing them to higher-x

Such an effect is consistent with electron-proton collisions at HERA [34]. In a heavy ion collision, the nucleus acts as an amplifier of the effect because of the the thickness of the nucleus. Saturation effects which in a proton would be at x 10^{-4} would show up in pA collisions at x 10^{-2}. Investigations of CGC signals use the fact that in going to forward rapidities, one begins to sample a lower range in x in the nucleus.

The ratio

$$R_{CP} = \frac{Yield(central)/N_{coll}(Central)}{Yield(peripheral)/N_{coll}(Peripheral)} \tag{2.2}$$

is a measure of the yield per collision from hard processes coming from central as compared to peripheral collisions, where the peripheral collisions are taken as a baseline. If pp data is available, it is often used as the baseline as will be done later in the definition of R$_{AA}$.

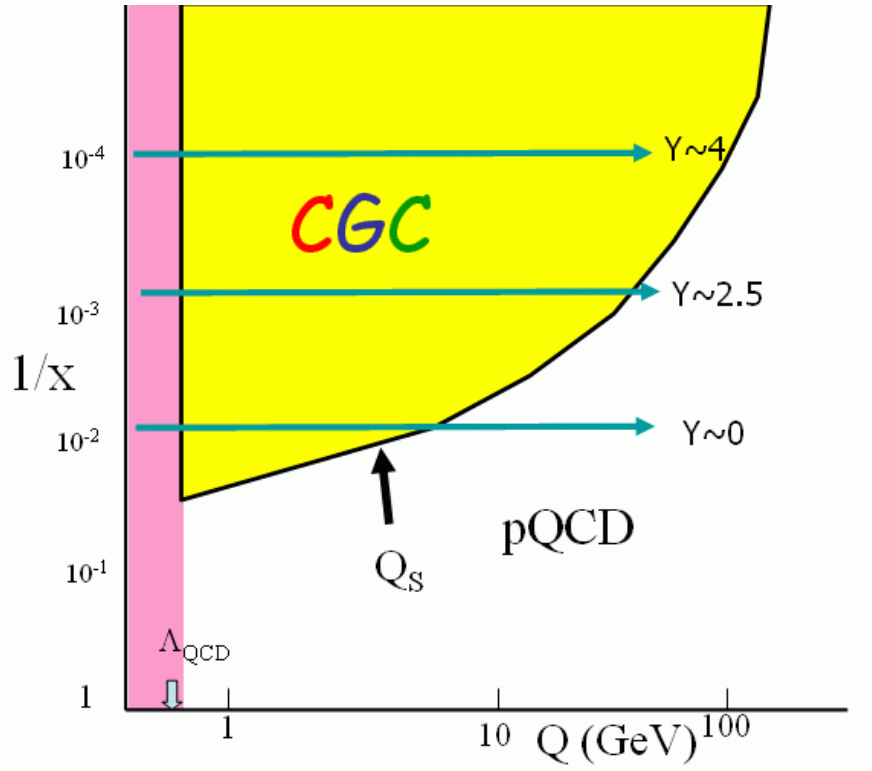

Figure 2.8: Regions of the nucleus showing the CGC region bordered by a line representing Q_S. As one goes forward in rapidity to regions covered by the NCC, one crosses into the CGC region.

Using punch-through hadrons identified in the muon spectrometer PHENIX looked at this ratio in deuteron-nucleus collisions. For a given p_T, a lower and lower value of x is sampled as one moves to higher rapidity. Since the gluon structure function increases at low x one would see a stronger suppression as one moves to higher rapidity. Fig. 2.9 shows just this effect, with the more central collisions showing a larger suppression. One interesting fact is that in the backward rapidity region, a strong enhancement is shown.

2.2.1.1 Contribution of the NCC

The NCC will be directly sensitive to the gluon structure function (or what is taken for a structure function in the CGC model) over a large region of x and Q^2 allowing measurements both inside and outside the saturation regions shown in Fig. 2.8. At midrapidity in central heavy ion collisions, there is a clear difference between the suppression of direct photons and hadrons (see Figure B.1). This was clear sign that the suppression was due primarily to final state interactions - the sQGP; and not due to the initial state - the CGC. By contrast, for central pA collisions , neither hadrons nor direct photons, show suppression at midrapidity. As just mentioned, in the forward rapidity region, hadrons do show a suppression in pA collisions fig. 2.9. One important test is to look at direct photons. If the suppression is due

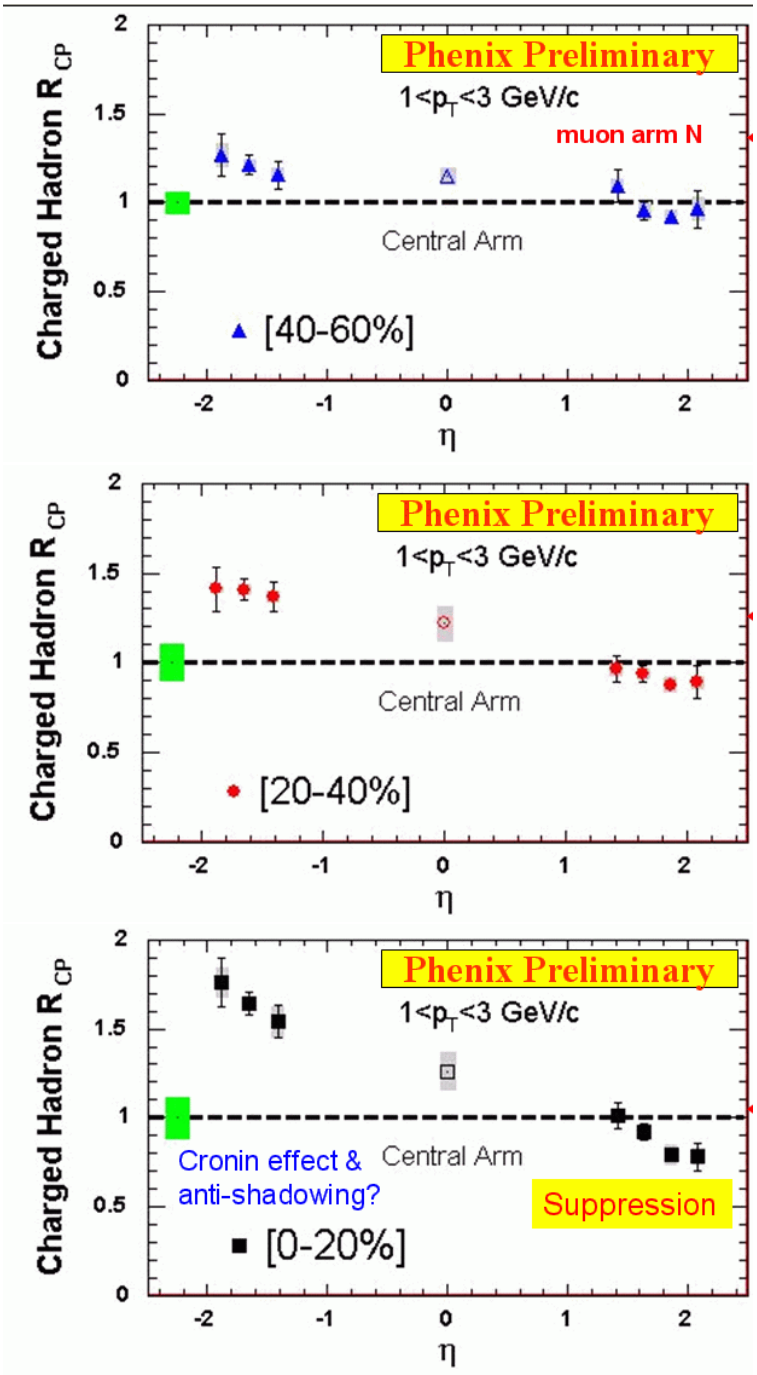

Figure 2.9: R_{CP} for charged hadrons as measured in by the PHENIX muon arms for different centralities.

to the initial state - that is the CGC - direct photons should also show a suppression. (See appendix C for a simulation of this effect.) By charting out the suppression vs centrality and rapidity the NCC will be able to map out the saturation regions shown in figure Fig. 2.8.

The following is a list of many interesting channels in the forward rapidity regions which are sensitive to gluon distributions which are accessible to the NCC. These channels include:

1. Single hadron production. Several hadrons can be readily detected by NCC via their decays to lepton/photon channels. The hadrons and their relevant decay channels include $\pi^0 \to \gamma\gamma$, $\eta \to \gamma\gamma$, $\omega \to \pi^0\gamma$, $\phi \to e^+e^-$, $J/\Psi \to e^+e^-$, $\Psi' \to e^+e^-$, $\chi_c \to \gamma J/\Psi$ followed by $J/\Psi \to e^+e^-$, and $\Upsilon \to e^+e^-$. The p-A data at forward rapidity region on the production of these particles would significantly enhance the physics reach of PHENIX which is currently limited to heavy quarkonium and punch-through hadrons.

2. Direct photon and jet production. The inclusive production of direct photons at forward rapidity is sensitive to the gluon distribution. Moreover, a measurement of direct photon in coincidence with a jet would be very valuable since the kinematic variables of the gluons can be readily reconstructed.

3. Dihadron production. The nosecone calorimeters will greatly extend the kinematic coverage for detecting dihadrons. A hadron such as π^0 or η could be detected in the NCC, while the other hadron could be measured by the barrel detectors. Energetic dihadrons would correspond largely to leading particles from dijet events, and can provide independent information on the gluon distributions in nuclei at small x.

4. Open charm and beauty production. In conjunction with the Forward Silicon Tracker, the NCC can be used to measure D and B meson productions via their semi-leptonic decays ($D \to eX$ and $B \to eX$). These heavy-quark productions are sensitive to gluon distributions. Furthermore, the acceptance for detecting a pair of charmed particle through their semileptonic decays is significantly enhanced when the NCC is combined with the muon spectrometers ($D \to eX$ in coincidence with $D \to \mu X$).

2.2.2 Other Physics Topics

2.2.2.1 Antiquark Distribution in Nuclei at Small x

In addition to the study of the CGC, other topics can also be addressed in pA collisions in the forward rapidity region. In the past decade, nuclear shadowing at small x − has been very well characterized experimentally in DIS [35]. The experimental signature is that the DIS cross section ratio falls below unity for $x \leq 0.08$. Theoretically, shadowing has been studied extensively in the past 10 years [36].

Shadowing is also expected in hadronic processes. To date, the only experimental evidence for shadowing in hadronic reactions is the reduction in the nuclear dependence seen in the Drell-Yan experiments E772 [37] and E866 [38]. The lowest x covered in these experiments is $x = 0.04$, just below the onset of shadowing effect.

Shadowing in the $p + A$ Drell-Yan process is largely due to antiquarks in the nucleus, unlike in DIS, where quarks dominate for most of the explored region. Although shadowing effects are expected for antiquarks and gluons, there is no known requirement that they be identical [39] to those for quarks. There exists no experimental information on the antiquark shadowing at small x ($x < 0.04$). The coverage in x_2 will be significantly extended at RHIC. In particular, the lowest x_2 reachable at RHIC is around 10^{-3}, a factor of 40 lower than in E772. Therefore, nuclear shadowing effect of antiquarks can be well studied at PHENIX using the muon arms and the NCC to detect Drell-Yan events via the $\mu^+\mu^-$ and e^+e^- channels.

An important role of the NCC in the Drell-Yan measurement is that it will allow a realistic determination of the contribution of open-charm background to the dimuon (or di-electron) events. The $e\mu$ pair events from the NCC and muon arm would lead to a direct measurement of the charm background. This would enable a reliable Drell-Yan measurement down to the smallest possible x values.

2.2.2.2 The Cronin Effect and x_F-Scaling

Finally, the Cronin effect, first observed in fixed-target experiments, has also been seen in d+Au data at mid-rapidity. The mechanisms for the nuclear enhancement of large p_T events are still poorly understood. In particular, the dependencies of the Cronin effect on the hadron species and on the hadron rapidity (particularly the negative rapidity region) remain to be measured at RHIC energies. A universal x_F-scaling behavior [40] has been noted for hadron productions in p-A collisions. The ability to measure a variety of hadrons at the forward and backward rapidity region with the NCC would shed much light on the origin of the Cronin effect, as well as the validity of the x_F-scaling.

2.3 Spin Structure of the Nucleon

2.3.1 Physics Motivation

The nucleon is the only stable state of quarks and gluons known, the constituent which gives the atomic nucleus its mass, and therefore the mass of the visible matter which surrounds and comprises humanity. Despite decades of study, a detailed understanding of this state has eluded us. QCD, born whole as a lagrangian, describes a force which is too strong and complicated for the calculational techniques we have developed so far. Only in high-energy collisions has one been able to apply a quite sophisticated perturbation theory, due to the small value of the strong coupling α_s at the high-energy scale, that is, asymptotic freedom. Recent advances in the computational power of lattice theorists imply that we are close to the beginning of a new era of non-perturbative QCD calculations which can be realistically compared to data.

Unpolarized deep inelastic lepton scattering and Drell-Yan experiments have provided most of the data from which we have formed our present understanding of nucleon structure at high energy, an understanding which is still primitive. The 1-dimensional momentum

fraction of the quarks on the light cone has been mapped out from relatively low values up to roughly 85%, over a broad but unfortunately correlated range of resolution scales, i.e., Q^2. Already this has revealed a rich phenomenology of structure which can be understood, over many orders of magnitude in Q^2, as the rapid fluctuation of color field energy into matter. Given the empirical partonic structure at one resolution scale, we now can reliably calculate the structure at some other scale, even if we cannot predict the structure *ab initio.*

Nonetheless, we still have little understanding of the physics or even the empirical distributions at large momentum fraction. At very low momentum fraction, we are hampered by the experimental correlation with low Q^2 (large distance scale) resolution in order to test our understanding of the quark-gluon fluctuations which are observed. New, precise electron scattering experiments, using both the electromagnetic and weak force, give us the spatial charge and magnetization distributions of quarks in the nucleon, but are difficult to connect to the 1-dimensional light-cone momentum distributions. The newly recognized use of exclusive reactions to determine generalized parton distribution will allow us to empirically connect these two regimes.

At high energy, there remain two fundamental aspects of the nucleon partonic structure which are mostly poorly determined by experiment. One is the nature of the quark and gluon motion transverse to the light-cone momentum direction, in other words, the true 3-dimensional momentum distribution. The other is the nature of the nucleon spin. At present, we have a limited set of high-energy data which tell us the alignment of the quarks along the light-cone momentum direction, as a function of the momentum fraction. These distributions are unknown at both high and very low momentum fraction, and the resolution range in Q^2 explored is much narrower than in the unpolarized case. In fact, even these data are limited to the case where the nucleon spin is along the light-cone momentum direction. Until the advent of the RHIC polarized proton collider data, there was no precise and clearly interpretable data on the polarization of the gluons along the nucleon spin direction. The polarized lepton scattering experiments have made it clear that the quark spins only contribute about 30% to the nucleon spin. The gluons, which make up roughly 50% of the total (unpolarized) partonic momentum distribution, may be expected to carry a significant fraction of the nucleon spin, but this distribution is almost completely unknown at present. The RHIC spin program using longitudinally polarized protons promises to answer the question of the gluon spin contribution definitively. First measurements using the existing PHENIX spectrometer have already constrained the polarized gluon distribution. The NCC will allow PHENIX to make a significantly more detailed and precise investigation of the polarized gluon distribution over a much broader range of light-cone momentum fraction, and as a function of momentum fraction.

When one explores the polarization of quarks with the nucleon spin perpendicular to the light cone, our understanding of both transverse momentum and spin are strongly tested, and at least in experiment, intrinsically linked to each other. Ever since the observation of a large asymmetry in high-energy proton scattering, it has been clear that transverse effects would play an important role. These effects have been shown to persist even at RHIC energies, almost undiminished in size. Recent progress has been spurred by the observations of transverse asymmetries in lepton scattering from transversely polarized protons. First

glimpses from these experiments have prompted intense theoretical activity, with new insight gained into the role of gauge links in calculating partonic field operators. We now have firm predictions relating the fragmentation process in lepton scattering to that in Drell-Yan. The possibility of a distribution arising from the correlation of spin and longitudinal momentum fraction is now widely accepted, and again there are early first glimpses from lepton scattering. A natural explanation for this correlation is the existence of significant quark orbital angular momentum. In fact, orbital angular momentum is essentially unexplored experimentally at the partonic level. Exclusive reaction experiments, if able to determine the generalized parton distributions sufficiently well, can give us information only about the total angular momentum. Theoretically, there is now a much more thoroughly developed formalism to describe transverse measurements. The distributions are functions not only of momentum fraction and Q^2, but now transverse parton momentum k_T as well. While the dependence can be modeled, there is evidence that one can develop the transverse momentum distribution directly from perturbative QCD (pQCD). Thus, using transversely polarized protons at RHIC, one should be able to explore these new distributions in a regime where pQCD can be safely applied, for example using spin-dependent two-hadron correlation functions [41]. The addition of the NCC will clearly increase the PHENIX hadron acceptance at forward rapidity where the transverse effects are large. While extracting this new distributions is indeed more difficult, it is clear that this is a very active and developing area in high energy spin physics, and forward acceptance is required in order for PHENIX to be a major player in this area. If the longitudinal program finds that the gluon contribution to the nucleon spin is small, the transverse physics will be the only effective avenue at RHIC to study the partonic nature of orbital angular momentum.

Below we give a more detailed description of what we hope to learn from this program. In addition, we touch upon the role that the NCC may be able to play at 500 GeV in the study of the anti-quark production via W boson production.

2.3.2 Nucleon Structure: Gluon Polarization

Our present knowledge of the partonic structure of the nucleon is encoded in the so-called parton distribution functions (PDF) which depend on Bjorken x, the light-cone momentum fraction, and the momentum scale Q^2. Since the quarks are spin-1/2 particles, we can actually define two quark distributions, so-called helicity distributions, which describe the partons with the same or opposite helicity of that of a proton with helicity along the light cone direction. We will denote the polarized PDFs by $q_f^{\rightarrow}(x, Q^2)$ and $q_f^{\leftarrow}(x, Q^2)$, where f is the flavor of the quark or a gluon, however we will typically denote the unpolarized gluon distribution as $g(x, Q^2)$. In general, the unpolarized PDFs are then the sum of the helicity distributions: $q_f(x, Q^2) = q_f^{\rightarrow}(x, Q^2) + q_f^{\leftarrow}(x, Q^2)$. It is common to also define $\Delta q_f(x, Q^2) = q_f^{\rightarrow}(x, Q^2) - q_f^{\leftarrow}(x, Q^2)$.

The distributions for charged partons can be extracted directly from inclusive deep inelastic lepton scattering (DIS) experiments (in which only the scattered lepton is detected) if the Q^2 and energy ν of the photon are sufficiently high. Deep inelastic neutrino scattering allows one to separate quark and antiquark distributions, which the charged lepton scattering

cannot distinguish. One can attempt to isolate the charged partons by flavor using so-called flavor tagging, where the known valence quark content of of hadrons is correlated with the flavor of the quark which absorbed the virtual photon. The detection of DIS lepton and a leading hadron, known as semi-inclusive DIS (SIDIS), necessarily depends on modeling of the fragmentation process. Lepton scattering from the gluon distribution is complicated, as the gluon has no electromagnetic or weak charge, thus extraction is more model dependent. To date the most successful DIS program has been the analysis of di-jets [42], which primarily (but not exclusively) derive from the photon-gluon fusion diagram. If there is insufficient energy to produce jets, one may attempt to substitute leading hadrons, but again, one is now more model dependent. In fact, global fits are regularly made by a number groups around the world, using not only the DIS data, but also data from hadron colliders and theoretical constraints derived from QCD sum rules [43, 44, 45].

The dependence on these functions on Q^2 can be directly related to the fluctuation of the gluons into quark-antiquark pairs and the radiation of gluons by quarks through the DGLAP equations, and this provides an means in principle to determine the polarized gluon distribution from the Q^2 evolution of the polarized quark distributions measured in DIS. The results of a recent analysis [46] of the available polarized DIS data (from SLAC, CERN, and DESY) are displayed in Fig. 2.10 (left panel) and show that the present uncertainties on ΔG are so large that even the sign of the gluon polarization is barely constrained; much more precise polarized DIS data, over a broader range in x and Q^2, would be necessary to provide better limits. The fact that the photon-quark asymmetry A_1 itself has only very small Q^2 dependence gives this type of analysis only a small "lever arm."

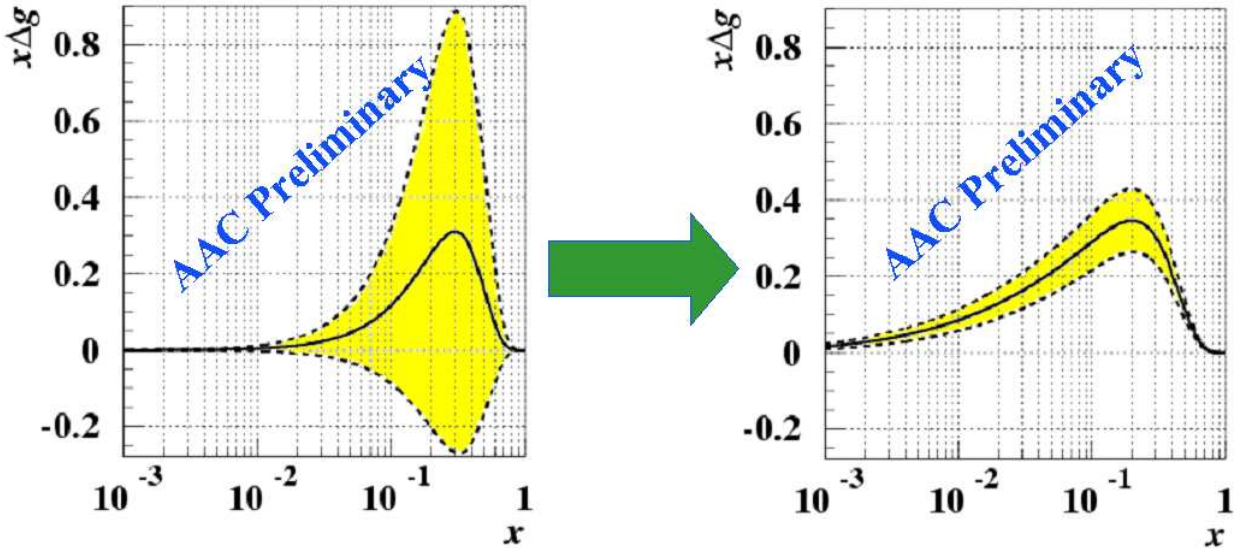

Figure 2.10: Polarized gluon distribution derived from NLO-QCD analysis of existing DIS data. The ranged limited by the dashed curves shows the range of gluon polarizations allowed by the data. The effect of including the direct photon results anticipated from PHENIX data from one year at design luminosity in the same NLO-QCD global analysis are shown in the right panel.

The RHIC spin program will provide the first precise measurement of the x-dependence of polarized gluon distribution $\Delta g(x)$. The PHENIX experiment, which has excellent particle identification and high rate capabilities, is well suited to this measurement as we are sensitive to Δg through multiple channels and each of these channels has independent experimental and theoretical uncertainties. Our main sensitivity is through inclusive hadron production, direct photon production, and heavy quark production.

In unpolarized $p+p$ experiments the gluon distribution function has been measured using single- and di-jet events as well as from direct photon events. In both cases, jets or high p_t photons carry information directly from the underlying hard scattering process which can be calculated using pQCD. As the cross sections factorize into a hard scattering and a proton structure part a measurement determines the parton distribution functions connected to the processes, schematically

$$\sigma \sim q\left(x_A\right) \otimes G\left(x_B\right) \otimes \left|\mathcal{M}_{\mathrm{pQCD}}\right|^2$$

where x_A and x_B are the fraction of proton momentum carried by the partons entering the hard scattering process. The theoretical problems present in the interpretation of fixed-target data have been largely resolved for the collider environment [47, 48]. PHENIX's first direct γ cross-section measurement indicates that these calculations are valid at RHIC.

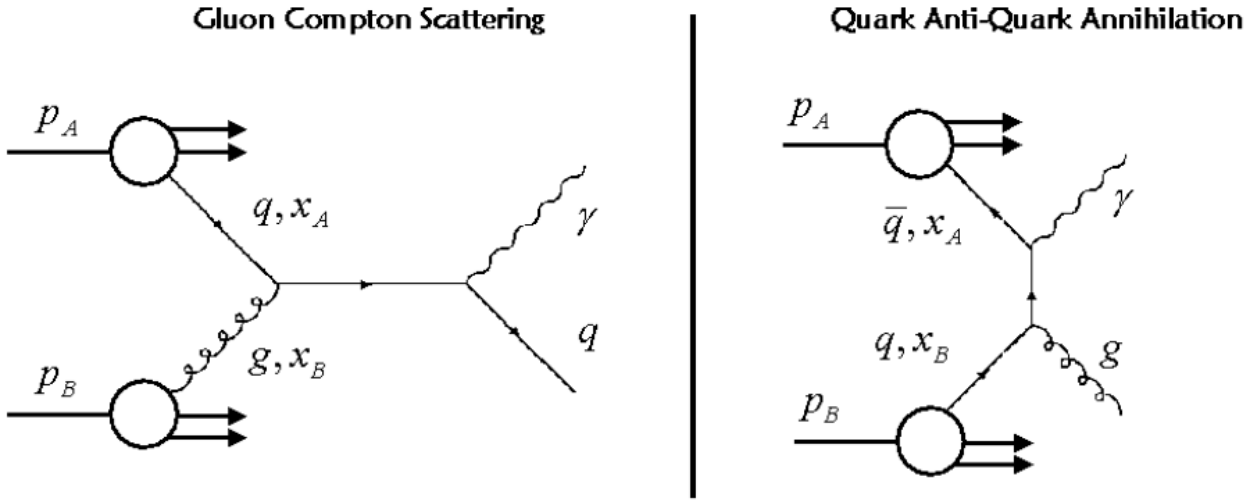

Figure 2.11: Direct photon production in the gluon compton and quark anti-quark annihilation processes. The ratio of the two processes has been studied using PYTHIA and was found to be about 9:1.

At RHIC, direct photon production is dominated by quark-gluon Compton scattering (see Fig. 2.11), which ensures that the double spin asymmetries from direct photon production provide the cleanest theoretical access to the gluon polarization $\Delta g/g$.

Helicity conservation at the quark-gluon vertex gives rise to a double spin asymmetry

$$A_{LL} \sim \frac{\Delta q_f\left(x_A\right)}{q_f\left(x_A\right)} \otimes \frac{\Delta g\left(x_B\right)}{g\left(x_B\right)} \otimes a_{LL}^{qg \rightarrow q\gamma}$$

from which $\Delta g/g$ can be extracted. The hard scattering asymmetry is denoted by $a_{LL}^{qg\to q\gamma}$ is calculated for the underlying quark-gluon Compton diagram with perturbative QCD. Background from the quark anti-quark annihilation process has been studied using the event generator PYTHIA and was found to be small.

The measurement of a double spin asymmetry for the case of detecting only the direct photon, typically as a function of p_T necessarily involves a convolution of over the momentum fractions of the colliding partons; one compares the measurements to QCD predictions based on different models of the gluon distribution. If one can also detect the opposing quark jet, then one may extract the the shape of the distribution more directly, as the initial momentums fractions x_A and x_B are now known (though the flavors and gluon combinations remain unknown and are summed over). This essentially allows a much more direct determination of the polarized gluon distribution. Unfortunately, the limited acceptance, $\eta \leq |0.35|$, of the current PHENIX detector and the absence of hadronic calorimetry presently make it impossible for us to reconstruct jets.

The NCC allows us to greatly extend the x-range of PHENIX's measurement. as well as provide information on the x dependence. The right panel of Fig. 2.10 displays the impact of PHENIX direct photon (inclusive) data on the range of allowed polarized gluon distributions. Despite the fact that the gluon polarization appears best constrained and falls off with decreasing x, the integral, ΔG, is dominated by contributions from $x < 0.1$ since this is the region where the gluons are most abundant [note that Δg is multiplied by x]. It is thus important to measure Δg to values of x as far below 0.1 as feasible. Historically it is interesting to note that the quark spin crisis only arose when EMC [49] extended the measurement of quark spin contributions to low x. Extrapolations of the SLAC [50] data alone led to results for the quark spin contribution consistent with expectations from naive quark models. The additional geometric acceptance in the forward direction provided by the NCC extends the measurement of the gluon polarization from $0.01 < x < 0.3$ down to about $x = 0.001$. Further, in combination with the new PHENIX inner tracker detectors, which will allow crude jet-reconstruction in the PHENIX central arm, the calorimeter makes it possible to obtain a rough measurement of x on an event-by-event basis by detecting the away-side jet associated with the recoiling quark. The x measurement allows for a leading-order determination of Δg as described above; this will be particularly valuable in constraining Δg at low x and complementing the NLO determination that will utilize the inclusive measurements. A rough jet measurement can also be made with the NCC, making possible a full range of measurements.

Overall, PHENIX is sensitive to Δg through multiple channels. The kinematic coverage for these various channels within PHENIX are shown in Fig. 2.12. The complementary measurements cover slightly different kinematic ranges, and most importantly provide alternative ways to the gluon polarization with different systematic and theoretical uncertainties. Figure 2.13 compares the x-Q^2 footprint of these channels to that of the DIS experiments.

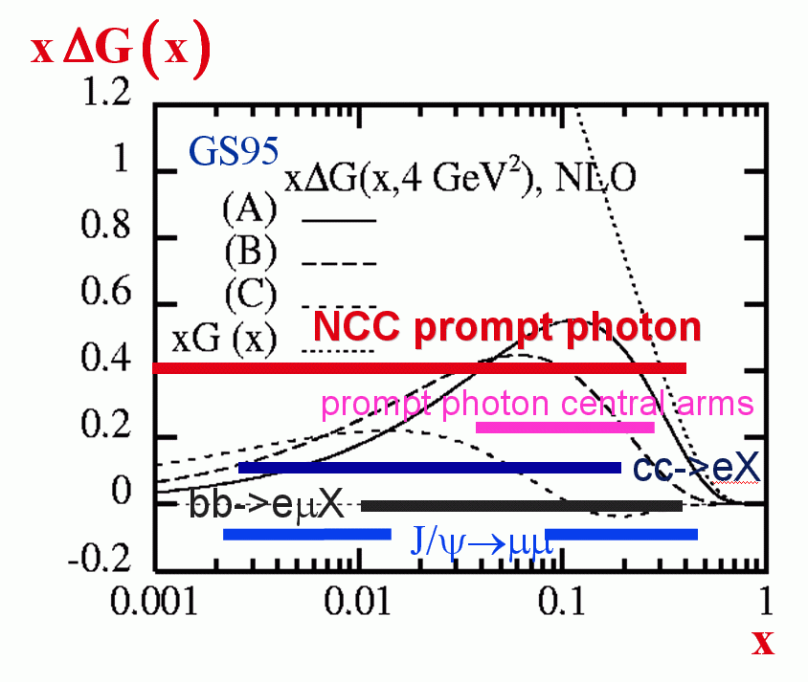

Figure 2.12: Kinematic coverage for PHENIX measurements that are sensitive to Δg. x_{Bj} range shown on-top parameterization of ΔG.

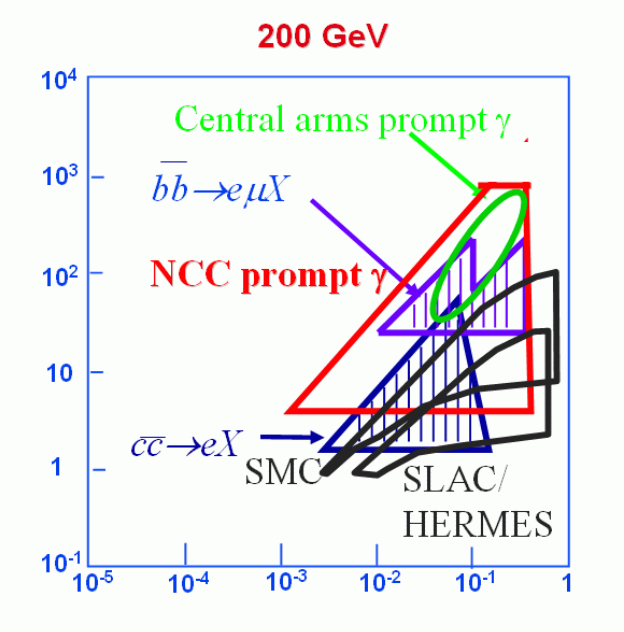

Figure 2.13: Range of x and Q^2 accessible by various DIS experiments compared to those accessible at PHENIX.

2.3.3 Transverse Spin Physics

It is fair to say the much of the interest in high-energy spin physics can be traced to two surprising results: the observations of large lambda hyperon polarizations [51] and large single spin asymmetries in pion production from polarized nucleon-nucleon collisions [52]. The general expectation from pQCD at leading twist was that these asymmetries would be vanishingly small, due to the chiral dynamics of QCD It was therefore startling when E704 discovered very large asymmetries in pion production from polarized $p+p$ collisions at $\sqrt{(s)}$ = 20 GeV. The expectation that yet higher energy would cause these asymmetries to vanish, was again invalidated by the STAR discovery that these effects persisted to the much higher $\sqrt{(s)}$ of 200 GeV [53], since it was thought that any power corrections should be suppressed at higher energies, despite the fact that the predictions of unpolarized cross-sections agree very well with the data. The single spin asymmetries for π^0 mesons detected at STAR, as a function of Feynman x, are shown in Fig. 2.14. Given that the magnitude of asymmetries at high energies are typically only a few percent, these forward asymmetries are quite large. One might questions whether the forward reactions are too soft to apply perturbative QCD, but as shown in Fig. 2.15 the cross sections are well described by NLO pQCD [54] as well as by PYTHIA [55]. The existence of large single spin asymmetries at RHIC, along with the good theoretical understanding of the unpolarized cross-sections gives hope that transverse spin effects can be used as a tool to probe the transverse structure of protons.

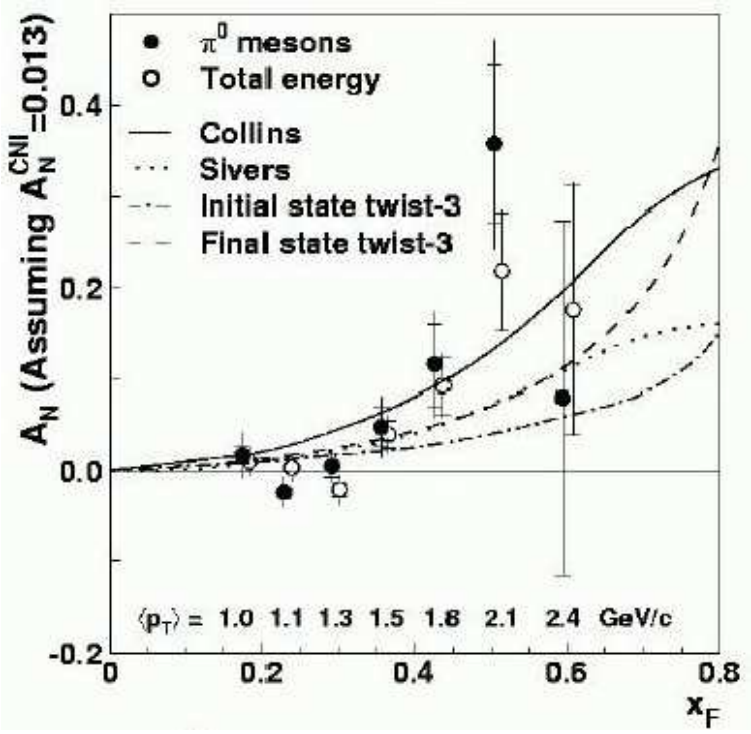

Figure 2.14: Single spin asymmetry from π^0 mesons at forward rapidity ($\langle\eta\rangle = 3.8$) as a function of Feynman x, measured at the STAR experiment from transversely polarized pp collisions at $\sqrt{s} = 200$ GeV [53].

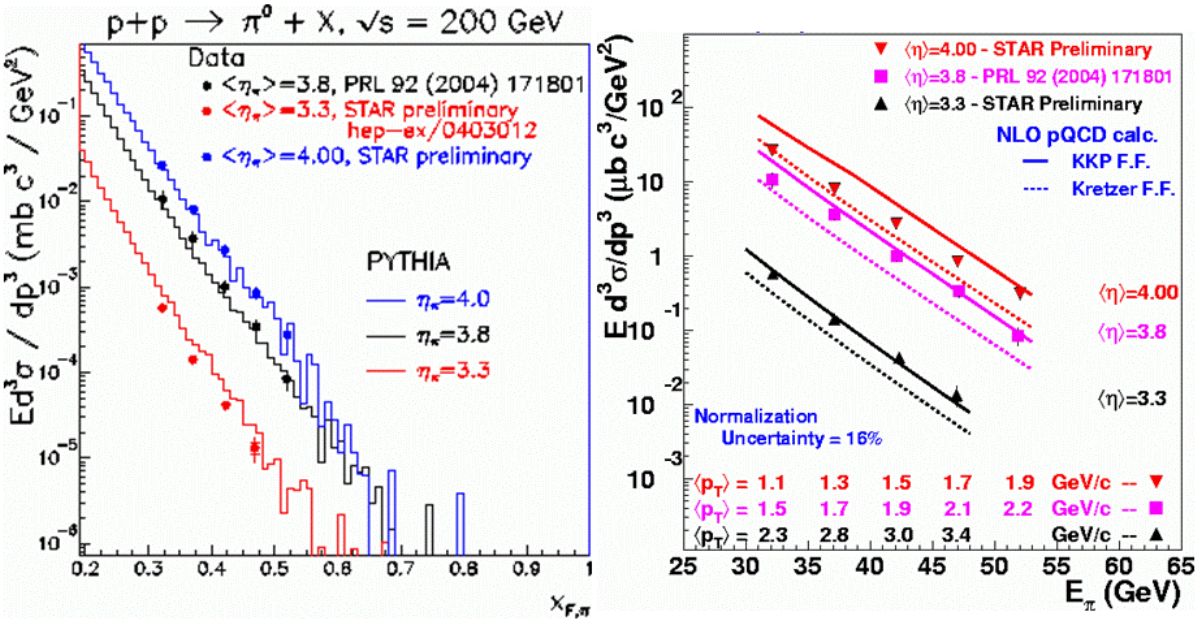

Figure 2.15: Forward inclusive π^0 cross sections measured at the STAR experiment from transversely polarized pp collisions at $\sqrt{s} = 200$ GeV [53]; the average pseudorapidity is $\langle\eta\rangle = 3.8$. In the left panel, these results are compared to predictions using PYTHIA [55] as a function of feynman x; in the right panel they are compared to NLO pQCD [54] calculations as a function of the pion energy.

There are three basic sources for the single spin asymmetries observed so far:

1. the existence of the Sivers function [56] which describes the correlation between the spin direction of the proton and the transverse momentum of the parton. Partons from the Sivers distribution fragment with the normal well-known fragmentation functions.

2. the existence of Collins fragmentation functions [57] which provide a correlation between the momentum of the final state particles with the direction of the initial parton spin. The initially transversely polarized quark are described by the transversity distribution [58]

3. Higher twist mechanisms in the initial and/or final state [59]

The recent observation of azimuthal asymmetries in semi-inclusive pion electroproduction at HERMES, from both longitudinally [60] and transversely polarized nucleon targets [61]

along with the STAR results has sparked renewed and intense theoretical study of this physics. Using the transversely polarized target data, HERMES has made a preliminary extraction of the separate asymmetries arising from the Sivers mechanism and the Collins mechanism. Additional efforts at BELLE have made the first extraction [62] of a Collins fragmentation function for e^+e^- annihiliation. Collins fragmentation functions of two pion states have also been proposed [63], and there is a preliminary observation once again at HERMES [64].

The existence of sizeable Collins fragmentation functions will allow the extraction of the transversity distribution of the nucleon $\delta q_f(x)$. Just as in the case of Δq_f, the transversity is a measure of the alignment of quarks along or opposite the nucleon spin; the critical difference is that in the longitudinal case, the nucleon spin is along the light-cone direction, while in the transverse case, it is perpendicular to this direction. Non-relativistically, this is a trivially different distribution, but once on the light-cone these are "independent" distributions, of the same leading order (A common (correct) model of the of the quark-gluon structure could predict both distributions, but you cannot determine one distribution from the other). The transversity is interesting for a number of reasons. Besides completing our knowledge of the nucleon at leading order, it is notable for being mainly sensitive to the valence quark spin structure, and furthermore, its Q^2 evolution is quite different due to the lack of coupling between gluon transversity functions and quark transversity functions. These attributes provide an important test of our understanding of the longitudinal antiquark and gluon spin structure functions, especially with regard to relativisitic effects.

The existence of Sivers distributions also provides an interesting window into the structure of the nucleon. This function accounts for the possibility that a parton's transverse momentum depends on the orientation of the nucleon spin. Orbital angular momentum of the quarks about the spin axis would naturally provide just such a correlation. At present, this connection is still not understood theoretically at the partonic level, but the distribution function itself is now generally accepted and well defined.

Effects in forward hadron production from transversely polarized pp collisions are somewhat more complicated than in polarized SIDIS, but as usual, the effects are typically larger and easier to study. Formally, there has been considerable progress in working out a formalism of possible distributions and fragmentation functions, for example as given in Refs. [65, 66, 67]. Predictions based on models of the nucleon are now being constrained by the data, but there is still much more data needed. As an example, the calculation of the asymmetry in pion production for the E704 experiment is shown in Fig. 2.16, taken from Ref. [67]. These models explore maximal bounds for the various distribution, but the point here is that the distributions in x_F are quite different, and they do not change much as a function of energy.

The NCC along with the recently installed Muon Piston Calorimeter(MPC) and the standard PHENIX central detectors will allow an important series of transverse spin measurements to be carried out at PHENIX. These should us to separate out the mechanisms contributing to the forward inclusive asymmetry. Specifically, the Sivers distribution can be measured in the azimuthal asymmetry of back-to-back di-hadrons or di-jets, where one of the hadrons is the forward π^0 or jet. The Collins fragmentation function can be measured

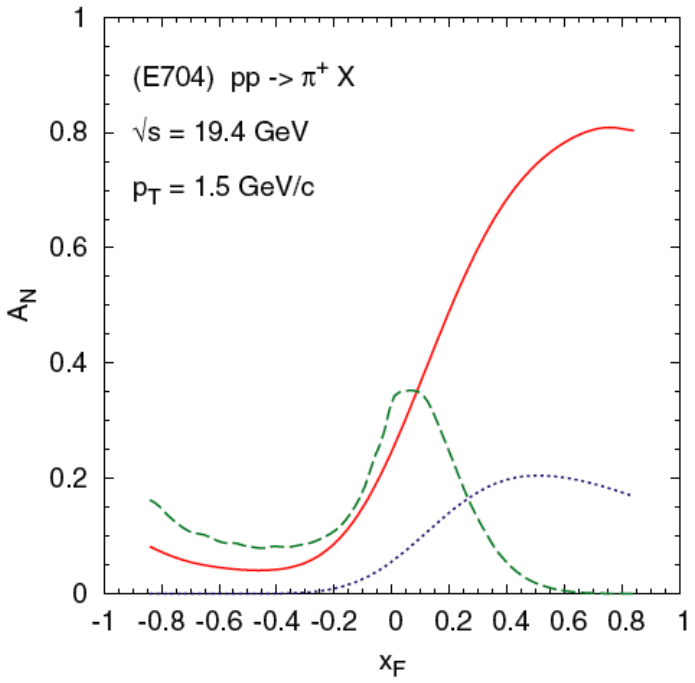

Figure 2.16: Different contributions to A_N, plotted as a function of x_F, for $p^{\uparrow}p \rightarrow \pi^+ X$ processes and E704 kinematics. The different lines correspond to solid line: quark Sivers mechanism alone; dashed line: gluon Sivers mechanism alone; dotted line: transversity $\otimes$ Collins. All other contributions are much smaller. Taken from Ref. [67].

in the hadron distribution around a jet axis. The two hadron Collins function can be measured by di-hadron correlations in the near side of a jet. Whatever is left can be use to test calculations of higher twist effects.

In general the exploration of transverse spin asymmetries in SIDIS and pp collisions requires one to investigate the dependence of the asymmetries on the p_T of the hadrons. This raises serious questions about the universality of the distribution and fragmentation functions which can be investigated in both experiment and theory. It has as well forced modelers to include the intrinsic k_T of the partons in some fashion. These issues are being addressed aggressively by the theoretical community. In fact, if we hope to start developing a true 3-dimensional understanding of the nucleon structure, this physics must be confronted and understood.

2.3.4 Nucleon Structure: Quark Polarization

While Δq has been fairly well measured, the anti-quark's contribution to Δq is not well-known. Some information has come recently from the polarized SIDIS measurement from the HERMES collaboration [68], using a flavor tagging analysis of the identified hadron asymmetries. The HERMES results on the sea polarization are accompanied by a substantial systematic error due to the observed small size of the asymmetry, and the weakness of the

correlation from the flavor tagging. As usual, the weak interaction is of critical use in determining the sea quark distributions, allowing the PHENIX measurement to provide an important independent measurement of high precision and much higher Q^2, using an experimental approach completely different from that of HERMES.

The high-energy polarized proton beams at RHIC provide copious yields of W bosons, and the parity-violating nature of the weak interaction permits the extraction of light quark and anti-quark polarizations through measurements of longitudinal single spin asymmetries in W^+ and W^- production. Bourrely and Soffer first discussed this idea using QCD at leading order perturbation theory [69]. Recently Yuan and Nadolsky presented a using modern resummation techniques in addition to an NLO calculation [70]. This work leads to a robust interpretation of the PHENIX quark polarization measurement in W production. In PHENIX, W production is characterized either by detecting high-energy electrons (or positrons) in the two central spectrometer arms or by reconstructing high-p_T muons in the two muon spectrometers. Due to their eight–times-larger acceptances, the PHENIX muon spectrometers will dominate the measurement statistically. The anticipated integrated luminosity of 800 pb^{-1} will yield approximately 10^4 detected W^+ and W^- events. However, before a successful measurement can be carried out, the event selection electronics must be improved significantly. The muon trigger was designed for heavy ion running and low-luminosity proton collisions; an upgrade is required to record selectively energetic muons from W decay during the high-rate spin running. Recently, the NSF has awarded a collaboration within PHENIX funds of almost \$2M to carry out this upgrade using resistive plate chambers to be installed in each muon spectrometer.

Figure 2.17 shows the projected precision of PHENIX on the light quark polarizations in the proton. Superimposed on the plot are projections of the accuracy achieved in preliminary results from HERMES (the figure has not yet been updated with the actual published final results). The anticipated measurements are highly complementary in nature. The HERMES results feature more complete kinematic coverage, while the PHENIX results are of greater precision. The PHENIX technique distinguishes cleanly between the light quark flavors in a model-independent way, while the HERMES kaon asymmetries are able to probe the strange quark polarization. Finally, the systematic uncertainties in the two experiments are of completely different origin.

The measurement of the anti-quark spin contribution to the spin of the proton will be via the measurement of high p_T leptons coming from W's – a rather rare process. The NCC upgrade will extend this measurement both by allowing the detection of electrons and positrons in the forward region (though without charge determination) – in addition to the muons, and in reducing potential backgrounds. One of the potentially large backgrounds is the decay of low momentum pions and kaons within the magnet muon tracker volume, resulting in an apparently straight line (high momentum) trajectory. Such background events can be studied and, if necessary, reduced by requiring a separation between the lepton-detected by either the muon spectrometer (muons) or the calorimeter (electrons) and the jet, as detected by the calorimeter.

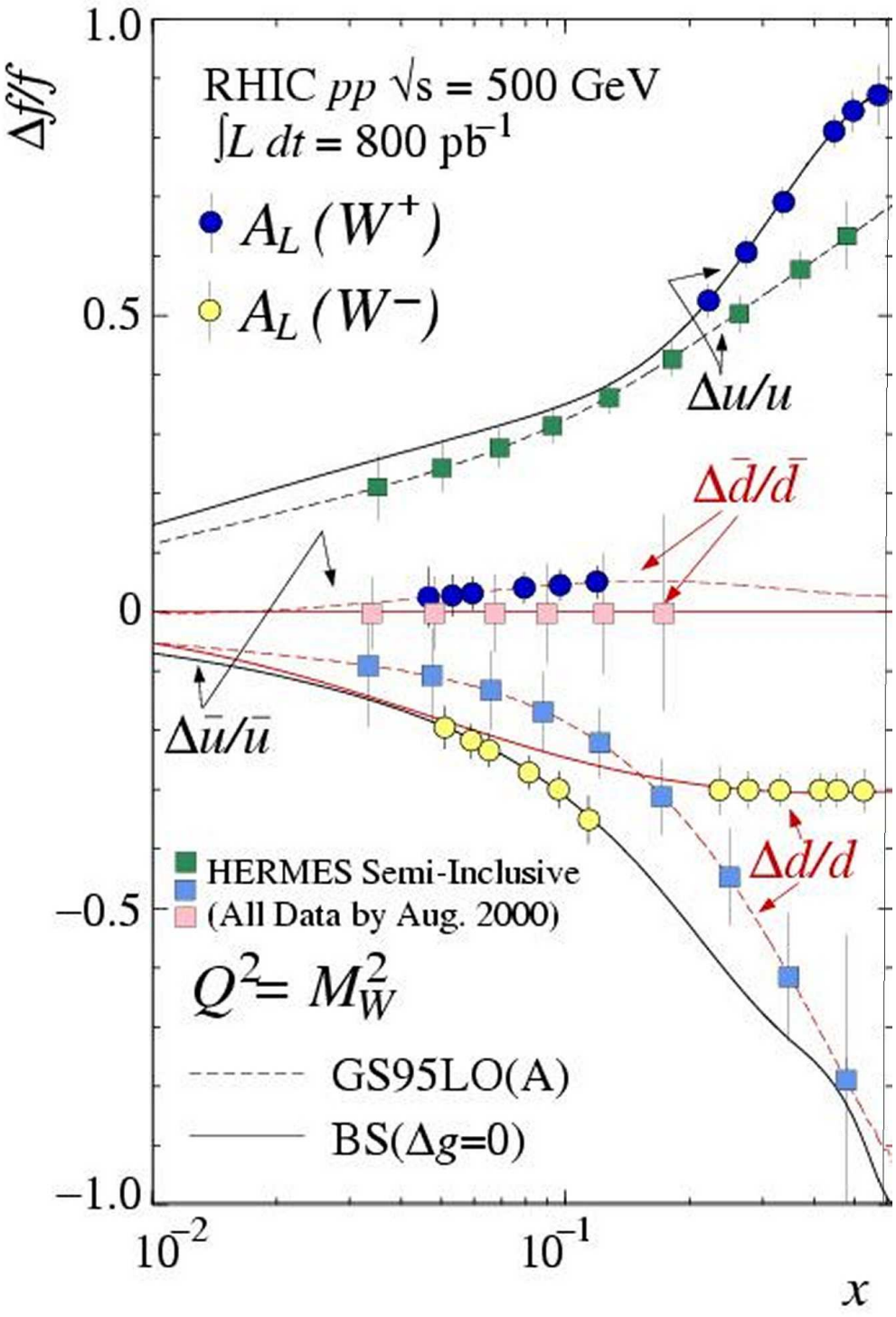

Figure 2.17: Simulation of measurements of light quark polarizations from W boson production at RHIC, compared with preliminary data from the HERMES experiment.

Chapter 3

Design of the NCC

3.1 Overview

The PHENIX[1, 71] detector, illustrated in Fig. 3.1, is designed to perform a broad study of nucleus-nucleus (A+A), proton- or deuteron-nucleus (p+A or d+A), and proton-proton (p+p) collisions to investigate nuclear matter under extreme conditions and to measure spin dependent structure functions. The needs of the heavy-ion and polarized-proton programs have produced a detector with unparalleled capabilities. PHENIX measures electrons muons, photons, and hadrons with excellent energy and momentum resolution. PHENIX utilizes global detectors to characterize the collisions, a pair of central spectrometers at mid rapidity to measure electrons, hadrons, and photons, and a pair of forward spectrometers to measure muons. Each spectrometer has a geometric acceptance of about one steradian and excellent particle identification.

The proposed Nosecone calorimeter, a major component in the forward spectrometer upgrade, will introduce new detector elements in the forward direction which will result in a ten-fold increase in rapidity coverage for charged hadrons and photons. As mentioned in the previous sections, this upgrade will provide us the access to physics observables that are to date not accessible to PHENIX or available only indirectly with very limited accuracy. Forward production of inclusive jets, direct photons or Drell-Yan pairs at large xF in nucleon-ion collisions at RHIC will provide a new window for the observation of saturation phenomena expected at high parton number densities [31, 32, 33, 72, 73, 74]. In addition these upgrades will give greater coverage for the direct photon-jet measurements, critical to the measurement of the spin dependent structure functions, and photon decays of the charmonium states such as the $\chi_c \rightarrow \mathrm{J}/\psi + \gamma$ for the study of charmonium suppression in heavy ion collisions.

3.2 Upgrade Layout and NCC Configuration

The NCC will occupy the space along the collision axis which is currently used by supplementary muon filters (NoseCones, one for each magnet pole) consisting of Cu disks 19 cm deep and $\sim$ 1m in diameter. The depth of the new calorimeter is chosen to fit within the envelope of the existing Cu Nose Cones.

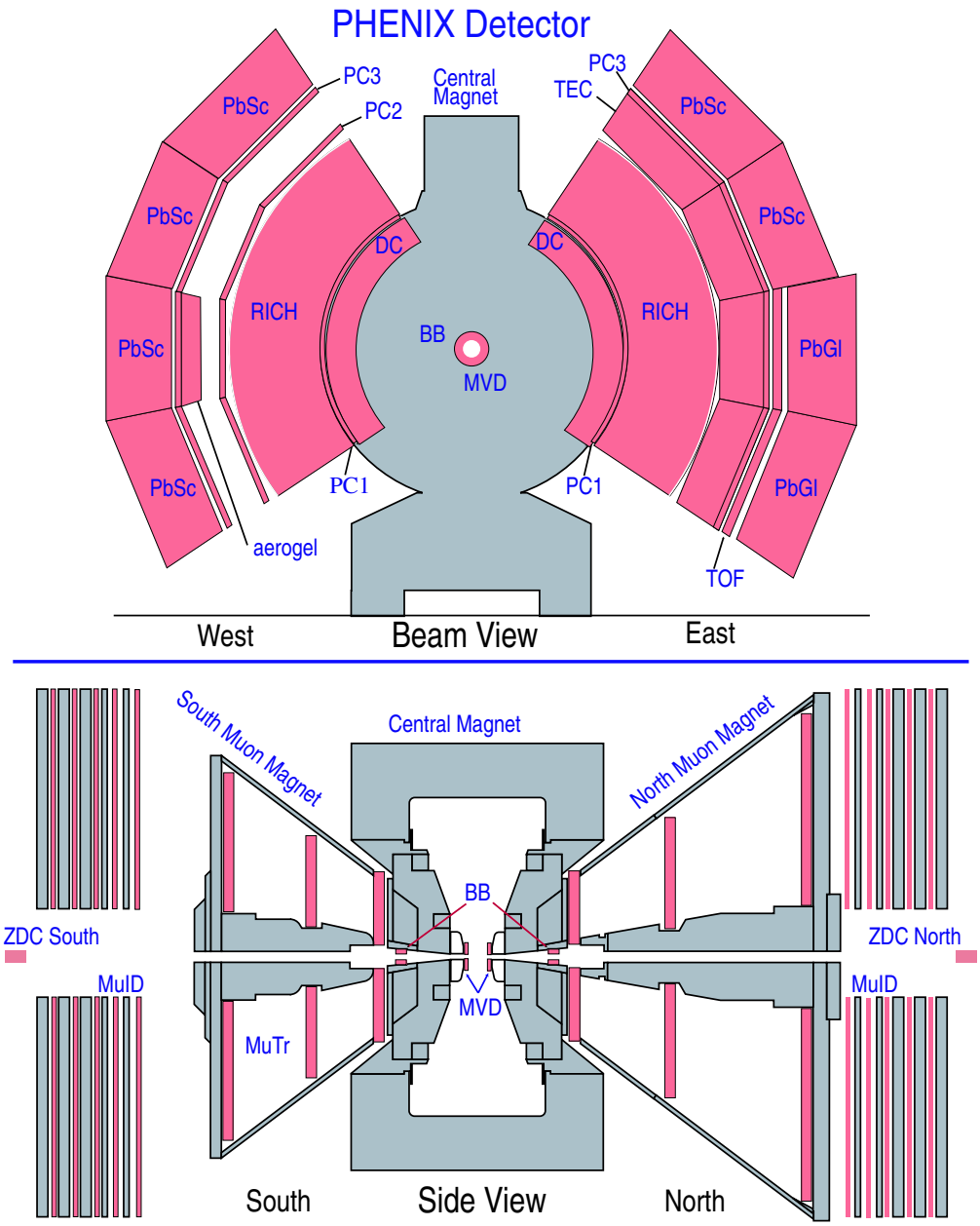

Figure 3.1: A beam view (top) and side view (bottom) of the PHENIX detector in its most recent configuration. MVD - Multiplicity Vertex Detector, BB-Beam-Beam trigger counters, DC-Drift Chambers, RICH - ring imaging Cerenkov counters, PC-Pad Chambers, TEC - Time Expansion Chambers, PbSc/PbGl – Electromagnetic Calorimeters, MuTr/MuId -Muon Tracking and Muon Identification, and ZDC - Zero Degree Calorimeters. There is an axial magnetic field in the central regions, the muon magnets produce a radial magnetic field.

Currently the PHENIX Forward (Muon) spectrometers (illustrated in bottom panel of Fig. 3.1) are limited to identifying muons and measuring their momenta via the muon tracker (MuTr) and the muon identifier (MuID). As a component of the PHENIX Forward Spectrometer the NCC will add the following:

1) precision measurements of individual electromagnetic showers,
2) $\gamma/\pi 0$ discrimination similar to the central PHENIX electromagnetic calorimeters,
3) photon/hadron discrimination,
4) jet finding, jet energy and impact position measurements,
5) data for fast triggering.

The other components to the upgrade are a) an enhanced muon trigger that processes signals from the R1-R3 trigger chambers which is able to recognize muons and impose cutoffs on the muon pointing and muon momenta at a RHIC rate of 10 MHz, and b) a forward Si vertex detector (FVTX) for identifying secondary vertices. The proposed upgrade to the forward spectrometers is shown diagrammatically in Fig. 3.2.

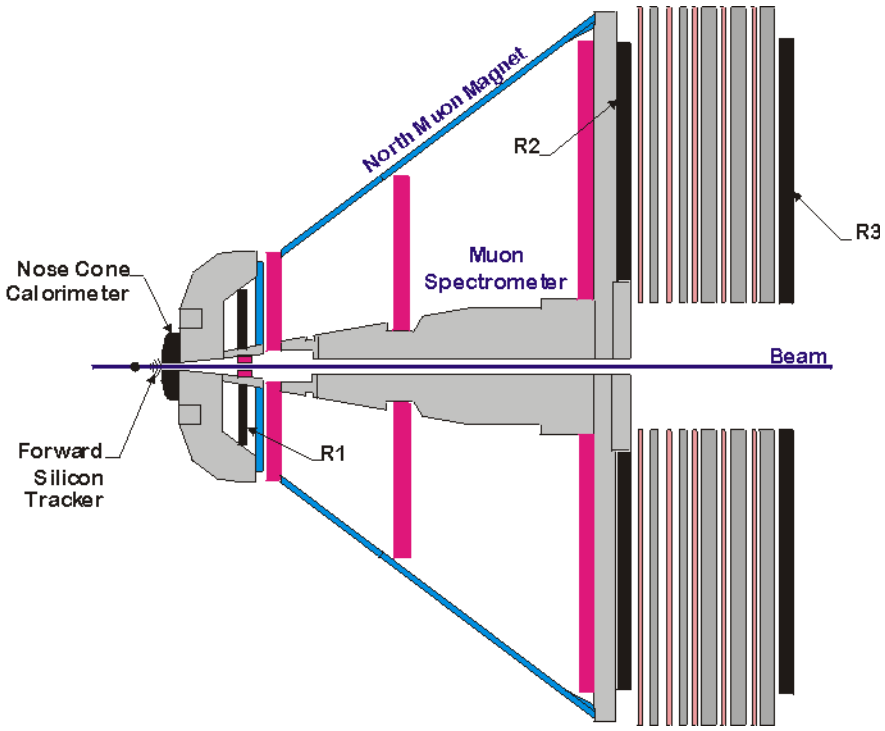

Figure 3.2: Schematic rendering of the new PHENIX Forward Spectrometer. R1-R3 – resistive plate chambers built for triggering on muons. Other components are detailed in what follows.

Fig. 3.3 indicates the sharing of available real estate in the upgraded central region with the Forward and Central Silicon Vertex Trackers (VTX), and with the Hadron Blind Detector (HBD). We have designed two identical NCC for the North and South Arms of PHENIX. Fig. 3.4 shows a 3-d rendering of the PHENIX central region with the NCC and the new silicon-based sensing devices (VTX and FVTX) installed.

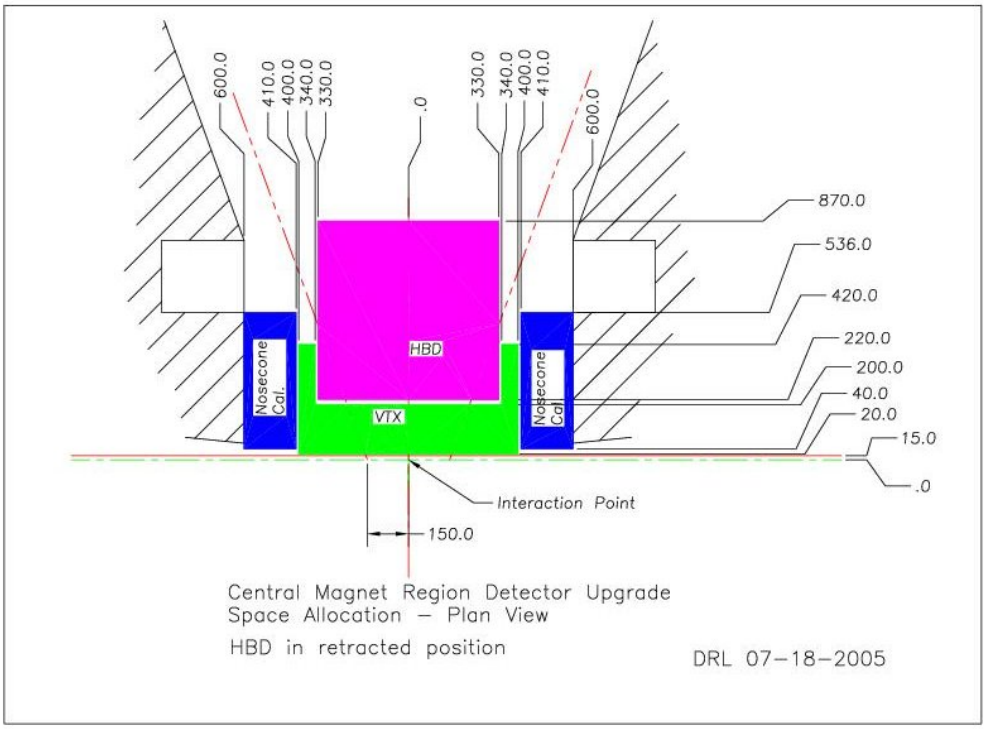

Figure 3.3: Sharing of the space budget between new detectors in central region.

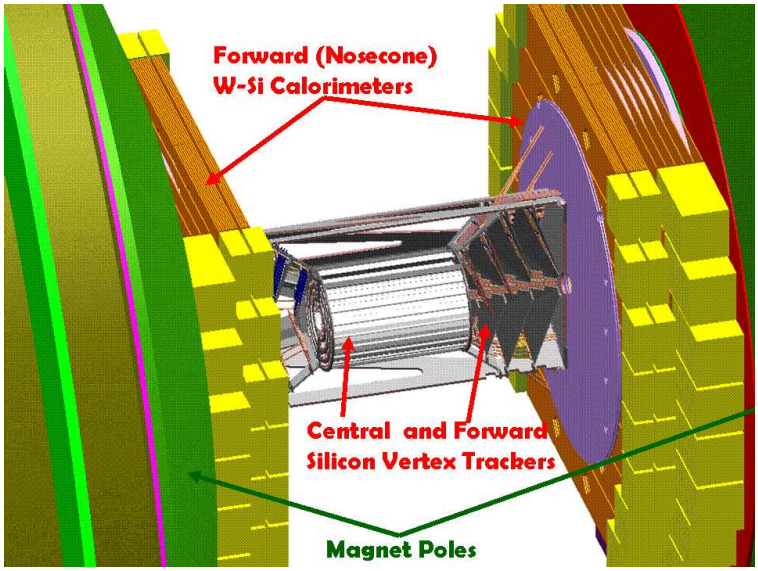

Figure 3.4: 3-d rendering of the new detectors employing silicon sensors in the central PHENIX region.

3.3 NCC Design Considerations

The design requirements imposed on the detector from physics considerations are:

- the ability to measure electromagnetic showers with a precision comparable to the sum of all systematic uncertainties characteristic of similar measurements with PHENIX central electromagnetic calorimeters (π^0 effective mass resolution better then 20 MeV in the p_T range above 5 GeV/c),
- the ability to discriminate between electromagnetic and hadronic showers in the calorimeter allowing extraction of the direct photon signal down to ∼5% of the π^0 yield,
- the ability to reconstruct π^0's via effective mass measurements and shower shape analysis to the p_T extent allowed by the calorimeter acceptance and RHIC luminosity,
- the ability to measure shower impact vectors with resolution sufficient for efficient matching to charged tracks reconstructed by Forward Silicon Tracking when it becomes available,
- the ability to measure the total jet energy and jet angle with precision sufficient to reconstruct kinematics of the g-q hard scattering resulting in γ-jet events with jets in the forward direction,
- ability to measure energies inside the jet cone around high p_T lepton candidates for isolation testing.

Satisfying these specifications requires a combination of highly segmented electromagnetic (EM1 and EM2) and hadronic (HAD) compartments supplemented by high resolution position detectors located at a depth in the calorimeter sufficient to convert both photons from π^0 decay with good probability (preshower detector-PS) and measuring decay asymmetry so the efficiency of π^0 reconstruction and π^0 yield are correctly measured (shower maximum detector-SM). The longitudinal structure of the single calorimeter tower is sketched in Fig. 3.5.

The NCC's are located 40 cm from the nominal collision point on both north and south poles of the PHENIX central magnet and limited to a depth of 19 cm each. Building the instrumentation capable of attaining the required performance under the constrains of PHENIX geometry requires the densest known absorber material (tungsten) and the most versatile active media known to instrumentation in physics (silicon). Silicon provides for simplicity of the transverse segmentation and tungsten has a small Moliere radius (9 mm) so the showers are very compact. Tungsten also has an excellent ratio of radiation and absorption lengths which is very important for electromagnetic energy measurements in the presence of heavy hadronic background. (Pb has and even better ratio, but is much too light compared to W.)

In order to achieve the goals outlined using the available technology requires compromises depending on priorities assigned to different performance specifications. Based upon physics

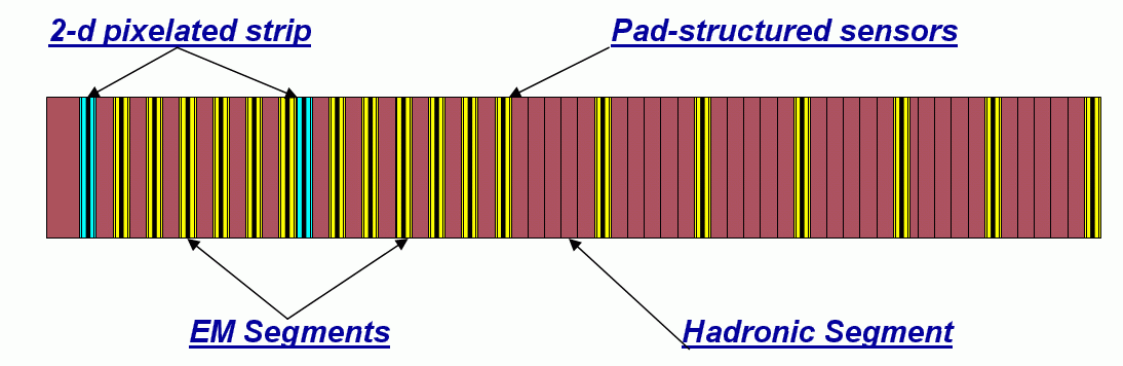

Figure 3.5: Longitudinal structure of a single calorimeter tower showing the locations of the three calorimetric segments, EM1, EM2, and HAD, and the high resolution position detectors- preshower(PS) and shower-max(SM).

expectations priorities are given to particle identification (including resolving close showers) and electromagnetic energy measurements.

A few cm of tungsten will fully absorb the electromagnetic showers, hence a properly structured 20 cm deep tungsten calorimeter can have both an electromagnetic segment and a shallow hadronic (leakage) segment. The W plate thickness and the total depth of absorber in the calorimeter are constrained by readout which is about 2.5 mm per layer divided up into 0.5 mm silicon, 1.6 mm of pc-board, and clearance gaps.

The design of the NCC relies heavily on past experience in Si-W calorimetry[75, 76]. Since the scheduling of upgrades in not fixed and since it will probably not be possible to obtain a momentum from the FVTX because of the Bdl available we require that the NCC be capable of doing particle identification as a stand alone device.

Such a calorimeter covering an area $\sim$0.7 m^2 with towers comparable in size to the Moliere radius will have $\sim$3000 silicon pixels per readout layer. In preparation for experiments at a future electron-positron linear collider a number of ongoing R&D projects aimed at building readout for the W-Si calorimeters able to digitize signals from every pixel in all sampling layers of a silicon-tungsten calorimeter are currently ongoing. The solutions are mostly on the drawing board and prohibitively expensive. To reduce cost and complexity we decided on a solution in which pixels from a number of sequential silicon sampling layers are ganged together and connected to the input of a single amplification/digitization circuit.

This allows us to reduce the number of channels in the detector by a factor of 6 (see below), and to use signal amplification solutions developed by the BNL Instrumentation Department for earlier projects[77]. It also solves the problem of compatibility between a new detector and existing mechanical infrastructure in efficient manner.

The present design is optimized to obtain shower shape measurements and the spatial separation of energy depositions due to photons from those due to charged and neutral hadrons reaching the calorimeter for a reasonable cost. Because of the limited space available we have chosen to use the same lateral granularity throughout the depth of the calorimeter which is easily achievable using alternating tungsten and silicon layers.

The optimization process for the design described below, resulted in the calorimeters built of 18 pad-structured sampling layers and two layers of 2-d position sensitive pixilated strips (preshower-PS and shower max-SM) which will serve as a very efficient photon-π^0 identifier able to discriminate between individual electromagnetic showers and overlapping photons from high momentum π^0's. Both longitudinal and lateral shower profiles can be measured in the device and are used in the particle identification.

We have chose 3 mm W plates for the first two fine segments (EM1 and EM2) based upon the following simple considerations.

The radial shower profile, which is the main characteristic used to discriminate between single vs multiple showers, has a pronounced central core surrounded by halo. The central core effectively disappears beyond shower maximum (in depth). The radial profile integrated over the whole shower depth in different materials is shown in the Fig. 3.6.

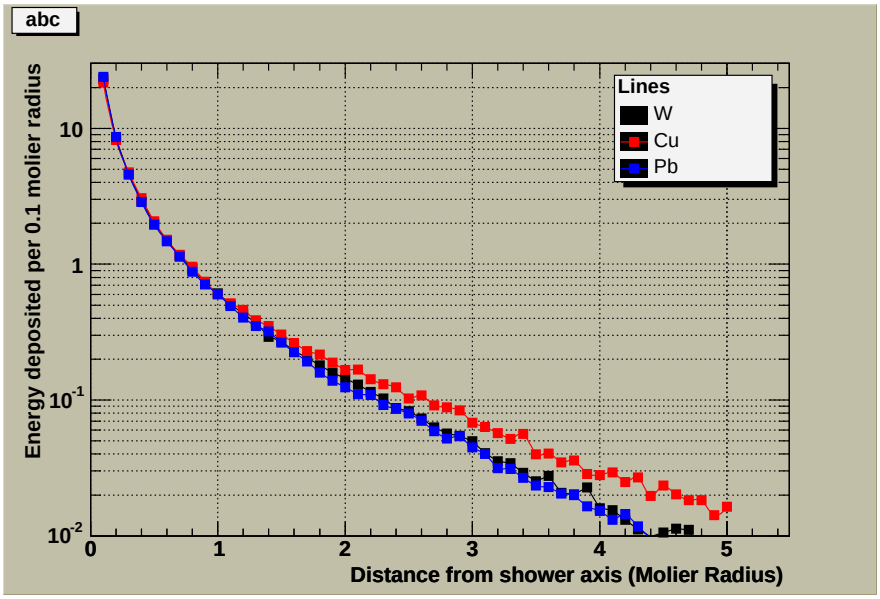

Figure 3.6: Radial profile of the electromagnetic showers in different materials(from simulation)

In Fig 3.6, the distance from shower axis is in Moliere units (9.3 mm for W). It is not a surprise that W and Pb show nearly identical behavior (although the actual values of Moliere radii are different by almost a factor of 2). Because of the compactness of the showers, W is the material of choice if two-shower resolving power is the primary goal. 50% of the shower energy is contained within a radius of 0.25 $R_{Moliere}$. 0.25 $R_{Moliere}$ is a back-of-the-envelope estimate for intrinsic limit for efficient two-shower separation since further improvements are hampered by fluctuations in the number of particles in the shower). Symmetrically decaying 30 GeV/c π^0's will have two photons in the calorimeter at a distance of the order of 5 mm (depending on the production kinematics) thus setting the upper limit to the Moliere radius for NCC equal to 20 mm. Technology sets a lower limit to the thickness of readout layers (carrier boards, silicon sensors, interconnects, protection) close to 2.5 mm. To keep the Moliere radius below 20 mm the thickness of W plates in the fine sections of calorimeter must

be equal or above the same 2.5 mm value. We propose to build electromagnetic segments of 3mm W + 2.5 mm readout sampling cells.

For energy measurements in the multi-GeV range, the energy resolution is driven by the sampling fluctuations which can be reasonably well described with the following simple formula (see [78]):

$$\frac{\sigma}{\sqrt{E}} = c\sqrt{d/f_{sample}},$$

where the thickness d of the active layers is in [mm] and f_{sample} is the sampling fraction for MIP's.

An infinitely deep calorimeter built of 3 mm W plates and 2.5 mm readout layers (525 mm Si sensors) will sample approximately 2.3% of energy left in the calorimeter by minimum ionizing particles resulting in the intrinsic limit to the energy resolution (sampling fluctuations only) of

$$\frac{\sigma}{E} \simeq \frac{14\%}{\sqrt{E}}.$$

The NCC should discriminate between electromagnetic and hadronic showers based upon shower shape measurements only, and retain the reasonable energy resolution and be able to measure jets to some extent. This requires reasonable longitudinal containment of electromagnetic showers in EM1 and EM2 and a total shower energy measurement for hadronic showers well downstream of the total depth required to contain electromagnetic showers. The latter constraint implies the presence of a hadronic (or leakage) segment. We propose to build relatively shallow electromagnetic segments leaving as much space for the leakage section as available. The relative shallowness of the electromagnetic segments serves to suppress the hadronic pile-up contribution to electromagnetic energy which is mostly contained in EM1 and EM2. The hadronic segment (HAD) is structured following the pattern used in EM1 and EM2 (except for the tungsten plates thickness which is 15 mm) will (1) assist the energy measurements of photons at the extreme upper end of the spectrum, (2) serve as an effective electromagnetic/hadronic discriminator tool, and (3) guarantee the low-grade hadronic energy measurements in calorimeter. Thick hadronic plates will certainly degrade the calorimeter energy resolution for electromagnetic shower measurements at the high end of energy scale but the compromise seems unavoidable to compensate for missing charged particle momentum measurements. A short summary of the calorimeter design features is in the Table 3.1 (all counts are for a single calorimeter unit). Implementing these ideas will result in a calorimeter with the total depth seen by particles at normal incidence of $\sim$42 X_0 or 1.6 L_{abs}.

Two layers of precision position sensitive silicon detectors (PS and SM) located downstream of converter and between two fine sections at approximately a shower max depth, will discriminate single vs multiple photons and measure decay asymmetry.

We will further discuss calorimeter energy resolution and energy containment in its connection to particle identification in longitudinally segmented calorimeter (based upon detailed GEANT simulation of calorimeter response) in the next section of this document.

There still remains an issue of concern for direct photons physics, that is the background of charged electrons impinging on the NCC. Without the addition of the FVTX some sta-

tistical tools are still available: photon showers are ~ 1 X_0 delayed compared to those due electrons. In the calorimeter fine longitudinal segmentation may give valuable information although its use will require some creativity in the analysis. We anticipate that the FVTX will become available within a reasonable time, hence we will be able to identify charged tracks entering the NCC.

Table 3.1: Nose Cone Calorimeter design features. All counts are for a single unit

Parameter		Value	Comment
Distance from collision vertex		40 cm	
Radial coverage		50 cm	
Geometrical depth		$\sim$ 19 cm	
Absorber		W	42 X_0 or 1.6 Labs
Readout		Si pads (15x15 mm2) and pixelated strips (.0.5x0.5 mm pixels grouped into 60 mm long strips)	
Calorimeter		EM1 and EM2 (12 sampling cells: 3mm W + 2.5 mm readout) longitudinally structured into two identical non-projective sections. HAD (6 sampling cells: 15 mm W + 2.5 mm readout)	
Preshower detector (PS)		2 X_0 W converter followed by a stripixel layer (0.5 mm strips) with 2-d readout	
Shower max detector (SM)		In between EM1 and EM2 at $\sim$ 7 X_0 depth. Stripixel layer (0.5 mm strips) with 2-d readout	
Sensors		calorimeter	3192 (12 x 168 + 6 x 196)
		PS and SM detectors	336 (2 x 168)
Channel count		calorimeter	8152
		PS and SM detectors	86016 (672 SVX4 chips)
Multiple scattering in NCC combined with Fe magnet pole		133 MeV	To compare with 106 MeV in the existing configuration with Cu NoseCone
Expected EM energy resolution		$27\%/\sqrt{E}$	
Expected jet energy resolution		$100\%/\sqrt{E}$	
Two showers resolved at	in calorimeter	3 cm	
	in preshower	2 mm	
	in shower max.	4 mm	

3.4 The Performance of the NCC

An extensive study of the present design has been in progress which included a Monte-Carlo simulation and hardware R&D programs culminating in the construction and beam testing of a detector prototype to be described later in this section. In our simulation effort the calorimeter as described above was simulated using GEANT to produce libraries of electromagnetic and hadronic showers. The calorimeter was located 40 cm from the production vertex. The whole active area of the calorimeter was uniformly illuminated. The simulated data presented below are integrated over all impact angles (0 to 45 degrees).

3.4.1 Simulations - the Optimization Procedure

For the purposes of optimization the calorimeter was initially simulated as a uniform stack of 0.5 mm thick W plates and similar thickness silicon layers. This trivial representation is convenient for testing the dependence of calorimeter characteristics as a function of calorimeter longitudinal structure: by combining layers one can easily vary multiple design parameters with a common set of simulated data. The configurations studied always comprised of three longitudinal segments (EM1, EM2, and HAD). The parameters subjected to optimization were the number of sampling layers in the segment and W plate thickness in the first two segments. The number of sampling cells in the HAD segment was kept equal to those in EM1 and EM2, the thickness of plates was always adjusted to fully occupy all available geometrical space along the beam axis. Fig. 3.7 is included to illustrate this approach.

Simulated electrons with an exponential momentum distribution were incident on the calorimeter with an inverse slope of 6 GeV/c. The slope of the reconstructed spectra were then compared to initial spectra to see if the convolution with errors have a visible effect on the slope. 12 sampling cells of 2 mm W plates is definitely too shallow an electromagnetic calorimeter (resolution is dominated by leakage into hadronic segment). It takes plates of at least 3 mm (our current choice for the plate thickness) to reach the saturation.

An optimized longitudinal structure was further simulated using a standalone GEANT implementation of a calorimeter shown in Fig. 3.5 and an output structure which enabled attribution of energies to specific towers and stripxels in readout layers. Results shown below are mostly based upon subsequent analysis of this data.

3.4.2 Shower Containment and Energy Resolution

The two panels in the Fig. 3.8 illustrate the main aspects of the NCC design and performance directly related to the PHENIX experimental goals. On the left is an electromagnetic shower developing in the NCC, on the right is a charged pion induced shower.

Most of the electromagnetic energy stays in the electromagnetic segments (EM1 and EM2). The depth and position of those segments with respect to the shower profile insure a linear dependence of the energy deposited in the EM2 vs the energy of the photon. Hence a trigger on electromagnetic energy can be based upon hits in the second segment only. The electron and pion showers show a distinctly different energy sharing between segments.

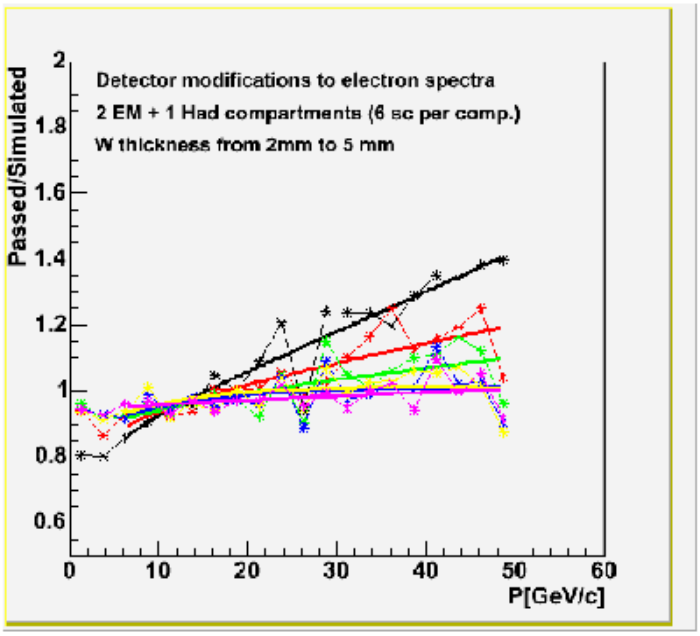

Figure 3.7: Momentum dependence of the ratio between momentum spectra of simulated electrons (in the denominator) and showers satisfying electromagnetic identification criteria (numerator) in NCC. Thickness of the W plates in EM segments is color-coded (varies from 2mm (black) to 5mm (magenta) in steps of 0.5 mm).

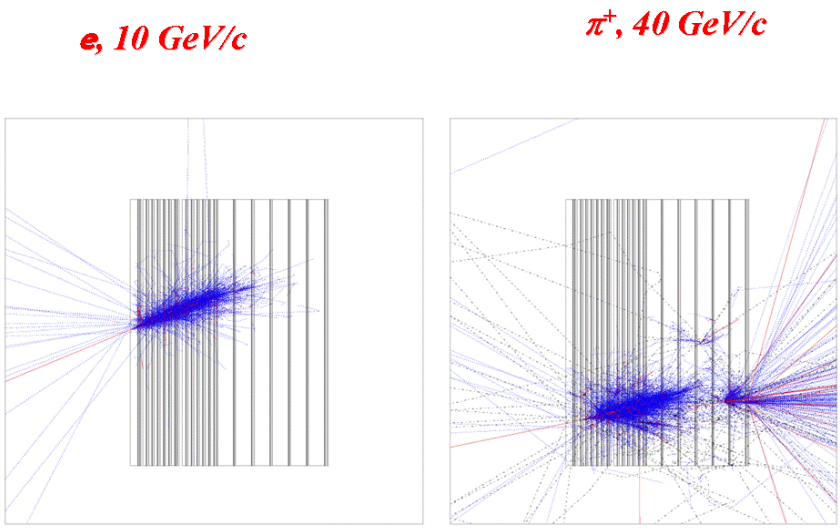

Figure 3.8: Typical electromagnetic (E=10Gev) and hadronic (P=40GeV/c) showers in NoseCone Calorimeter.

In a longitudinally segmented composite calorimeter the sampling fraction (which is a calibration coefficient if electronics gains are ignored) depends on the depth along the shower axis due to an interplay between photon and electron components in the shower and critical energy. The effect is clearly seen in Fig. 3.9 (top panel) where the simulation results for a sampling fraction in three longitudinal segments of NCC and converter are presented.

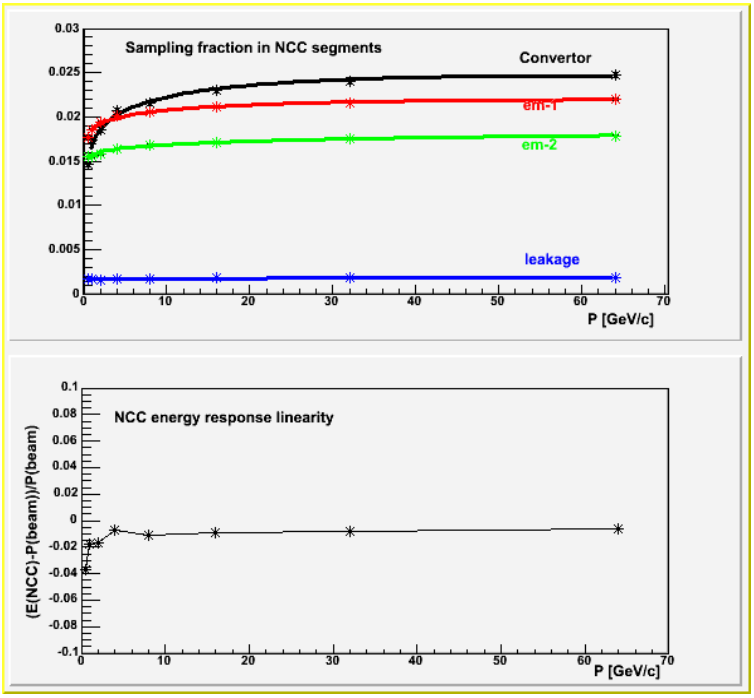

Figure 3.9: Top panel - momentum dependence of the sampling faction value in NCC segments (including converter). Bottom panel- linearity of NCC energy response after all corrections.

A simple functional form was used to describe the behavior observed in the simulated data. When energy dependent calibration coefficients were applied, the calorimeter response was found to be linear within 1% (Fig. 3.9, bottom panel). The momentum dependence of the intrinsic electromagnetic energy resolution of this calorimeter deduced from the simulation data shown in Fig. 3.10 and follows the functional form

$$\frac{\sigma}{E} = \frac{18\%}{\sqrt{E}} + 4\%.$$

The coarse structure of the hadronic segment and upstream converter both contribute a degraded stochastic term (18% compared to 14% prediction based upon Wigmans compilation) and an additional 4% constant term.

Comparable lateral and longitudinal dimensions of the individual sub towers in electromagnetic and hadronic segments allow for independent position measurements in every segment and provide some degree of pointing capabilities. Geometrically very shallow subtowers help to minimize the underlying event contribution to the measured shower energy and improve two shower separation at extreme impact angles.

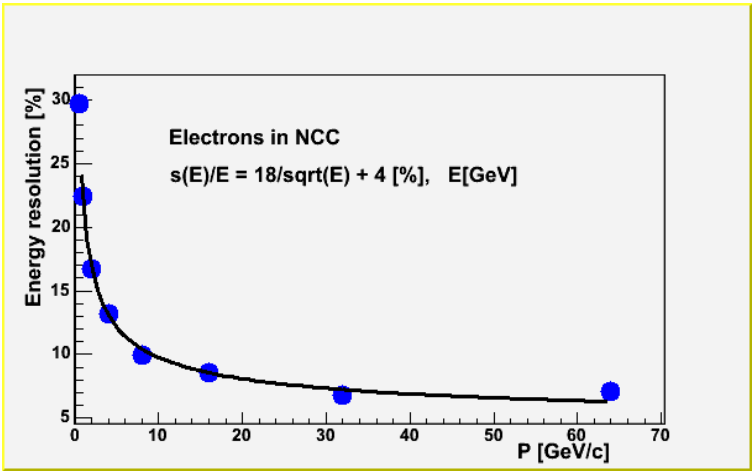

Figure 3.10: The momentum dependence of the intrinsic NCC electromagnetic energy resolution deduced from simulations.

3.4.3 Shower and Hadron Rejection

In the absence of independent momentum measurements for E/P matching, hadron rejection will depend on the momentum distributions of the particles we want to retain and particles we want to reject. At present, the rejection procedure used to test the NCC performance is entirely based upon longitudinal shower shape analysis. Lateral shape analysis will be added at a later stage and is expected to improve results considerably. Electron events were used to compute average energy and variance in every segment. The results were parametrized using simple polynomial functions. The χ^2 value computed ignoring the correlations between segments was used to compare the visible energy distribution in calorimeter to the parametrized one. The probability for pion of momentum P[GeV/c] to fake an electron (integrated over energies of fake electrons) for the different choices of W plate thickness is shown in Fig. 3.11 (plate thickness is color coded in steps of 0.5 mm from 2 mm to 5 mm).

This probability distribution was then convoluted with the hadron spectrum from PYTHIA min-bias events. The data in Fig. 3.12 shows the ratio between the energy spectra of fake electromagnetic showers thus produced and initial hadrons. The points corresponding to different W thickness in EM1 and EM2 are color-coded and connected by lines to guide the eyes. The spread in the values reflects the complexity of estimates due to many orders of magnitude variations to the cross section and a rejection factor with momentum. Similar to spectra modifications discussed in the earlier section, rejection saturates at a W plate thickness around 3 mm. We should remember that this result largely reflects the fact that the decision to use all available space leads to the thickness of W plates in HAD increasing when thinner plates are used in EM1 and EM2.

We conclude this section noting that the saturation effect observed in calorimeter particle identification capabilities when W-plate thickness in EM segments is close to 3 mm is the natural consequence of the initial compromise between cost (number of Si readout layers) and limited total depth of the calorimeter. While further optimization may still result in modifications to the W plate thickness in EM segments, it is unlikely to largely affect

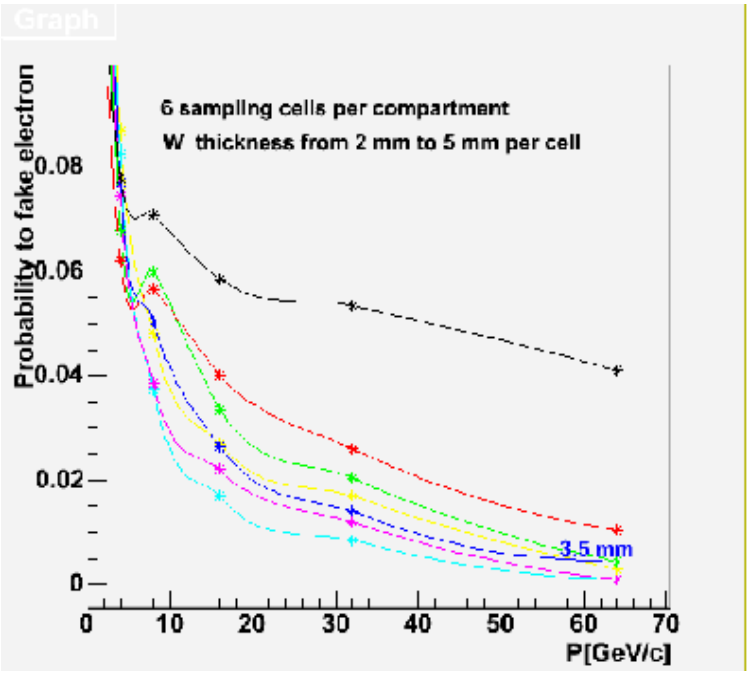

Figure 3.11: Probability for a shower produced by a pion of momentum P[GeV/c] to satisfy electron identification criteria

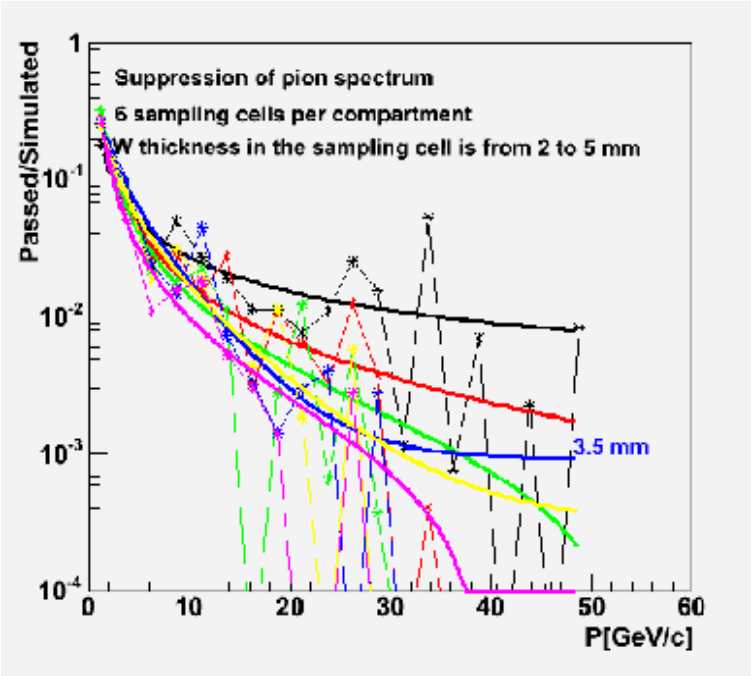

Figure 3.12: Results of the NCC hadron rejection procedure applied to the shower spectrum due to PYTHIA simulated hadronic background. Above 30 GeV the fake electromagnetic showers are $\sim 10^{-3}$ of the inclusive hadronic cross section at a similar momenta.

the ability of calorimeter to suppress hadronic contribution to the electromagnetic showers which is estimated to be ∼99.9% in the momentum range above 20 GeV/c. The hadrons will contribute up to 0.1% of inclusive hadronic cross section to the photon spectra which must be processed through subtraction procedure usually applied to extract direct photon production. The latter value is to be compared to the corresponding numbers for direct photons which can be estimated from PHENIX published data on π^0's and direct photon production in p+p interactions at 200 GeV [8,9]. In the p_T range above 6 GeV/c where direct photon yield exceeds 10% of the π^0 yield (∼5% of the charge hadron yield) fake electromagnetic showers in the proposed NCC are less then 1% of the total hadronic yield corresponding to a direct photon to fake electromagnetic showers ratio better then 10%.

3.4.4 π^0 Reconstruction

One of the major physics channels we would like to study with the NCC is direct photon production in events with a correlated photon-jet in the final state resulting from Compton scattering of a low-x gluon on a quark, where the photon gives us a calibration of the energy and the transverse momentum of the jet. The background to this process is the double-jet final state with one jet fragmenting into a leading π^0 faking a single photon due to shower overlaps. Given the characteristic slope of the shower core ∼0.2 $R_{Moliere}$, the clear separation of the maxima due to two photons with close energies in a detector built of composite material with Moliere radius $R_{Moliere}$ ∼18 mm should be possible down to a similar value of $\Delta \sim 0.2 R_{Moliere}$.

A problem arises when attempting to prove that observed maxima are due to independent showers and not to the shower fluctuations. The separation is too small compared to the average shower radius at the same energy to make meaningful quantitative tests based on lateral shower shape measurements. The following strategy is adopted for the NCC to deal with fluctuations. We are installing two layers of identical 2-d position sensitive detectors (0.5 mm pitch) in the calorimeter at two depths: 2 X_0 and 7 X_0. The first layer (PS), installed downstream of 2 X_0 W converter, is a hit counting layer where position resolution is limited by the strip width to ∼150 μm. The second (SM) layer will serve to measure the decay asymmetry through shower shape analysis at a depth where the shower expands to 1 $R_{Moliere}$ radius. The algorithm will first find all showers in the calorimeter. For every shower it will identify the regions of interest in PS and SM detectors and look for hits in the PS layer to find those showers which may be two overlapping showers. These overlap candidates will be checked for consistency with the hits in the SM layer where the deconvolution will finally be made assuming that the contribution of individual photons is proportional to the peak energy values as measured in the SM detector. Simulations have shown that this approach works well to energies close to 30 GeV (effectively to the limit set by integrated luminosity).

This section summarizes the results of a simulation pattern recognition program to show a proof-of-principal. π^0 events were simulated with a uniform momentum distribution between 1 and 30 GeV/c. Checks were made that only those events with both photons inside NCC aperture are retained. The pattern recognition algorithm used was simple and intended to answer whether the data actually posses the features required to separate single showers

from overlapping showers using this technique. In the detector with Moliere radius ∼18 mm and tower size 15×15 mm^2 decay kinematics implies that a substantial fraction of π^0 decays will yield clearly separated photons. As in the central calorimeter, we consider two showers distinct if their maxima are separated by at least one counter i.e. there is a visible valley between the showers.

A simple clustering algorithm was applied to the hits seen in the longitudinal segments of the calorimeter. The clustering was done separately in all segments. Showers ordered by energies were combined into "tracks" originating from the collision vertex. Whenever the algorithm produced more then one track in the NCC, an attempt was made to compute an effective mass. The comparison of the effective mass distributions for e- and π^0's in multitrack event configurations is shown in the left panel in Fig. 3.13. A scatterplot of the effective mass vs π^0 momentum in "multitrack" events is shown in the right panel.

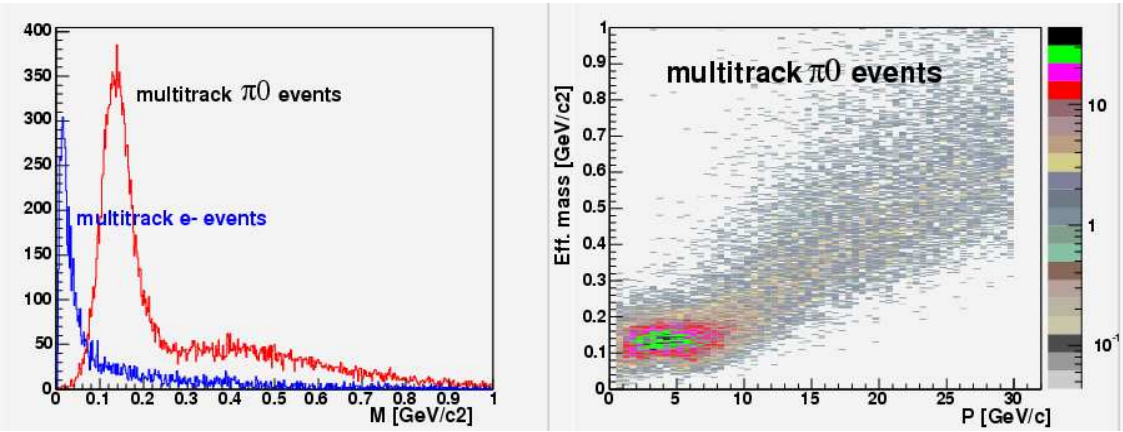

Figure 3.13: Two-shower effective mass distribution in the events with two distinct maxima found in the pattern of deposited energy in NCC.

A clear π_0 signal with a width of $\sim$ 25 MeV/c^2 is seen in π^0 events while the distribution for electron events is totally consistent with background. This approach works reasonably well for π^0 momenta below 7 GeV/c and fails at higher momenta where the showers begin to merge.

The probability to find two distinct showers in the event with both photons from π^0 decay in the detector aperture thus computed is shown in Fig. 3.14.

The events with effective mass outside the two standard deviation window around the π^0 mass as well as single "track" events were further subjected to a reconstruction procedure relying on the pre-shower (PS) detector for shower separation measurements and on the shower-max (SM) detector for decay asymmetry measurements.

All fired strips in the PS and SM detectors were subjected to a simple clustering algorithm which assumed all strips around a local amplitude maxima as being part of a single cluster. For illustration in Fig. 3.15 the hit pattern produced by 7 GeV/c π^0 is shown in the PS and SM detectors.

The multiplicities of fired strips in the two detectors are grossly different. The clusters are obviously separated in both detectors but fluctuations are certainly the limiting factor

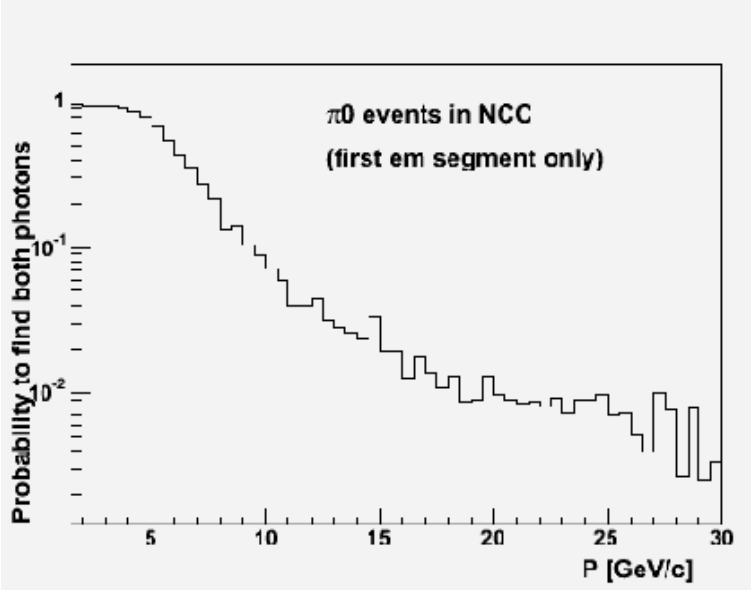

Figure 3.14: Probability to find both showers from π^0 decay as two distinct maxima in NCC vs momentum of π^0.

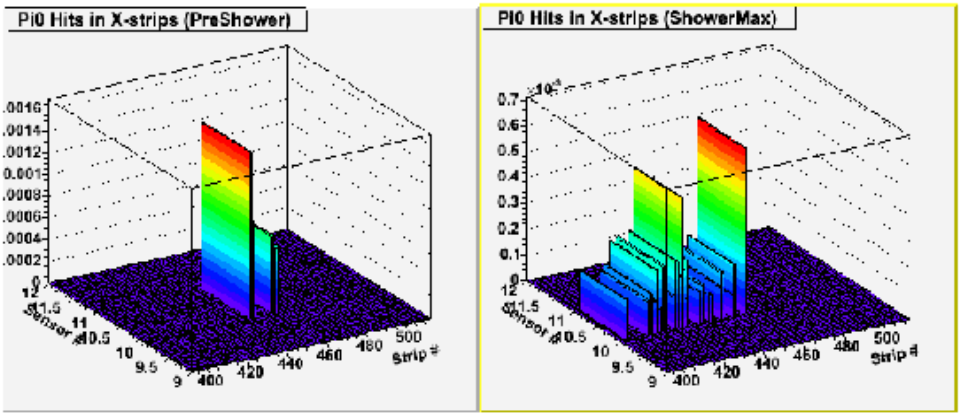

Figure 3.15: Energy patterns in the PreShowr and ShowerMax detectors due to two overlapping photons from 12 GeV/c π^0 decay. (The vertical axis is an energy per strip in GeV).

adversely affecting the resolving power for any simple tests based on cluster multiplicities.

The total energy is obtained from the sum of energies in EM1, EM2 and HAD. The decay opening angle is obtained using hits in the PS detector. The decay asymmetry is obtained from the shower profiles in the SM detector. Once these three factors are known, the effective mass can be computed using formulas based upon trivial decay kinematics. The comparison of the distributions of effective masses reconstructed using this procedure in electron and π^0-events is shown in Fig. 3.16.

The π^0 peak is present in π^0 events only, whereas the distribution for e-events is totally

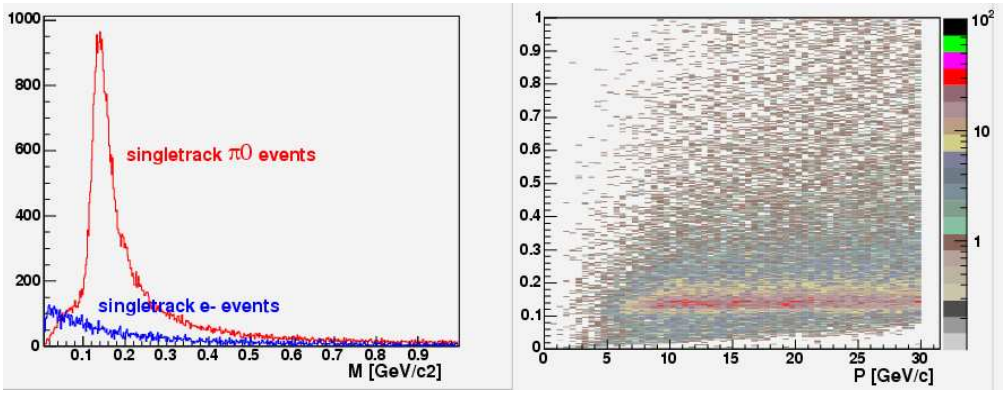

Figure 3.16: Reconstructed effective mass distribution in the events with a single distinct maximum found in the pattern of deposited energy in NCC.

consistent with background. The shape of the π^0 peak as it is reconstructed by this procedure is a subject for further improvements. Currently it has a central peak characterized by $\sigma \sim$ 20 MeV/c2 consistent with detector energy resolution on top of a wide distribution which would usually be considered as a background. The real composition of the peak reflects correlations between the decay asymmetry and the effective mass resolution intrinsic to this approach. While asymmetric decays result in better separated showers, asymmetry measurements in the SM detector get less and less precise when energy in one of the showers decreases. There are also flaws and shortcuts in the current implementation of this procedure resulting in a complete failure to properly reconstruct very asymmetric decays. Addressing such issues will require further development. The losses and failures to reconstruct π^0's by the currently available algorithm are summarized in Fig. 3.17. We expect to make considerable improvements in the algorithm as well as tests using a prototype in a test beam.

Mass cuts 2 standard deviations around the central peak applied to π^0 masses reconstructed in "single track" events result in loosing 50% of π^0's from the peak region. All other losses are within 15% combined. If events producing reconstruction failures are excluded the estimated efficiency of algorithm to reconstruct π^0 both via multitrack and singletrack algorithm in the NCC is shown in Fig. 3.18.

Even at this early stage in the development the efficiency stays above 40% to 30 GeV. For comparison the π^0 reconstruction efficiency in the PHENIX central calorimeters drops to zero around 15 GeV/c.

3.4.5 Jet Measurements

Jets in NCC are an important signature for the hard scattering process and a source of information on the kinematics of the underlying 2→2 scattering. Because of the shallowness of the calorimeter, the percentage of the total jet energy absorbed in NCC drops as function of jet energy and levels up at a value of ∼60% which is essentially the total jet energy converted to electromagnetic component inside NCC (total depth ∼1.6 L_{abs}). (See Fig. 3.19) The energy resolution of the NCC for jet measurements is shown in the right panel. It is

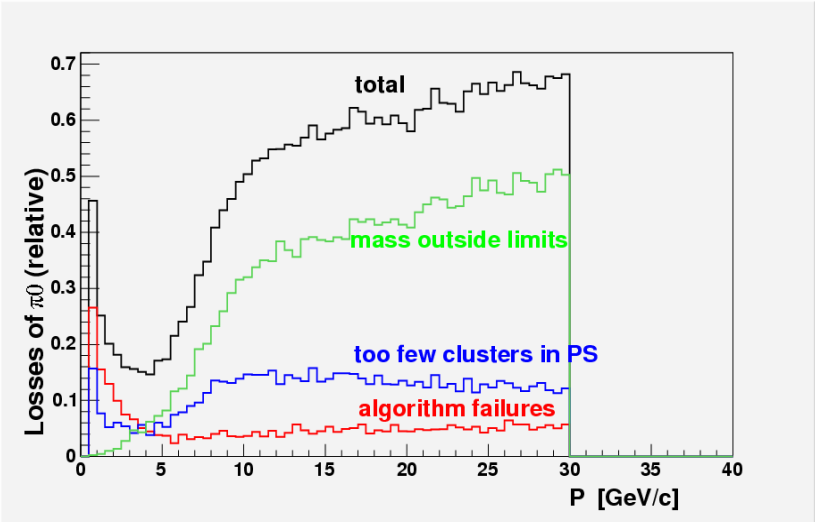

Figure 3.17: Probability for π^0 in NCC to fail in reconstruction or to end up outside 2σ mass window.

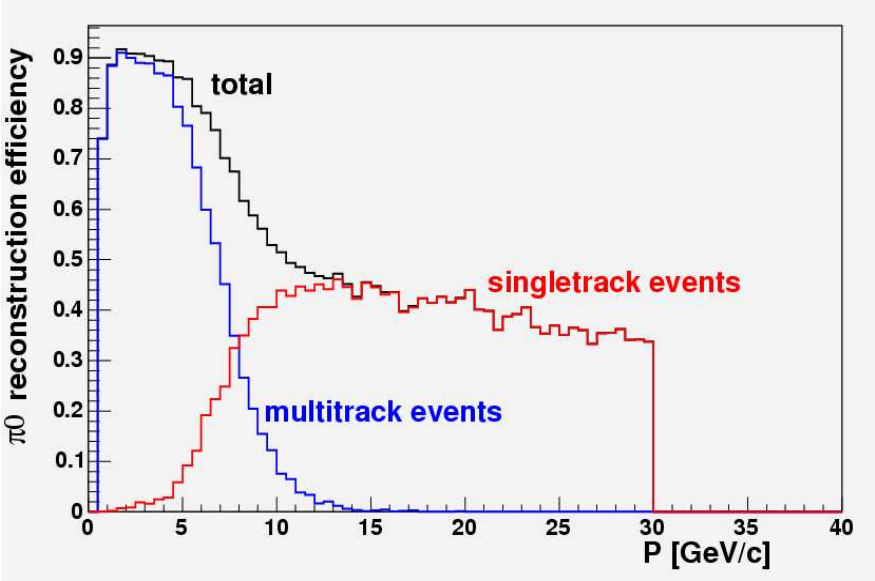

Figure 3.18: Probability for π^0 in NCC to be reconstructed within 2σ mass window.

important to note that at least in case of gluon-quark scattering resulting in a correlated production of direct photon and jet in the forward direction, the measurement of the total jet energy is not required. To reconstruct kinematics of hard scattering measuring the jet 3-vector is sufficient. In general the latter is well represented by the momentum vector of jet electromagnetic component that allows one to build an algorithm relying on an energy pattern in the combined calorimeter for jet finding and energy distribution and EM1 and EM2 for directional vector measurements. The development of this algorithm is ongoing. Its results will be reported at a later stage in the project.

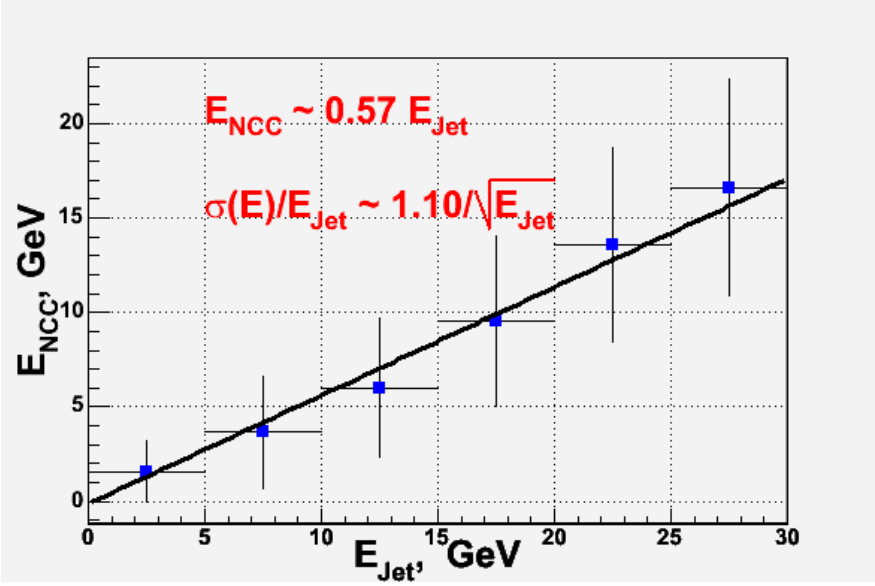

Figure 3.19: Jet energy and its variance as seen in NCC vs PYTHIA jet energy

3.5 NCC Occupancy and Dynamic Range Considerations

In the NCC the energies of showering particles will be shared between the three segments of the calorimeter. In principle this sharing is uneven, with most of the electromagnetic energy deposited in EM2, and most of hadronic energy in HAD. In p+p interactions it is sufficient to set the upper limit of the dynamic range per tower per section to $\sim 60\%$ of the W mass to cover the whole range of physics topics we are planning to study at a 1 TeV collision energy.

Unfortunately in heavy ion collisions, the calorimeter, located only 40 cm from collision vertex, will see a high occupancy environment resulting in hits due to different particles piling up. The potential impact on calorimeter dynamic range was estimated under the assumption that any shower in the calorimeter would always fire a base matrix of 3x3 towers and 3 neighboring strips in SM detector at the peak of the particle density distribution. Strips and towers were assumed to be of a similar surface area ($\sim$200 mm^2). This is grossly exaggerated for the SM detector version as per this proposal. The resulting radial dependence

of the probability to be fired for strips in the SM and towers in the calorimeter is plotted in Fig. 3.20.

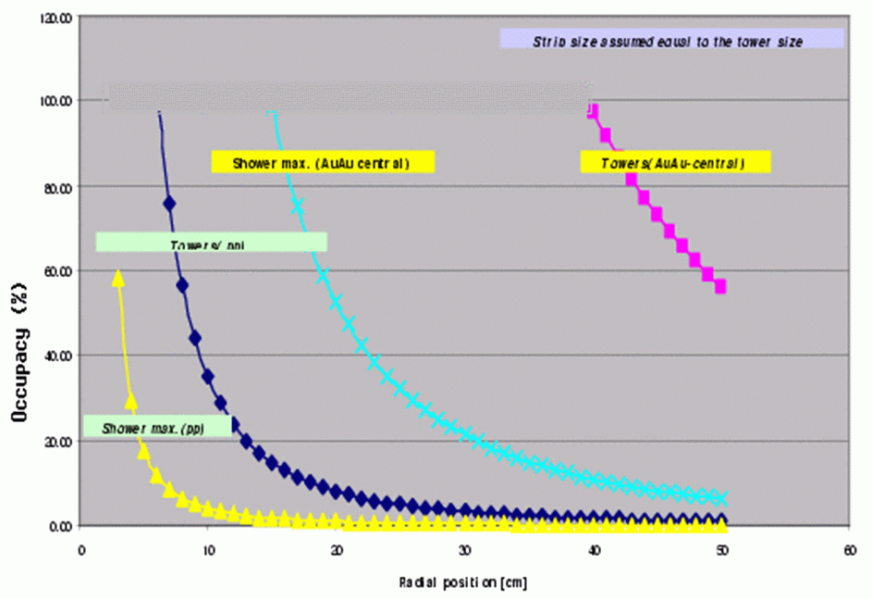

Figure 3.20: Probability for Tower in NCC and strip in SMD to be fired (occupancy) in p+p and Au+Au collisions in PHENIX as function of the distance from the beam pipe.

In p+p collisions, conditions similar to those in the central calorimeter are reached at a radial distance of 10 cm, hence the entire calorimeter area will have a reasonable occupancy. The situation is considerably more challenging in Au+Au collisions where the calorimeter will be heavily occupied by the showers due to soft secondary particles. The SM occupancy still stays relatively low for cluster counting and impact point measurements in the calorimeter allowing jet finding based upon hit occupancy even in the events of highest multiplicity. Energy measurements in Au+Au collisions will be strongly affected by pileup from underlying events resulting in higher threshold values and additional inefficiencies. Similar problems are seen in the present central calorimeters. Jet measurements are certainly the most challenging part of NCC program. Multiple approaches such as threshold selected hit counting, energy profiling and energy flow should be tried. The next figure (Fig. 3.21) illustrates pileup in p+p collisions.

Depending on the rapidity, a 4 GeV/c transverse momentum jet in the NCC acceptance window will have a total energy of 8 GeV to 80 GeV. It will be seen in the calorimeter with very little pileup contribution up to ∼2.5 units of rapidity and will start merging with the underlying event only at rapidity ∼3 or outside NCC acceptance and will have no effect on dynamic range. The outlook for the heavy ion collisions is similar. A typical picture comparing GEANT simulated jet energy to pileup energy within jet cone in midcentral Au+Au collisions is shown in Fig. 3.22

Both jets and pileup contribute equally up to jet-cone energies ∼20 GeV. Larger energies are dominated by jets so the dynamic range of ∼50 GeV per tower per segment suggested

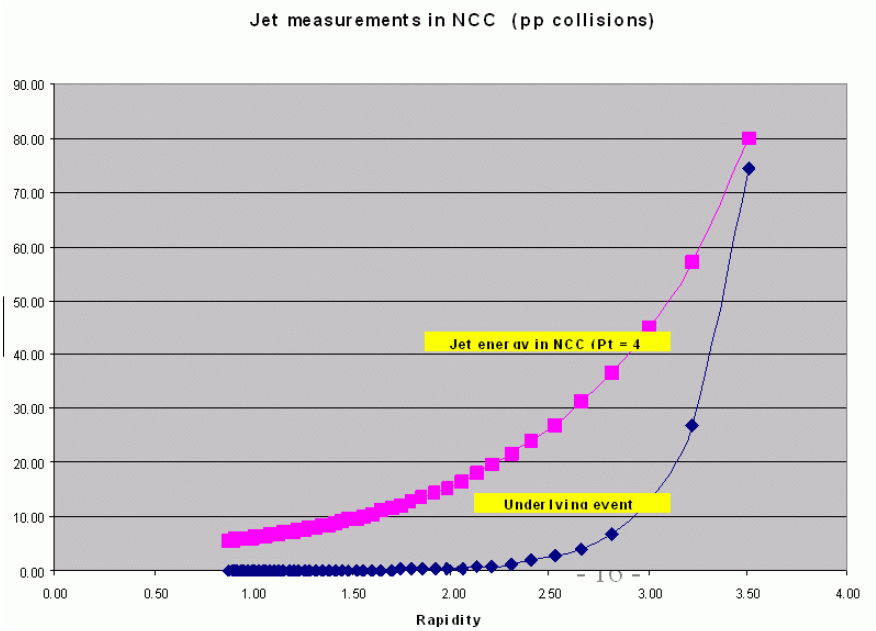

Figure 3.21: Contribution of the underlying event to the energy inside the jet cone in the Nose Cone Calorimeter in p+p collisions at RHIC.

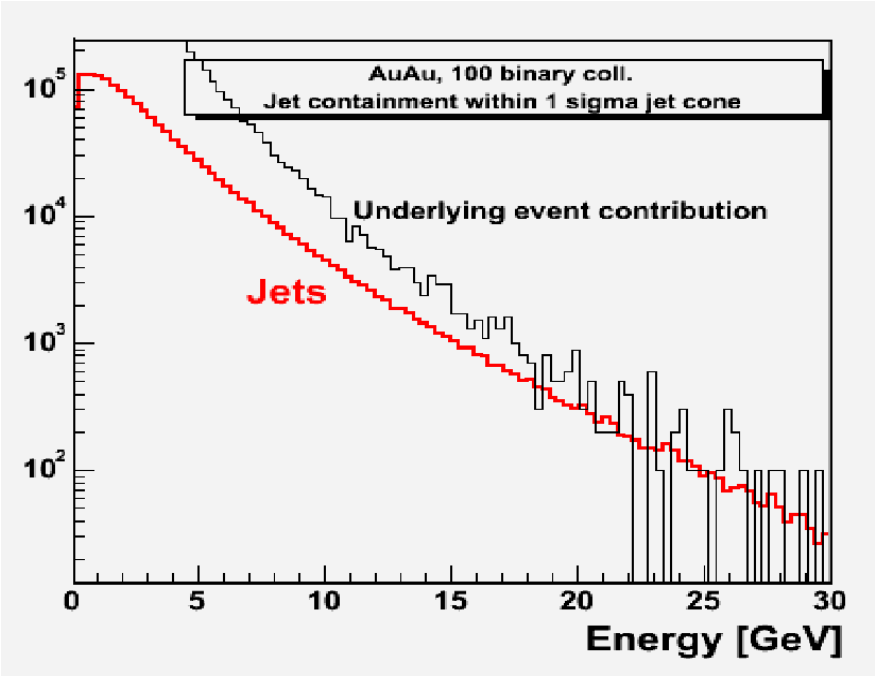

Figure 3.22: Energy distribution of high p_T jets in calorimeter (red histogram) compared to pileup energy distribution inside jet cone in midcentral events in Au+Au collisions at RHIC energies.

for W-measurements should be totally appropriate to cover the whole range of NCC physics.

3.6 NCC Mechanical Design

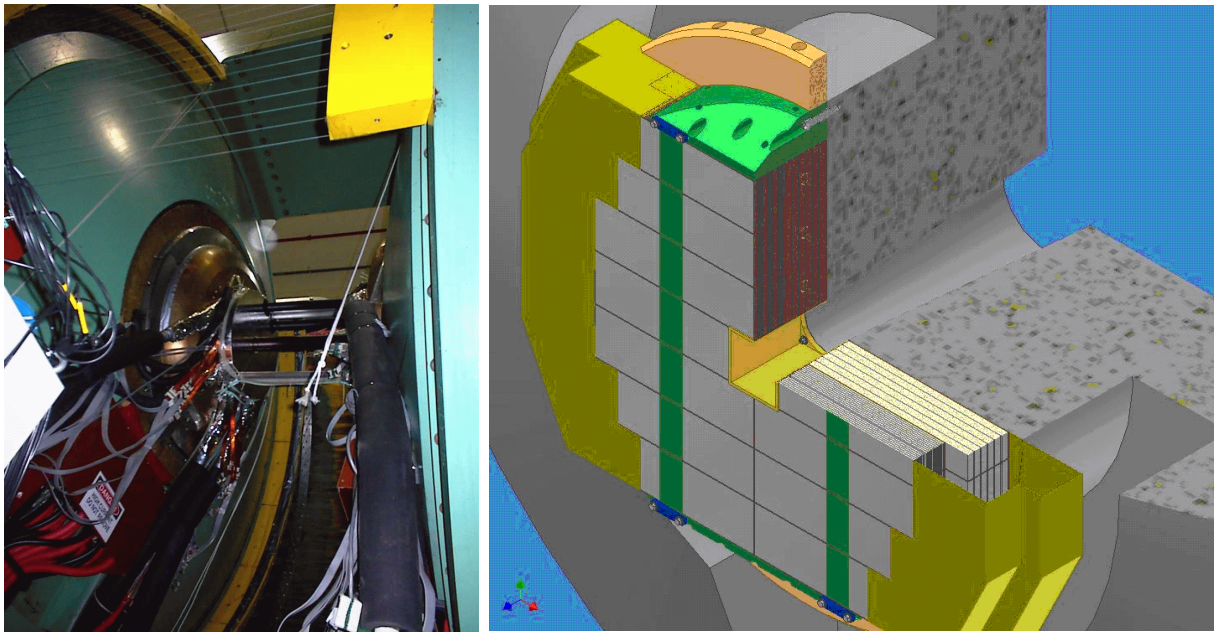

Figure 3.23: PHENIX Nose Cone (left panel). Nose Cone Calorimeter (right panel). Boxes upstream are electromagnetic segments (EM1 and EM2), downstream boxes are HAD. Air plenums housing preamplifiers are also shown.

A modular NCC design will be used in the mechanical structure of the NCC as illustrated in Fig. 3.23. The calorimeter is designed of "bricks". Two kinds of bricks (see Fig. 3.24) are used to build two quasi-independent calorimeters: the electromagnetic (EM1 and EM2) and hadronic (HAD). All bricks are a single silicon sensor wide. There are three standards for the brick length in the electromagnetic and hadronic sections (7/6/5 sensors in HAD, 6/5/4 sensors in EM1 and EM2). The electromagnetic bricks are much more demanding in terms of the readout as compared to the hadronic bricks. Electromagnetic bricks are composed of the tungsten converter, preshower detector (PS), shower max detector (SM) and two electromagnetic segments (EM1 and EM2). A hadronic brick will consist of a single hadronic segment. Each brick has a W plate facing upstream and Cu skin enclosing it on all other sides save one for connections to external electronics boards.

When assembled, the bricks will form two vertical walls and small locking pins will be used to maintain the geometry. For mechanical reasons the two walls will have the same size vertically, giving up some of the acceptance of HAD. Horizontally the hadronic wall is two sensors wider compared to electromagnetic wall. This geometry allows us to minimize the cost while keeping all particles originating from the collision point and are currently stopped by the brass nosecones within calorimeter structure. The calorimeter walls are supported by

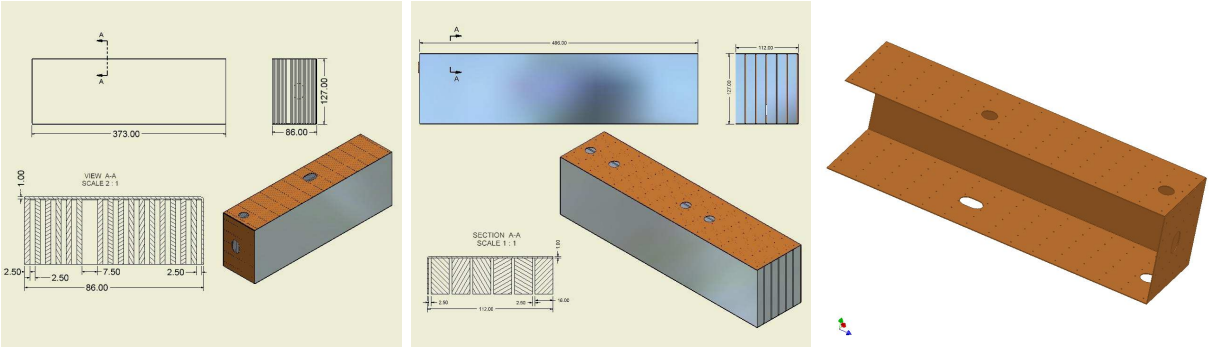

Figure 3.24: NCC building bricks. (left) electromagnetic [wide gaps indicate locations for preshower and shower max detectors], (center) hadronic, (right) Cu skin for the electromagnetic brick.

two shelves above and below, and thin pretensioned front braces (strips of stainless steel or Kevlar) preventing the walls from buckling outward.

3.7 NCC Silicon Sensors

The main requirements for the silicon detectors in the calorimeter are reliability, precise shower energy measurements via charge measurements in silicon, precise tracking measurements, and radiation hardness. The pad size chosen for the NCC is 1.5x1.5 cm^2. The strip size for PS and SM is 0.5x60 mm^2. All silicon detectors in the NCC are 6x6 cm^2 diced from 4" wafers 525 mm thick for pad sensors and 600 mm thick in the case of the stripixels. Critical to the success of the experiment will be reliable operation of these sensors in a radiation environment. The estimates based upon total energy flow simulation predict the total fluence of 100 kRad (in Si) or about $3x10^{12}$ equivalent neutrons per cm^2 over the period of 10 years (assuming p+p interactions at 200 GeV with luminosity $\sim 2x10^{32}s^{-1}cm^{-2}$). For a pad size of the order of a few cm^2 and 300 mkm sensor thickness, published data predict the leakage current of the order of 5-10 mkA per pad. Handling this value of current requires decoupling capacitances between pads and preamplifiers.

For the operation of the detectors the control of leakage current is important because of the increased noise. Leakage current may also result in increased bulk heat production in silicon which may lead to thermal breakdown if the silicon detector is not cooled. In our design of sensors and selection of raw material we were guided by the experience and work done within the scope of the D0 (FNAL) and ALICE (LHC) projects and recent published data from the research and development in radiation hard silicon technology. In particular we followed few simple rules:

- Single sided sensors from established vendors to insure higher yields and less trouble due to the simplicity of the design. It is also well known that double sided sensors suffer more radiation damage,

- A minimal number of different sensor designs (only two in the NCC case). Design

to successful completion of the project using a single vendor. Transfer the design to additional vendors when ready. This will speed production,

- Use short strips to reduce the number of ghosts hits to avoid creating pattern recognition problems. We use 4" wafers only,
- Avoid double metalization,
- Specially designed guard ring structures. Such guard rings are important in order to keep breakdown voltage before and after irradiation as high as possible.

In short, for the construction of the Nose Cone Calorimeters we will use single-sided single-metal p+ on n- bulk silicon devices. Integrated polysilicon resistors will be included on the stripixel sensors to simplify the test procedures (sensor can be fully depleted using two lines only) and to minimize the real estate used by external RC chains to DC coupled detectors to readout electronics. Two kinds of sensors are used to construct the NCC's: pad structured and pixilated strips. They both will be described in more detail below. The technology of pad structured sensors is well tested. We have three established vendors ready to manufacture the 6x6 cm^2 pad-structured sensors using common design files, corrected for specifics of technology. The pixilated strips (stripixels) are novel detectors developed at BNL and currently selected as a base design for the silicon sensors in another of the PHENIX upgrades - the central silicon tracker. The design chosen by PHENIX are interleaved stripixel detectors where each pixel is divided into two parts: X-cell (or pixel) and Y-cell. X-strips and Y-strips connect X-cells and Y-cells, respectively, in a strip detector readout scheme. In this detector two dimensional (2D) position sensitivity is achieved with single-sided processing. A short summary of sensor parameters is given in Table 3.2.

Both pad sensors and stripixels have been prototyped at ELMA (Russia) and are currently being tested. We briefly review the design of the sensors and related infrastructure in this section. R&D results are presented in a separate section of this document.

3.8 Pad-Structured Sensors and Pad-Structured Readout Layers

The pad structured Si layers (18 in total) are built of 6x6 cm^2 silicon detectors subdivided into 16 identical square cross section pads (diodes).

The sensors will be mounted on pc boards. Sensors, carrier boards and interconnects (see Fig. 3.25) form the readout unit which is installed in the gap between W plates. The position is defined by locking pins on the side opposite to sensors.

The interplate gap reserved for readout unit is 2.5 mm thick. 0.5 mm of this space is silicon, ∼1.4 mm is FR4 (motherboard), 0.2 mm is the FR4 interconnect, another 0.2 mm is the FR4 spacer required to control the height of low temperature solder between interconnect board and carrier board. The remaining ∼0.2 mm gap is to insure that no pressure is applied to the surface of Si sensors. Such pressure may result in increased noise due to the piezoelectric effect.

Specifications	Pad-structured sensors	Stripixel sensors
Wafer thickness	525 mm	600 mm
Depletion voltage	100-120 V	130 – 155 V
Diod capacitance	37 - 41 pF	
Bias voltage	Full dep. V + 20V	Full dep. V + 20V
Leakage current	< 300nA total, <20nA/pad	< 1?A total
Junction breakdown	> 300V	> 300V
Implant area	15 x 15 mm2	TBD
Al area	15.02 x 15.02 mm2	15-60 mm prototyped. Decision pending.
Polysilicon bias resistor	1 m?	1 m?
Interpad (strip) capacitance	< 2pF (pad-pad) or < 8 pF (pad-all neighbors)	TBD
Maximum heat dissipation from the bulk material	< 50 ?W	< 100 ?W
Heat dissipation from on-the-sensor electronics	-	TBD

Table 3.2: NCC Silicon Sensor parameters

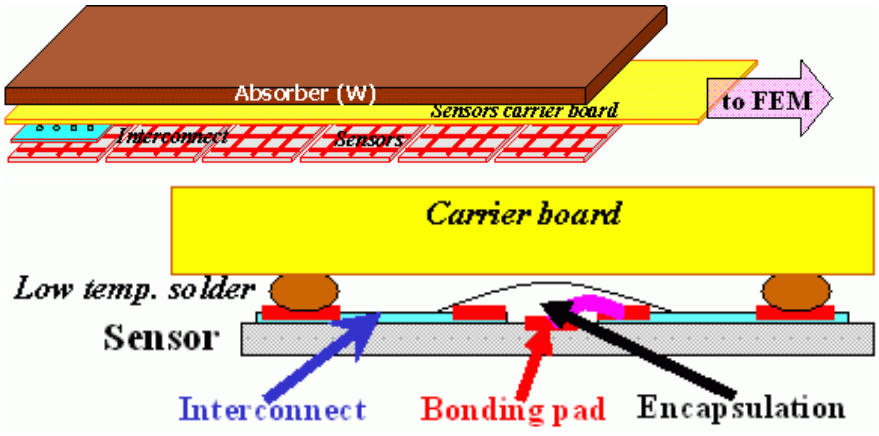

Figure 3.25: NCC Readout unit structure. Details of the sensor installation scheme are in the bottom part of the picture.

This particular design is considered (we are still working on testing different implementations) for ease of repair of the assembled readout unit. Soldering points are connected to the bonding pads via traces allowing them to to be located around the center of the interconnect board. If a sensor fails it can be removed with its interconnect board from the carrier board by heating just the central area of the sensor. A new sensor-interconnect board assembly can then be installed.

The NCC will use five different readout units: all a single sensor wide with the number

of sensors varying between 3 and 7.

3.9 Stripixel Sensors and Stripixel Readout Layers

We have chosen a novel detector of interleaved pixilated strips ("stripixel") developed at BNL and already in use for the Central VTX in PHENIX. This novel detector generates X-Y two dimensional position sensitivity with a single-sided processing and readout. Fig. 3.26 is an illustration of the concept. It consists of a comb shaped structure with 250 μm prongs cover a pixel area of 500x500 mm^2. Prongs are interleaved with similar prongs from two overlapping pixels on the right and on the left.

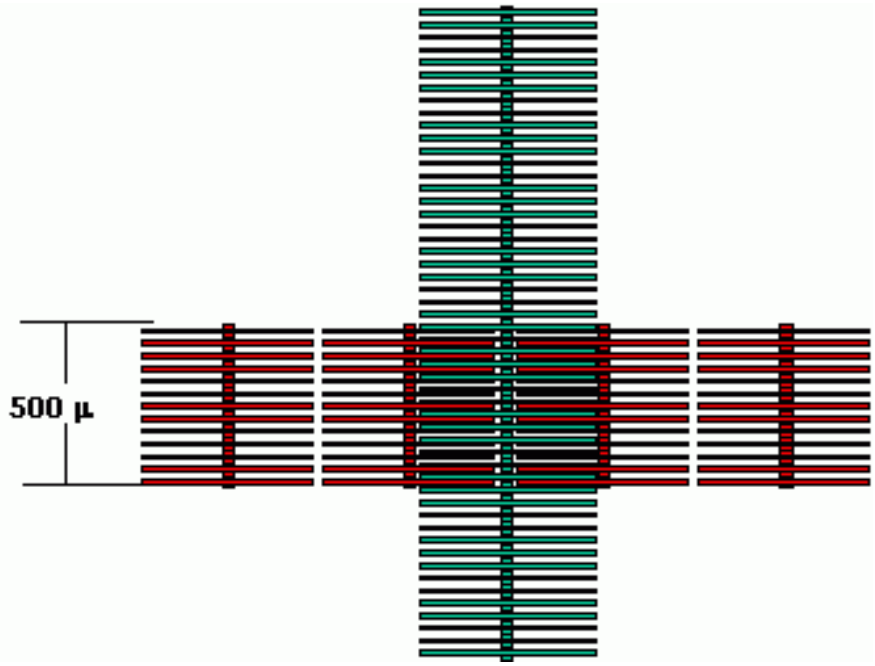

Figure 3.26: Design of the detector with interleaved pixilated strips with 2-d position sensitivity. Ionization charge produced by charged particles in Si is shared between X and Y oriented strips.

Alternate combs are connected either in the X direction (for measurement of the Y coordinate) or in the Y direction (for measurement of the X coordinate). The pitch between prongs belonging to different strips is chosen comparable to charge diffusion to insure uniform charge sharing. While it is easy to predict that an optimal pitch for a 525 μm wafer must be in the range of 15 mm, it may still be affected by the comb geometry and will need prototyping to optimize the pitch. Other critical issues are interpixel connections and crosstalk, the latter depends on the total length of the strip edge which in turn is correlated to the pitch. While the PHENIX central VTX employs double metal technology for interpixel interconnects, it may be advantageous for the NCC to use n+ implants to create conductive regions in the

bulk silicon separated from Al with a layer of SiO2. This technology may have better promise for radiation hardness.

The readout system for the stripixel silicon detectors will be based on the SVX4 chip developed at FNAL for the D0-detector Upgrade and the existing PHENIX data acquisition system. Strips are connected to Data Collection Modules (part of the PHENIX DAQ system) through hybrids with an RC network and SVX4 chips daisy chained and followed by an interface board with a sequencer which are in turn connected to DCM's. The hybrids will be glued directly onto the sensors with the common of the sensor glued to the carrier board.

Preliminary results of R&D work on StriPixel structures and a detailed proposal for readout electronics for StriPixel NCC layers developed in collaboration between the BNL NCC group, the BNL Instrumentation Department and JINR LHE (Dubna) group can be found below in the section on NCC Research and Development and in an addendum to this CDR.

3.10 NCC Electronics

3.11 NCC Analog Signal Processing

For readout purposes the calorimeter is longitudinally segmented into two fine and one coarse segments and two 2-D sensitive coordinate layers. In total the silicon tungsten calorimeter as it was described above will have close to 60 000 silicon pixels and 80 000 strips. This calls for a compact, economical readout. The block diagram of the NCC analog signal processing plant is shown in Fig. 3.27.

Depending on the location in the calorimeter the readout unit will deliver between 48 and 112 signal lines to the preamplifier board. In order to minimize the number of individually designed components in the detector, we are planning to use the same design of the adapter board everywhere with only live channels populated.

As previously mentioned we will sum up pixels in each longitudinal segment of the calorimeter. A simple passive (on the resistors) summation scheme will be implemented on the outskirts of the detector. Signals from individual pixels are sent to the summer via traces on the carrier board. The rather modest goals for the electromagnetic energy resolution allow us to disregard the potential contribution to resolution due to the spread in the gains between individual channels. Summed signals are amplified using hybrid line terminating amplifiers developed at BNL for the ATLAS liquid argon calorimeter. Modifications to the existing design will include polarity change for all transistors (to work for positive swing signals) and the addition of differential drivers to drive the signals over twisted pairs cables to the digital signal processing plant.

The silicon carrier boards and readout motherboard with preamp, shaper and analog driver daughterboards will comprise the analog portion of the NCC readout electronics. The carrier boards are connected to the motherboard via flexible polyimide cables. The motherboard hosts a preamp, shaper and differential drivers arranged as three rows of nineteen daughter boards each.

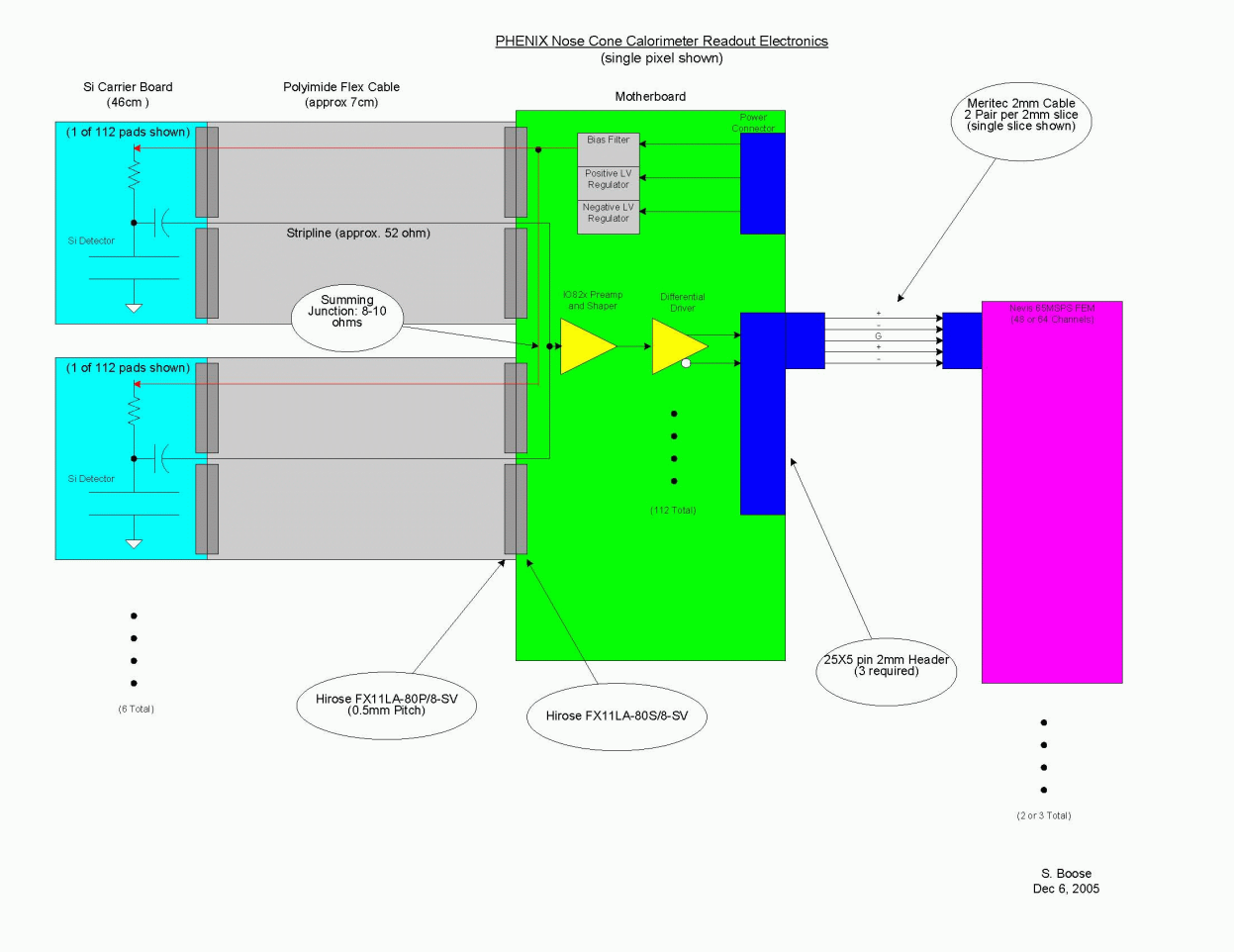

Figure 3.27: NCC analog signal processing block-diagram

3.11.1 Silicon Carrier Board

Each silicon carrier board is 460mm long by 64mm in width by 1.6mm thick and mounted at a 5.5 mm pitch with its neighbor in a stack of six carrier boards. Each carrier board can host up to 7 silicon sensors with 16 pads each for up to 112 signals. The outer end of the carrier board has two 80 pin, 2mm stacking height connectors for connecting output signals and input bias voltages.

3.11.2 Flexible Cables

Flexible Polyimide cables connect output signals via stripline from the carrier board to the preamps and bias voltages from the motherboard to the carrier board.

3.11.3 Motherboard

The motherboard contains up to 112 channels of hybrid preamp circuitry, shapers and corresponding differential output drivers, low dropout regulators and connectors for signals and power. Hybrid preamp boards, shaper boards and driver boards are removable for servicing. The differential output connector is a 2mm header that will accept the Meritec shielded pair cables to be used by the Nevis Front End Modules which will do the signal digitization. Low voltage supply inputs are regulated down to the required preamp, shaper and driver voltages by local low dropout regulators.

3.11.4 Hybrid Preamplifier

Each preamp daughterboard is 35mm x 53mm and handles six channels, providing 112 channels when arranged vertically in rows of 19. This is an expanded version of the 4 channel BNL IO82x Line Terminating Amplifier. The power dissipation is < 100mW per channel.

3.12 NCC Digital Signal Processing

3.12.1 Calorimeter FEM

The NCC Front-end Module (FEM) has the function of receiving the NCC preamp signals, digitizing the signals and sending them to Data Collection Module (DCM) and NCC local level 1 modules (LL1). The FEM will be hosted in the 6U VME crates located near the detectors. Each FEM will receive 48 channels of signals. A custom dataway will be used as a bus for the serial data and chain FEM data between adjacent modules. A crate interface module will serve to interface with the PHENIX granule timing module (GTM) as well as to the PHENIX slowdownload interface. The level 0 (L0) and level 1 (L1) timing signals and serial data will be generated from the interface module and sent to the FEM.

The amplified differential signals will be driven from the detector to the FEM through 2mm Hard Metric (HM) cables. The cable is made from 2 isolated 26 gauge parallel wires with overall shield and 100 ohms impedance. The 2mm HM connector, has 5 pins per row and can host 2 signal pairs plus central ground pin per row. The overall block diagram for the FEM is shown in Fig. 3.28

. The cable receiver, as shown in Fig. 3.27, will receive, shape and drive the signal the differentially to the ADC. Final gain adjustment can be done by changing the feedback resistors. An 8 channel 65MHz 12-bit ADC will be used to digitize the signal. The ADC will sample the signal 6 times per RHIC beam crossing, 6x9.4MHz. Ignoring the voltage shift of the ADC, the full range the ADC is +1V to -1V. The amplifier and receiver arrangement can only swing the voltage from 0V in a positive direction. We will get 11 of 12 bits ADC. With the current gain setting, The ADC data is serialized using a 12 times sampling clock, 720MHz. An FPGA will be used to receive the serial data. The same FPGA will provide the 40 beam crossing L1 delay buffers, 5 L1 trigger event buffers and data format. Upon receive L1 trigger, 12 samples of data per channel will output to the DCM with a 6 times

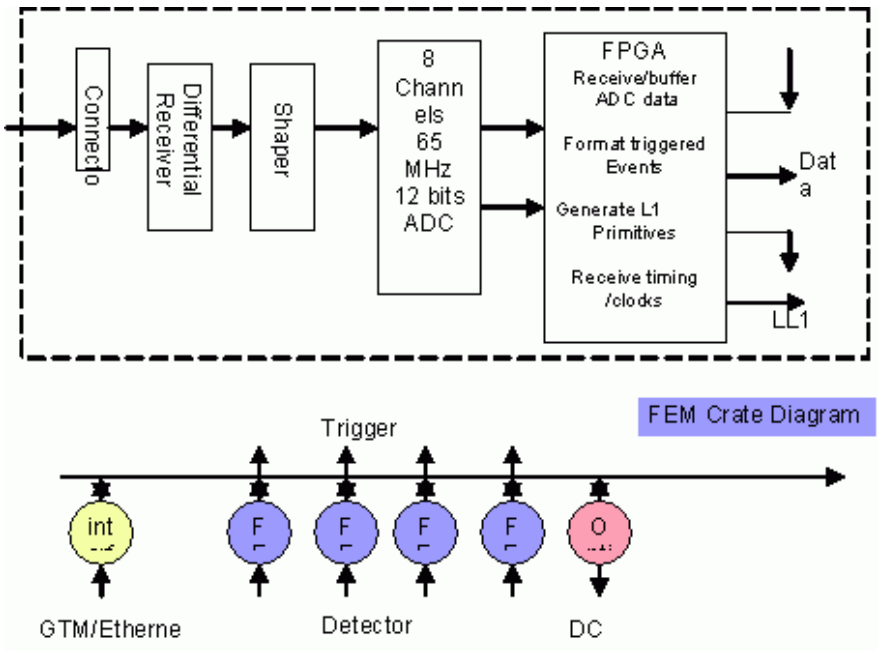

Figure 3.28: Digital signal processing in NCC

beam crossing clock. The data output of FEMs will be connected through a token passing dataway. An optical output will generate every 4 module to DCM.

3.13 NCC Based Event Triggering

In order to pursue it's rare-event physics program the PHENIX experiment requires high luminosity from the RHIC accelerator and highly selective Level-1 and Level-2 trigger systems. In particular, the Level-1 trigger system is limited to a maximum rate of 12.5kHz by the readout rate of the detector front-end electronics. This will require an overall event rejection of up to ∼1000 when RHIC reaches its goal of ten times design luminosity for protons in future run. Since we anticipate the parallel acquisition of several rare event channels, the rejection for an individual trigger channel must be larger by a factor 5-10.

The PHENIX Level-1 trigger is fully pipelined and provides an event decision in less than 4.2μs (40 RHIC clock ticks). The Level-1 Trigger consists of two separate subsystems. The Local Level-1 (LL1) systems communicate directly with the participating detector systems. The input data from these detector systems is processed by the LL1 algorithms to produce a set of reduced-bit input primitive data for each RHIC beam crossing. The Global Level-1 system receives and combines this data to provide a trigger decision. In addition, busy signals (both global and trigger) are managed by GL1. The PHENIX detector system readout is divided into two sets of elements: granules and partitions. A granule is the smallest detector element that communicates with the PHENIX timing and control system via a Granule Timing Module (GTM). The GTMs distribute the local 9.4Mhz RHIC beam clock as well as control bits and event accepts to the granule. A partition is an administrative configuration

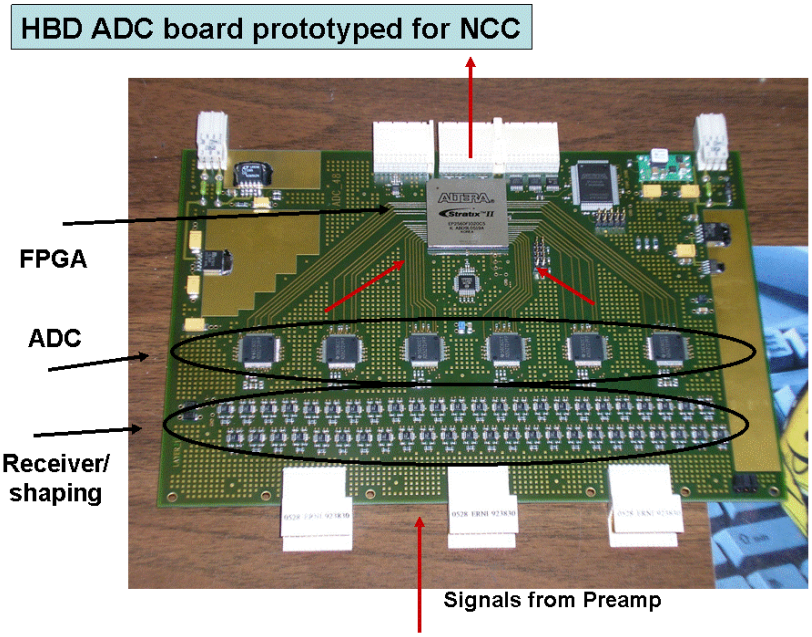

Figure 3.29: ADC board prototype for the NCC

of granules that share both busy signals and Level-1 triggers.

In this PHENIX upgrade the NCC LL1 primitive system will generate primitive information on the jet axes, as well as single and multiple high energy clusters. An upgraded muon LL1 trigger system will generate primitive information on the momentum of high p_T tracks, while a potential upgrade to provide the Si tracking coverage over the acceptance of the PHENIX muon arms will allow identification tracks with displaced vertices. In order to maximize the trigger rejection at Level-1 it will be necessary to combine trigger information from all of the forward Level-1 systems. To accomplish this, a new regional trigger processor will then take the complex trigger primitive information from the nosecone calorimeters, muon tracking system and muon identifiers, combine the individual detector LL1 primitives, make trigger decisions and send them to GL-1. A block diagram of the data flow is shown in Fig. 3.30.

The existing MuID LL1 system is based on a generic, configurable LL1 trigger board designed and built by Iowa State University, and is a prototype for the development of the NCC Level-1 trigger. The Generic Local Level-1 hardware (GenLL1) was designed to address a number of difficulties faced in extending the original design concepts for LL1 systems to address the full range of PHENIX trigger needs. First, the hardware had to be re-programmable to allow not only quick corrections to the trigger logic, but modifications of the trigger system as the PHENIX physics program evolved. This also had the added advantage of lowering development costs and allowing quicker prototyping of new trigger systems. Second, the new hardware had to be able to manage a data throughput of ∼20Gb/s in order to be able to handle large data volume detectors (such as the Muon Identifier) without prohibitive cross-stitching between multiple boards (and crates of boards). Finally, in order

to keep power consumption and heat load on the board within reasonable limits the GenLL1 design was required to use the next generation of HP GLINK receiver/transmitter logic (the HDMP 1032/1034), which runs at 3.3V. Smaller format transceivers (Agilent HFBR 5912) were also required in order to be able to handle up to twenty fiber inputs on a single 9U VME board.

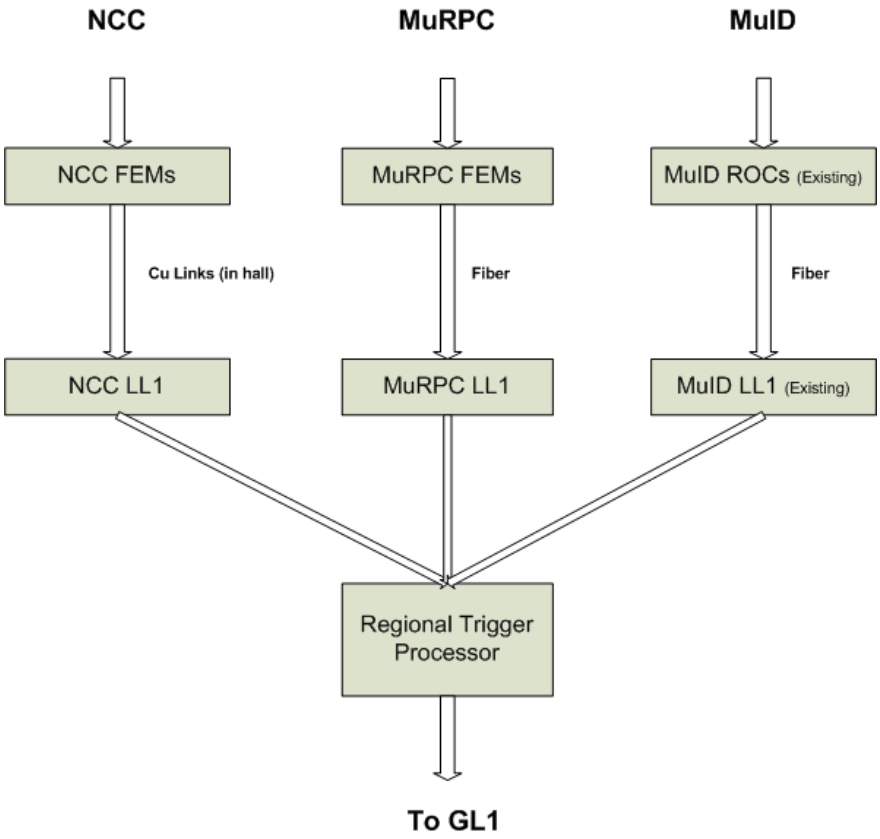

Figure 3.30: Block diagram of the combined forward PHENIX Level-1 trigger system showing the nosecone calorimeter, NCC, trigger muon tracker stations and the existing MuID LL1 system for a single PHENIX muon arm. In order to combine the primitives of the various trigger systems a regional trigger processor will combine the trigger information before sending primitives to Global Level-1.

3.14 The NCC Level-1 Trigger System

The nosecone calorimeter (NCC) will use a Local Level-1 (LL1) trigger to select events via with a high p_T photon or jet in the calorimeter acceptance. As is typical of PHENIX LL1 systems the processing will consist of a set of pipelined stages. First, a set of primitive data will be digitized on the front-end modules (FEMs). Second, this data will be transferred to an LL1 system, and finally the bit-reduced trigger information is sent from the LL1 system

to the PHENIX Global Level-1 trigger system, possibly via a new regional trigger processor to combine Level-1 information from the different forward detector systems as described in the previous section.

The NCC system consists of over 10k channels of analog data per nosecone spread over three layers in depth. The FEMs digitize the analog pad output, and pass the LL1 system an 8-bit ADC value per pad. The 8 bits per channel will allow a ∼100 MeV least count with a full range of 100 GeV, and will result in an aggregate bandwidth of 1,200Gbit/s per nosecone into the LL1 system, roughly a factor of 15x larger than the data processing capacity of the existing MuID LL1 trigger system. Simulations have shown that sufficient resolution can be obtained at LL1 with eight bit digitization per pad. In addition, we are considering the possibility that the FEMs could digitize data in 2x2 granularities to further reduce the data transfer into LL1.

Because of the large data volume and tight space constraints on the detector FEMs we are considering the possibility of transferring the data over high-speed serial links into an LL1 system located in the detector hall, as opposed to other LL1 systems that transmit their data over optical fiber links to LL1 electronics in the PHENIX rack room. The advantage of this approach would be that with serial links we could concentrate the entire NCC LL1 data stream into a smaller number of LL1 modules, simplifying the data cross-stitching required for trigger tile algorithms. This would only be possible by using high-speed copper serial links between the detector FEMs and the LL1 electronics which are inherently short-range, requiring the LL1 electronics to be located in the detector hall.

The LL1 system will aggregate the NCC pad data and form two types of tile for trigger processing. The first, a set of 2x2 tower non-overlapping trigger tiles will be available for prescaled triggering at very low p_T. The second set will be a collection of overlapping 8x8 tower overlapping trigger tiles. The 8x8 overlapping size was chosen to fully contain high p_T electromagnetic showers as well as a good match the the η width of a jet of hadrons. For both the 2x2 and 8x8 triggers the algorithm will begin by examining the relevant trigger tile in the EM2 section of the calorimeter. If energy is found in the EM2 tile, a corresponding tile is constructed in the EM1 and HAD calorimeter sections based on the center of the trigger tile in EM2 and the assumption that the incident energy came from a vertex location at $z = 0$. This "steering" in theta angle accounts for the fact that particles do not enter the NCC at normal incidence.

A sum is formed from the trigger tile energies in the EM1, EM2 and HAD sections, and this energy sum is compared to a threshold based on the desired E_T trigger threshold and the theta angle of the trigger tile in the EM2 section. In this way the total energy threshold varies as a function of theta in such a way as to keep the E_T threshold approximately constant. If the energy is above threshold, a trigger bit is set in the reduced bit output to Global Level-1. The reduced bit output of the NCC LL1 trigger, in the form of a set of bits indicating satisfied algorithms, would be transmitted to the GL1 system over optical fiber.

In order to separate electromagnetic from hadronic showers using the 8x8 trigger tiles, and additional selection is made based on the fraction of the total shower energy that is in the HAD calorimeter section, HAD/(EM1 + EM2). If this ratio is less than one, the trigger tile is tagged as an 8x8EM trigger. Simulation studies show that this separation in 99%

efficient for high energy photon showers. Note that the 8x8 trigger is inclusive of the 8x8EM trigger.

Studies of the anticipated rejection from the NCC LL1 have been done using the simulated events and the PHENIX detector simulation application (pisa). For proton-proton collisions at $\sqrt{s}$ = 500GeV, approximately one million minimum bias events were generated and simulated in the PHENIX apparatus. Rejection factors for the 8x8 and 8x8EM trigger tiles were calculated, and are shown in Fig. 3.31. A table of the rejection factors is available in Table 3.14. We note that rejections in the range of 10000 for the 8x8EM trigger can be obtained with an E_T threshold between 10-12.5 GeV.

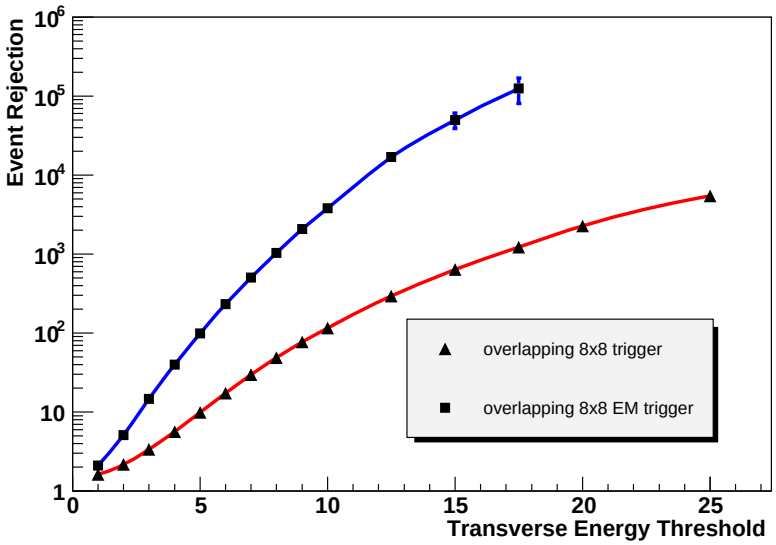

Figure 3.31: Anticipated NCC LL1 rejection factors of minimum bias proton-proton collisions at $\sqrt{s}$ = 500GeV for the 8x8EM and 8x8 trigger tiles, as described in the text.

In order to examine the expected event rejection in heavy ion collisions, the event generator Hijing was used. To cover the full range of potential colliding species at RHIC we chose to simulate AuAu, CuCu and SiSi collisions. The expected rejection factors for the 8x8EM and 8x8 trigger tiles are shown in Fig. 3.32 and Fig. 3.33. As expected, substantial event selectivity can be obtained for collisions of light ions, but the very high overall multiplicity in Au+Au collisions limits the overall rejection that can be achieved. The rejection factors are shown in tabular form in Table 3.14. These results are based on simulations of 500 events for AuAu, 1600 events for CuCu, and 3700 events for SiSi.

Finally, we examined the expected event rejection in d+Au collisions (again using the event generator Hijing). The expected rejection factors for the 8x8EM and 8x8 trigger tiles are shown in Fig. 3.34 and Fig. 3.35, with the rejection for each arm of the NCC identified separately due to the nature of the asymmetric colliding species. The rejection factors are shown in tabular form in Table 3.14. These results are based on simulations of 5000 d+Au events.

E_T Threshold (GeV)	8x8EM	8x8
1.0	2	1.6
2.0	5	2.0
3.0	15	3.5
4.0	40	5.7
5.0	99	10.0
6.0	233	17
7.0	505	30
8.0	1032	49
9.0	2083	77
10.0	3808	116
12.5	16910	295
15.0	49900	636
17.5	125000	1230
20.0	-	2300
25.0	-	5500

Table 3.3: Anticipated NCC LL1 rejection factors of minimum bias proton-proton collisions at $\sqrt{s} = 500$GeV for the 8x8EM and 8x8 trigger tiles.

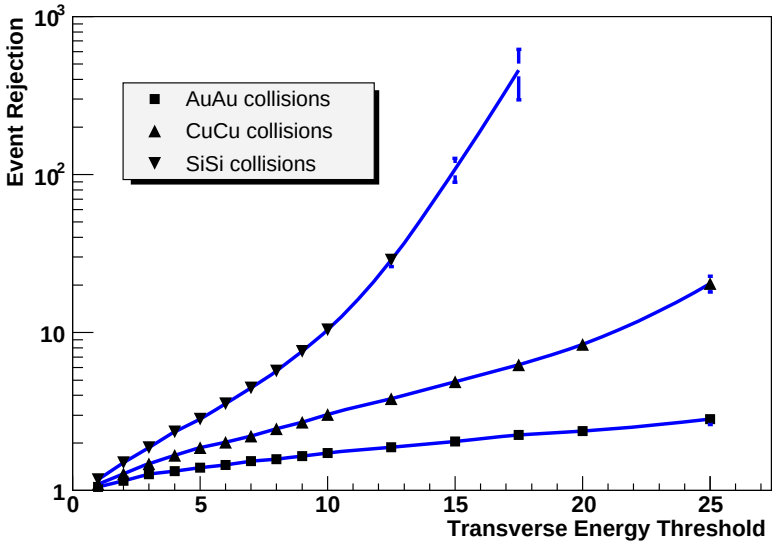

Figure 3.32: Anticipated NCC LL1 rejection factors of minimum bias heavy ion collisions at $\sqrt{s} = 200$GeV for the 8x8EM trigger tile, as described in the text.

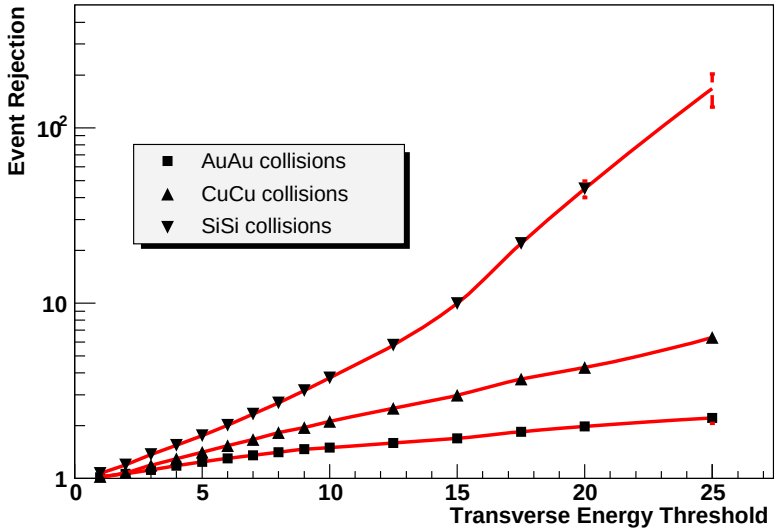

Figure 3.33: Anticipated NCC LL1 rejection factors of minimum bias heavy ion collisions at $\sqrt{s} = 200$GeV for the 8x8 trigger tile, as described in the text.

	Si+Si		Cu+Cu		Au+Au	
E_T Threshold (GeV)	8x8EM	8x8	8x8EM	8x8	8x8EM	8x8
1.0	1.2	1.1	1.1	1.0	1.1	1.0
2.0	1.5	1.2	1.3	1.1	1.2	1.1
3.0	1.9	1.4	1.5	1.2	1.3	1.1
4.0	2.4	1.5	1.7	1.3	1.3	1.2
5.0	2.8	1.8	1.9	1.4	1.4	1.2
6.0	3.5	2.0	2.0	1.5	1.5	1.3
7.0	4.5	2.3	2.2	1.7	1.5	1.4
8.0	5.7	2.7	2.5	1.8	1.6	1.4
9.0	7.6	3.2	2.7	2.0	1.7	1.5
10.0	10.4	3.7	3.0	2.1	1.7	1.5
12.5	29	5.8	3.8	2.5	1.9	1.6
15.0	108	10	4.9	3.0	2.0	1.7
17.5	459	22	6.3	3.7	2.3	1.8
20.0	1225	45	8.4	4.3	2.4	2.0
25.0	-	167	20	6.4	2.8	2.2

Table 3.4: Anticipated NCC LL1 rejection factors of minimum bias heavy ion collisions at $\sqrt{s} = 200$GeV for the 8x8EM and 8x8 trigger tiles.

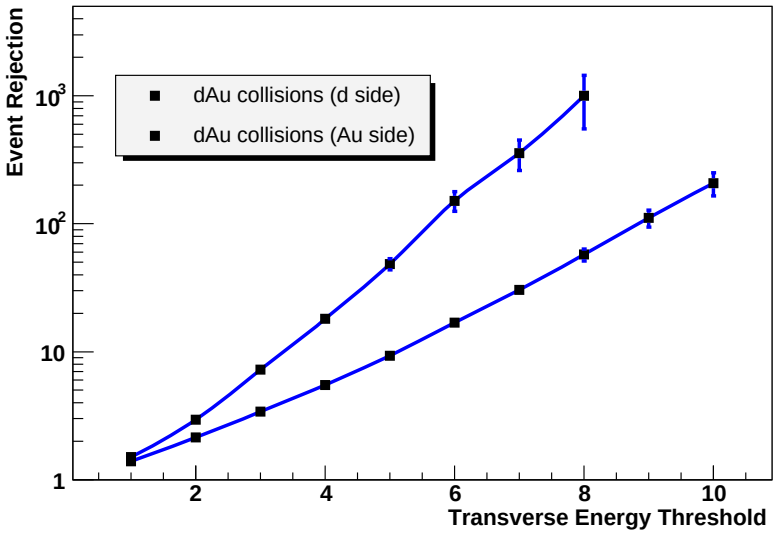

Figure 3.34: Anticipated NCC LL1 rejection factors of minimum bias d+Au collisions at $\sqrt{s}$ = 200GeV for the 8x8EM trigger tile, as described in the text. Note that the trigger rejections depend on whether the NCC arm in in the d-going or Au-going side of PHENIX.

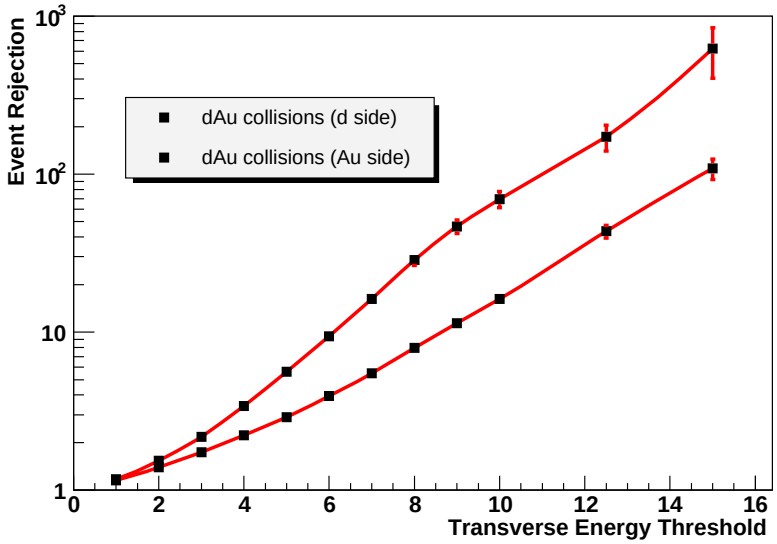

Figure 3.35: Anticipated NCC LL1 rejection factors of minimum bias d+Au collisions at $\sqrt{s}$ = 200GeV for the 8x8 trigger tile, as described in the text.Note that the trigger rejections depend on whether the NCC arm in in the d-going or Au-going side of PHENIX.

	d side		Au side	
E_T Threshold (GeV)	8x8EM	8x8	8x8EM	8x8
1.0	1.5	1.2	1.4	1.2
2.0	2.9	1.5	2.1	1.4
3.0	7.2	2.1	3.4	1.7
4.0	18	3.4	5.5	2.2
5.0	48	5.6	9.3	2.9
6.0	151	9.4	17	3.9
7.0	357	16	30	5.5
8.0	1000	29	57	7.9
9.0	-	47	111	11.4
10.0	-	69	208	16.2
12.5	-	172	1666	43
15.0	-	625	-	109

Table 3.5: Anticipated NCC LL1 rejection factors of minimum bias d+Au collisions at $\sqrt{s} = 200$GeV for the 8x8EM and 8x8 trigger tiles.

3.15 The NCC Research and Development Program

With the help of institutional contributions it was possible to maintain a small, but well focused, effort over the past two years to explore technologies for silicon detectors suitable for the PHENIX NCC. For about $100K the BNL, RIKEN, MSU, JINR, UCR groups were able to design, manufacture, and test batches of DC-coupled pad-structured Si sensors, AC-coupled pad-structured sensors and first ever samples of StriPixel sensors with effective strip width of 0.5 mm. Their were enough DC coupled sensors for the proof-of-principle prototype calorimeter which was completed and beam-tested in November 2005. The main results of completed R&D program are published in [IEEE, Breckenridge, QM].

3.15.1 Silicon Sensor Development

Test pad-structured DC coupled silicon sensors optimized for radiation hardness following the prescriptions listed in earlier sections were produced at the ELMA, subsidiary of the Research Institute of Material Science and Technology (RIMST) in Moscow, and delivered to Moscow State University for testing. The actual sensor picture together with the guard-ring structure are shown in Fig. 3.36. The 5kW, 300 μm thick FZ- wafers from Wacker (Germany) available at MSU were used for this submission. In total 30 sensors were produced, IV and CV measurements at MSU resulted in 25 sensors accepted and 5 sensors rejected (large leakage currents). Results of the depletion voltage (CV) and leakage current (IV) measurements are shown in Fig. 3.37.

We are very pleased with an outcome of this work, with both satisfactory yield and performance. Good sensors were used to build a NCC prototype recently tested in the test beam in Protvino, Russia (IHEP). The design of the test sensors was largely influenced by

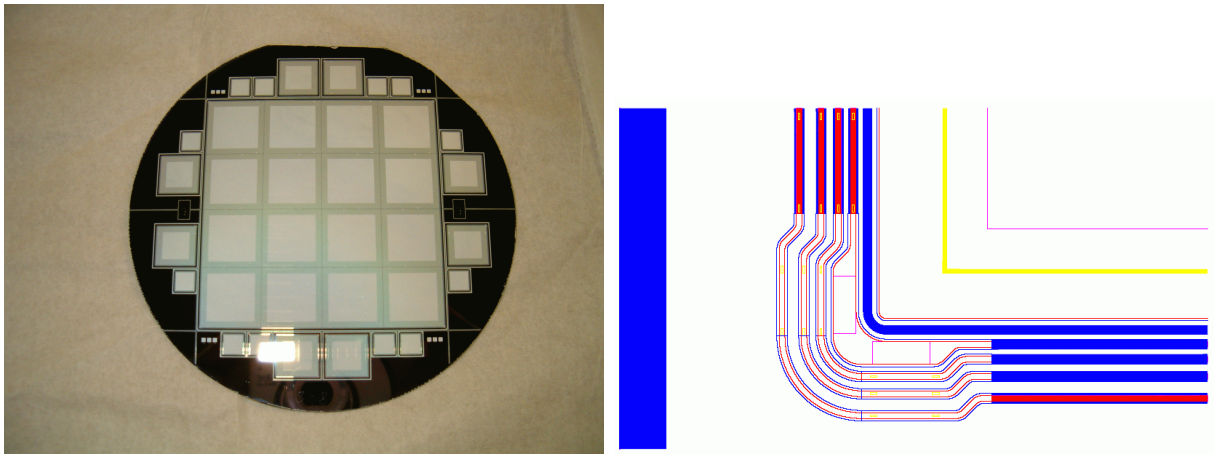

Figure 3.36: (left) NCC Silicon sensor with undiced wafer. The active area is subdivided into 16 readout pads 1.5x1.5 cm2 each. (right) Structure of the guard rings. The complexity of the design is needed to prevent voltage breakdowns after radiation exposure.

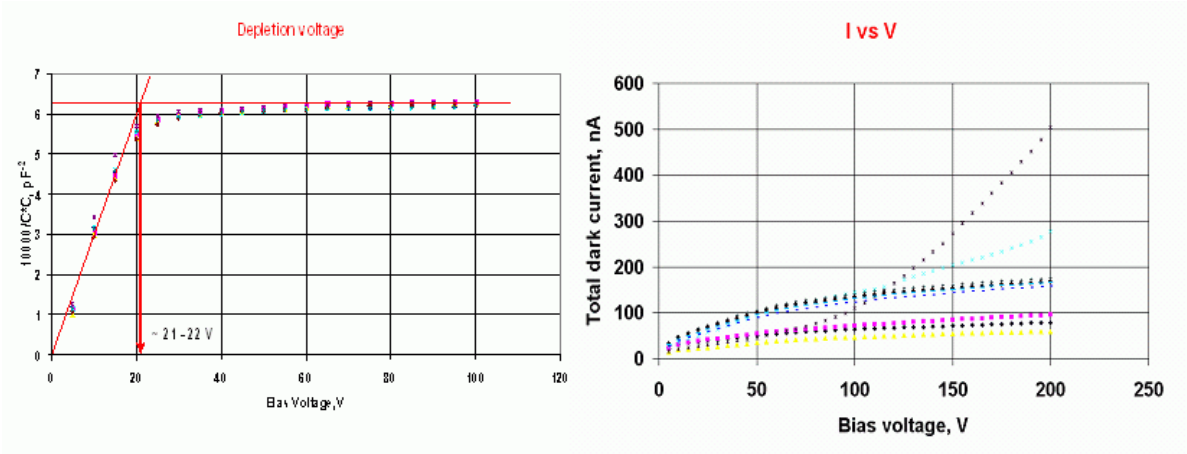

Figure 3.37: CV and IV measurement data for the test batch of 30 PHENIX NCC pad-structured sensors produced at ELMA in Russia.

preexisting experience at MSU with pad-structured sensors for the CALICE W-Si calorimeter prototype. In parallel we considered a number of options varying between two extremes illustrated in Fig. 3.38 with decoupling RC networks on and off sensors.

Sensors with built-in RC networks are probably the only option for detectors planning to digitize signals from individual pixels. Unfortunately this technology routinely results in increased cost and reduced yield associated with extra steps required to grow large capacitances on pad surfaces. In the case of the PHENIX NCC where individual pixels are ganged together to allow a single preamplifier to handle analog sum of the pixel currents, the advantages of AC coupled design are not obvious and may result in ineffective spending of resources. Our project was recently reviewed by an unofficial panel of Si detector experts at the SiDet Laboratory at FNAL. A recommendation was made to either use DSC coupled

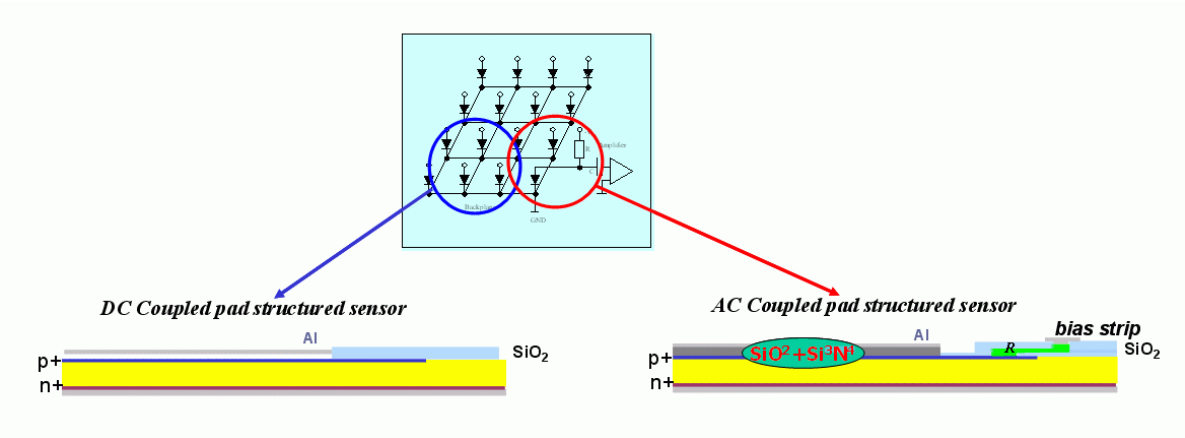

Figure 3.38: Two extreme designs for the pad-structured Si sensors. DC on the left and AC on the right.

sensors or to limit the upgrades to growing polysilicon resistors on the sensors keeping external decoupling capacitances. While no firm commitment was made, the modified design was proposed for considerations by ELMA, ON Semiconductors (Czech Republic) and SENS (Korea) companies. ON Semiconductors is expected to deliver test samples to our Collaborators in Prague shortly so for evaluation. The very first AC coupled sensors manufactured at ELMA were received at MSU while this CDR was in preparation and are now being tested.

Within the same framework we began development work aimed to optimize the stripixel sensor design. Critical aspects of charge sharing and crosstalk between crossing strips are very difficult to simulate, and the final choice cannot be made without prototyping a variety of structures. A prototype wafer was recently delivered from ELMA in Russia. Measurements on test structures have shown no problems with sensor production, however the sensors themselves happened to be shortened because of mismatch between the design files (made at BNL) and the technology used at ELMA. New revisions of the design is now submitted for preapproval by ELMA and production will follow. More details related to the R&D work on StriPixel detector layers and StriPixel's readout could be found in the addendum.

3.16 Test Beam Study of the Prototype NCC Calorimeter

The prototype NCC was designed as a proof-of-principle device for the Collaboration to acquire the experience in silicon detector production, and to test at least one possible assembly scheme and the robustness of technology. The prototype calorimeter was designed of 22 sampling layers, with the first 16 cells in groups of 6 and 10. These were designed as the as electromagnetic segments (2.5 mm W + 2.5 mm readout). The last 6 cells (15 mm W and 2.5 mm readout) serving as a hadronic segment. The calorimeter was built to allow installation up to 4 sensors per layer (12x12 cm^2). We used one position in every layer to install prototype DC coupled sensors. Fig. 3.39 is the photograph of a single assembled ROU

(readout unit) connected to the preamplifier board.

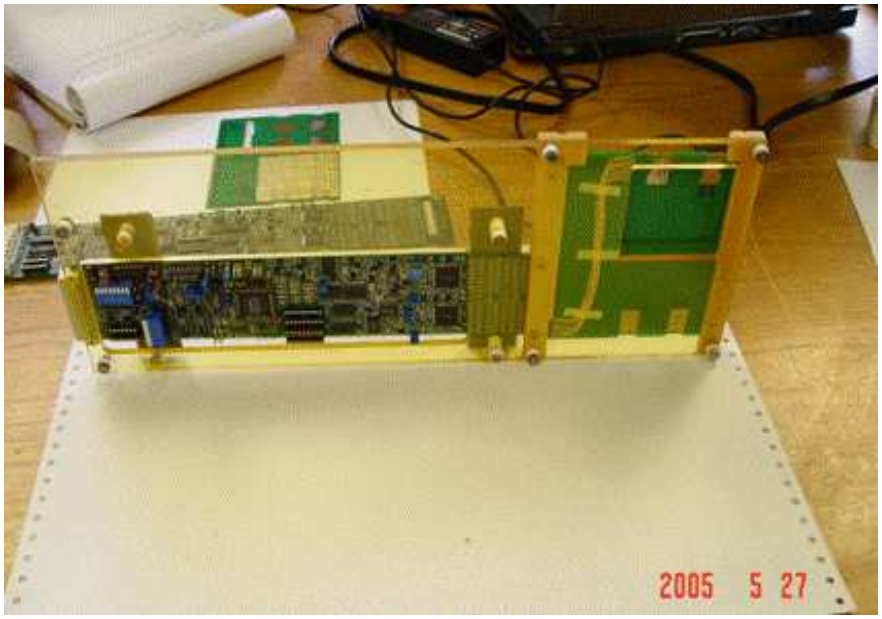

Figure 3.39: Single assembled readout layer for the prototype NCC connected to readout electronics.

For the test beam experiment we used preamplifier boards developed at MSU and equipped with CR1P4 16 channels preamplifier chips provided by A.Vacchi (Trieste, Italy). To make an optimal use of available electronics the number of geometrically matching pads from individual layers ganged together was limited to 4. Ganged and amplified signals (6 in total) were digitized using off-the-shelf multi-channel ADC unit. The assembled prototype is shown in Fig. 3.40.

Fully assembled prototype was structured into 4 electromagnetic segments and 2 hadronic segments. The prototype calorimeter was exposed to the electron and proton beams from IHEP U70 proton synchrotron in Protvino (Russia) in November 2005. In what follows we present data accumulated exposing the calorimeter to 70 GeV/c protons and 10 GeV/c positrons.

3.17 Data analysis

The amplitude distributions recorded in proton runs were used to establish values of the pedestals, the shape of the signal, minimum ionizing peak values and the signal/background ratio. The result is illustrated in Fig. 3.41 which shows the pedestal and MIP signal. The signal/noise ratio is 4-5 with a good MIP resolution.

In the case of the electron data the individual pedestals computed using data from proton run were subtracted to get signal amplitudes in every segment. MIP peaks varied segment-to-segment but was nearly independent of hit position in the plane. The recorded data are strongly affected by a common mode noise. Pads outside the base matrix of 3x3 towers

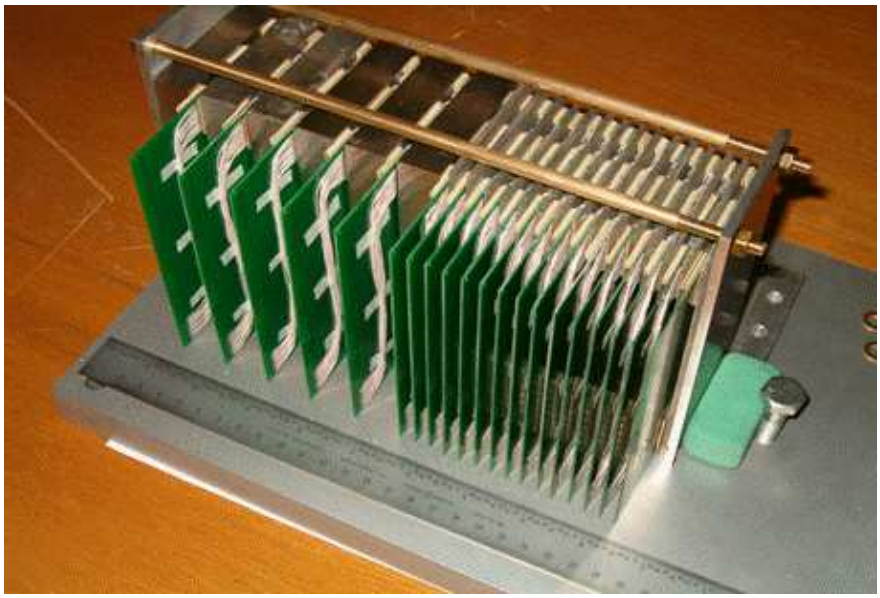

Figure 3.40: Assembled prototype calorimeter. Readout electronics not shown.

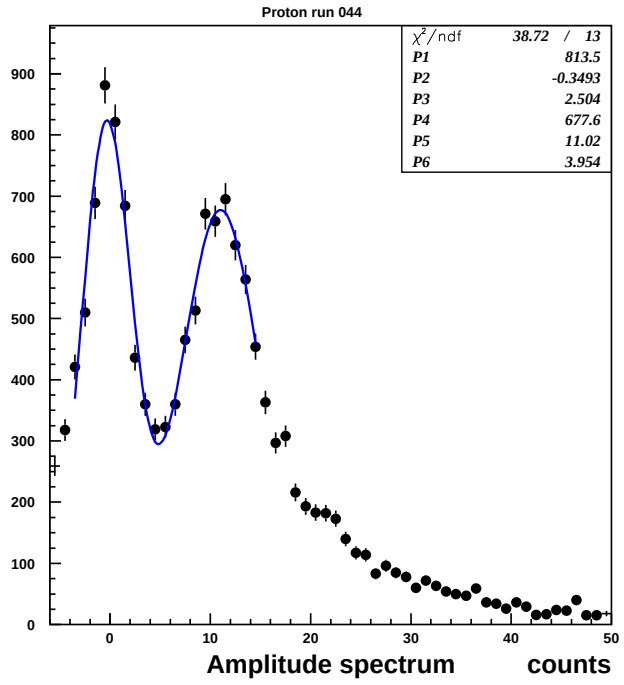

Figure 3.41: Amplitude distribution of the signal from the pad near beam impact.

centered at the tower with maximum amplitude were used to measure the common mode noise value which was subtracted from all 16 measured amplitudes prior to normalization. In addition the following cuts were applied to clean the data of hadronic contamination present in the electron beam:

- Amplitude sum in segment 1 was required to be smaller then amplitude sum in segment 2 (to exclude tails of showers started upstream of the prototype detector),.
- The amplitude sum in segment 1 was required to be smaller then 600 cnts (to exclude events with multiple hits).

. A typical event in the prototype calorimeter exposed to positrons of 10 GeV/c momenta cleaned of common mode noise is shown in Fig. 3.42.

Average energy in the segment when exposed to positrons is plotted as function of the calorimeter depth at the geometrical center of the segment in Fig. 3.43.

The observed behavior is consistent with the expected electromagnetic shower shape. The maximum in the distribution of deposited energy is reached at a depth of $\sim 7\ X_0$ in the calorimeter.

The mean longitudinal profile was fitted with the functional form $k \times X_0^{(a-1)} \times \exp -bt$ which describes the data with good accuracy.

In order to improve the experimental resolution an additional weighting procedure based upon measured longitudinal shower shape was applied to positron data. The final distribution of the weighted amplitude sum with is shown in Fig. 3.44. The data were fitted by sum of the Gaussian peak and polynomial background resulting in measured resolution of 11% (90% CL) for the 10 GeV/c positron beam consistent with predictions in earlier chapters of this CDR i.e. $\sim \frac{18\%}{\sqrt{(E)}} + 4\%$.

The positron data recorded in every segment of the prototype were further used to study the dependence of position resolution measured in individual segments on the depth position of the segment in calorimeter. In the absence of beam tracking resolution was computed subtracting measured coordinates from those computed using straight line fit to all six measured points (see Fig. 3.45).

As expected the best result ($\sigma = 1.4mm$) at 10 GeV is reached using data from segment next to shower maximum. Combining all 6 points we may estimate the pointing resolution of prototype calorimeter (Fig. 3.46)

A value ∼6 mrad was measured in X- and Y- planes what corresponds to pointing resolution $\sim 9mrad$ corresponding to 5mm resolution in impact parameter with respect to collision vertex.

The pointing capability is a byproduct of longitudinal segmentation introduced as an only tool available to forward physics in PHENIX to remove hadronic contamination from the photon sample. While probably non critical, this nice feature may be important in reducing contamination from non-beam sources like cosmic rays which are important source of background to photons with very high momenta.

In conclusion we would like to emphasize the following: the construction of of the prototype and exposure in the particle beam was probably the most important achievement of a longer then a year R&D effort. It proved

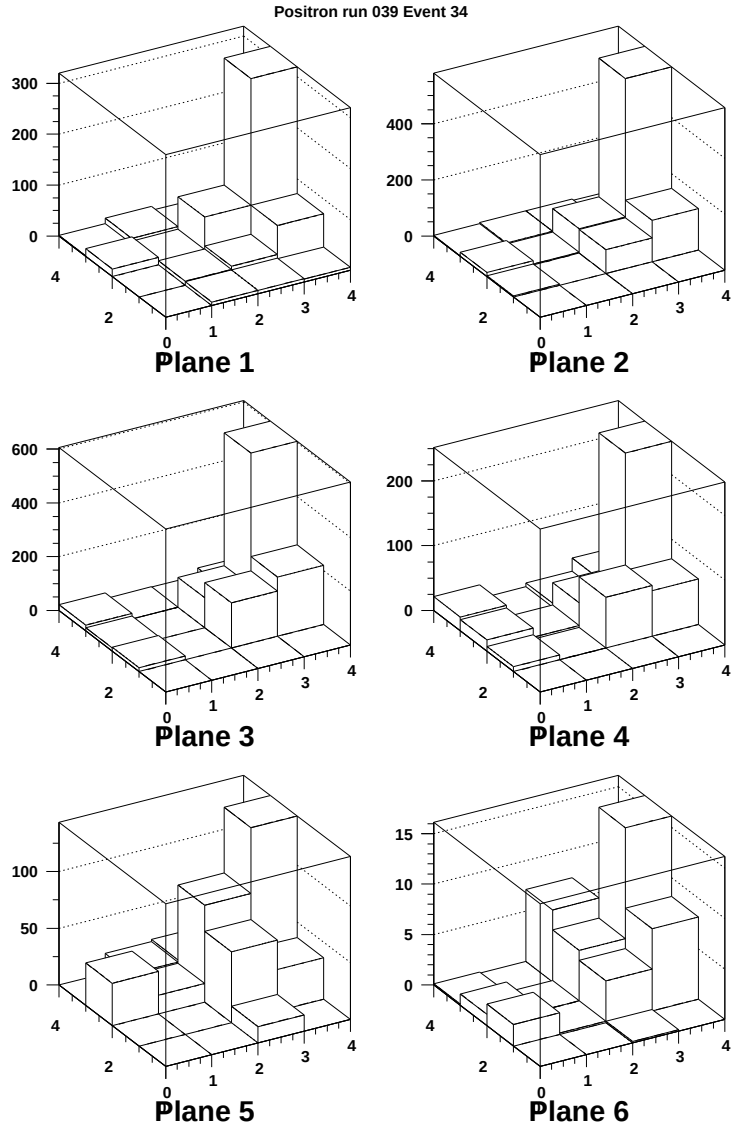

Figure 3.42: Example of the electromagnetic shower in prototype W-Si calorimeter

- the robustness of technology,
- the soundness of the idea to passively sum signals from multiple Si pads,
- the ability to handle and calibrate data from longitudinally segmented calorimeter,
- the ability of simulation to correctly predict detector performance,
- the ability of a collaboration which has a very brief prehistory and is composed of institutions from all over the world to coordinate its efforts and reach the desired goals.

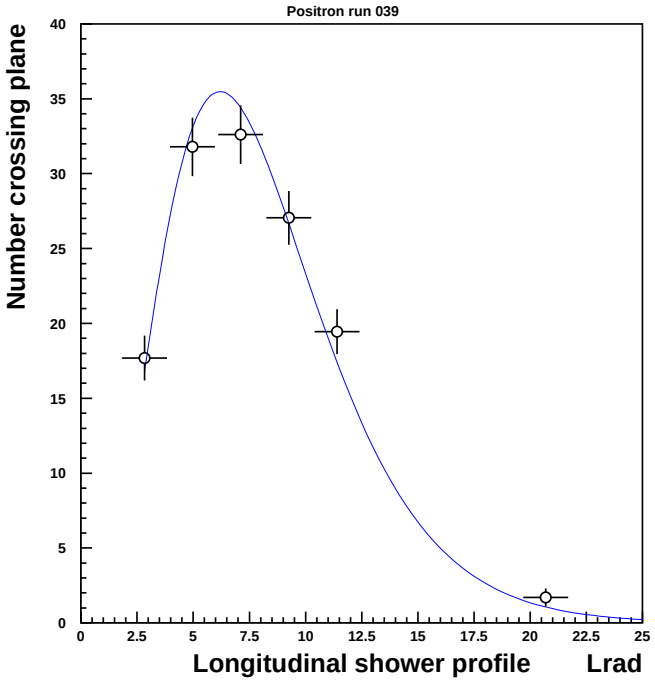

Figure 3.43: Longitudinal profile of electromagnetic shower.

3.17.1 Ongoing R&D Program

More recently the R&D effort has shifted towards finalizing technology choices as required by the construction project. We will closely follow the development of the digital signal processing plan for a near term PHENIX upgrade - the Hadron-Blind Detector which is functionally identical to what is proposed for the NCC and SVX4 based readout currently under development for the two outer layers of the PHENIX central Silicon Vertex Detector.

The key issues still to be resolved are the noise (capacitive and pick-up) in the detector operating with ganged sequential pads and optimization of the stripixel sensor design. The solution to the noise issue requires extremely careful design with large care taken in grounding the detector components and readout electronics. We have enlisted help from the D0 silicon laboratory at FNAL for the next step in the detector design and will rely on their expertise in large silicon systems and detector mechanics.

We will continue stripixel sensor development in parallel with helping NUCLON experiment based at MSU to implement single sided strip detectors of a similar geometry which we consider a backup solution. We plan to make the final technology choice in 2006.

For many parts of the NCC, the technology choices have been made, and the R&D is focusing on prototyping the designs. We will need to pursue and complete these topics over the next two years to start EDIA and construction of the NCC in FY08. The next stage R&D project will include:

- Comparative study of pad-structured DC coupled sensors implemented on $300\mu m$ and

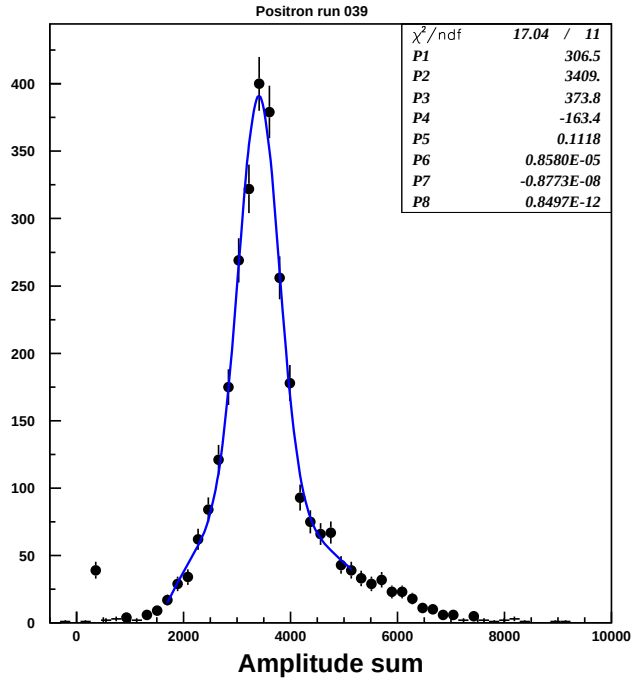

Figure 3.44: Energy distribution in the NCC prototype measured exposing detector to 10 GeV/c positron beam.

$500\mu m$ Si wafers,

- Comparative study of pad-structured DC coupled and AC coupled sensors including study of the effects related to implementing polysilicon bias resistors on sensors,
- Production and testing of StxriPixel test structures to study the influence of inter-pixel pitch on the charge sharing and crosstalk between strips,
- Finalizing design for the stripixel sensors,
- Finalizing design of the readout units for both kind of sensors,
- Designing and testing the heat removal scheme for on the sensor SVX4 based readout electronics in StriPixel layers,
- Finalizing conversion of ATLAS preamps for PHENIX NCC application. Implementing a new version of amplifier with 2-sided hybrid technology,
- Generating the layout for the preamplifier summer boards,
- Development of the digital readout for NCC,

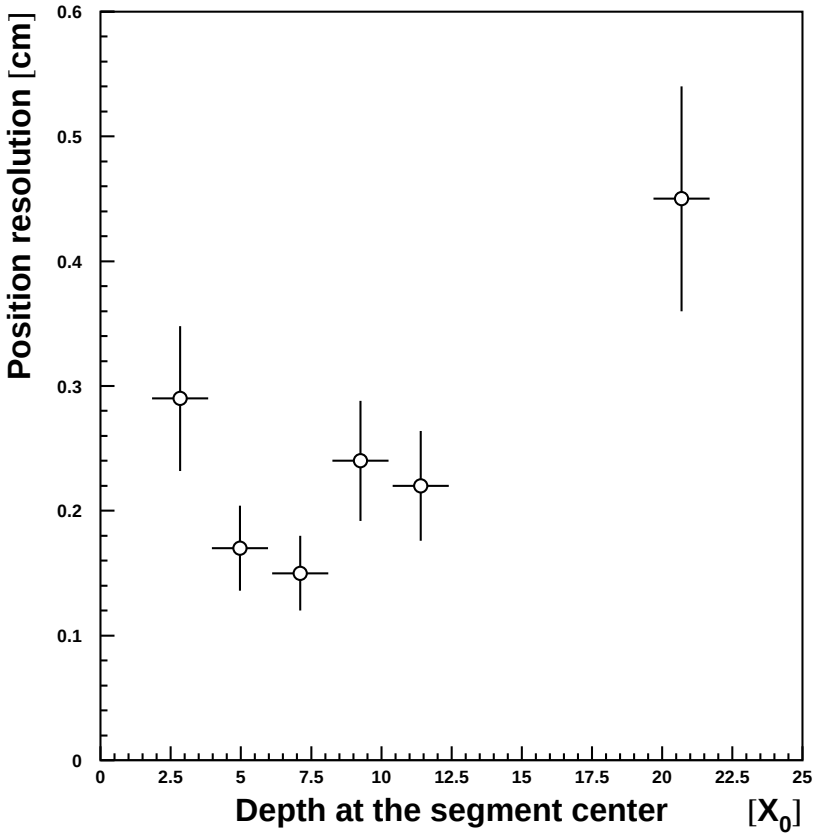

Figure 3.45: Precision of the impact point measurements in the segments of prototype detector. Location of the segment geometrical center in the prototype is plotted along X in units of X_0.

- Small scale production runs of pad-structured and StriPixel sensors to equip a fullscale brick-sized NCC prototype for on-the-bench and test beam measurements of the detector performance,
- Finalizing detector mechanical design,
- Constructing a full system prototype (single brick) and running test beam experiment-likely at FNAL in 2007.

The complete program will require total funds of about $US 400 000 uniformly distributed over the period of 2 years (2006/2007). These funds will be used to support the R&D work, procure the measurement equipment, pay for the work at foundries, mechanical workshops, PC-board production and stuffing and assembling fullscale calorimeter readout units.

It will end with presenting the final calorimeter design supported by performance measurements in the test beam to the Final NCC Design Review now scheduled for the fall of

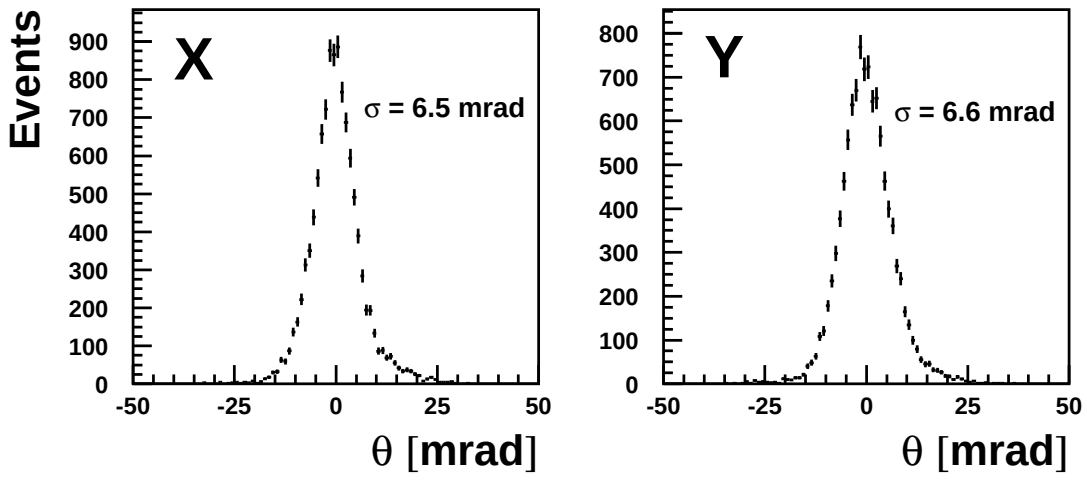

Figure 3.46: Pointing resolution measured in the prototype calorimeter exposed to 10 GeV/c positrons. Both X- and Y- planes are shown.

2007.

Chapter 4

Project Management and Responsibilities

The organization and management of the proposed effort is embedded in the management structure of the PHENIX experiment, which is part of the BNL RHIC project. The new organization must satisfy a number of requirements including a clear interface to the existing RHIC and PHENIX management structure, clear roles and responsibilities within the existing PHENIX subsystem structure. Particular attention has to be paid to the fact that a significant portion of the project efforts is carried by PHENIX groups which belong to the international component of PHENIX collaboration. Clear deliverables, responsibilities for deliverables and the accountabilities of the participating Institutions have to be defined. These responsibilities will be formalized in memoranda of understanding (MOU's) between PHENIX and the participating Institutions. In this section, we outline our proposed management organization and delineate responsibilities within the project.

4.1 Project Background

The proposed project is part of a detailed upgrades program to enhance the physics capabilities of PHENIX. The development of the PHENIX upgrade program started in response to the recent NSAC long-range plan, which was developed in 2000. The PHENIX Upgrade program spans the next 8 years. Realizing this plan will enable PHENIX to remain competitive well beyond the turn on of LHC expected for 2008, as well as advance our understanding of QCD by fully exploiting the unique spin physics capabilities of RHIC. The plan covers a broad range of measurements in A+A, p(d)+A, and p+p and its goal is to provide key measurements which currently can either not be addressed at RHIC or only with limited accuracy.

The calorimeter component of the PHENIX upgrade program was first proposed in the fall of 2004 when a Letter of Intent (LOI) for an upgrade of the forward region of PHENIX was written and presented to the PHENIX management. This LOI included the NCC, and a trigger for the muon spectrometer which is now being funded by the NSF. The forward LOI was reviewed at a joint meeting of the PHENIX detector council (DC) and executive

council (EC). Following their recommendations PHENIX management (PM) endorsed both projects and the group was charged with preparing NCC proposal for presentation to the DOE through BNL.

The NCC project was reviewed in December 2004 by a panel, including PHENIX Detector Council and Executive Council members as well as external members who are not PHENIX collaborators. The recommendations of the review panel have been very helpful to prepare the present proposal. All recommendations have been addressed and answers have been incorporated into the proposals.

4.2 The Management Plan for the NCC

4.2.1 PHENIX Management Structure

The NCC project is part of the PHENIX project and as such integrated into the PHENIX management structure as described by the PHENIX bylaws. The PHENIX Detector Council (DC) will advise PHENIX management on the design, construction, and integration of the NCC. The DC is co-chaired by the operations manager (Edward O'Brien) and the upgrades manager (Axel Drees). The NCC subsystem manager will serve as a member of the DC.

4.2.2 PHENIX Subsystem Leadership

We expect that the proposed NCC project will be funded through the DOE Office of Nuclear Physics (DOE-NP) beginning in 2008. The collaborating institutions will jointly fund remaining R&D efforts (2006-2007) resulting in construction and beam-testing of a W-Si prototype calorimeter serving as NCC system prototype. A successful completion of the NCC will require close collaboration between participating institutions, well-defined matrix of responsibilities and contributions in terms of deliverables. These deliverables and planned sources of contributions are outlined below. Within PHENIX, the responsibility for the NCC subsystem will be shared by the subsystem leader, Richard Seto (UCR) and his two deputies, Itaru Nakagava (RIKEN) and Edouard Kistenev (BNL). The subsystem leader reports to PHENIX PM and will represent the NCC in the PHENIX DC.

Simultaneously, E.Kistenev will serve as the DOE contract project manager (CPM), and will have the fiscal and construction responsibility for the DOE funded deliverables as outlined in this proposal. This involves appropriate planning, budgeting, and reporting.

4.2.3 Role of BNL

Because we expect that all DOE funding for this effort will be directed through the BNL Physics Department, BNL line management will have ultimate fiscal and managerial responsibility for the construction of the NCC and for its subsequent operation.

Fig. 4.1 shows a management chart of the NCC project. The subsystem manager has general responsibility for the implementation of the project and is assisted by two deputies, who are responsible respectively for the hardware and software aspects of the project. Similar

to other upgrade projects in PHENIX, the PHENIX operations manager will assist the project in all integration matters and is responsible for installation of the detector into the PHENIX experiment and for the safety of operations. The institutions that will participate in the implementation and management of individual tasks are given in the bottom right corner of every task block in Fig. 4.1. When our international collaborators, notably Russia, Czech, and Korea, are represented by several institutions working together they are indicated by nation, rather than by individual institution. PHENIX safety, DAQ, and infrastructure are common to all subsystems, so they are not listed as an explicit part of NCC management.

4.2.4 Specification of Deliverables

The NCC is divided into subprojects, which themselves are divided into tasks detailed in an NCC Microsoft Project File. The main tasks identified as blocks in Fig. 4.1 are closely related to deliverables, which need to be completed before the NCC construction project can be considered complete. Below are the major deliverables and responsible institutions and a brief review of institutional responsibilities.

4.2.4.1 Calorimeter

- Silicon pad-structured sensors designed and implemented to the specification: **MSU/Czech/Korea**
- Silicon strip sensors designed and implemented to the specification: **MSU/JINR/BNL**
- Readout units for the pad-structured calorimeter layers: **MSU**
- Readout units for PS and SM detectors: BNL/JINR
- Analog data processing electronics for pad-structured layers (EM1/EM2/HAD segments of NCC): **BNL**
- Detector-end data processing for StriPixel PreShowerand ShowerMax layers: **BNL/JINR**
- Digital data processing: **BNL/Nevis**
- Trigger electronics: **ISU/Ames**
- Support structure and absorber plates: **BNL/UCR**
- Calorimeter mechanical components: **JINR**
- Assembly and testing of calorimeter bricks: **BNL/UCR/RIKEN**
- Assembly and testing of calorimeter: **BNL/UCR/RIKEN**

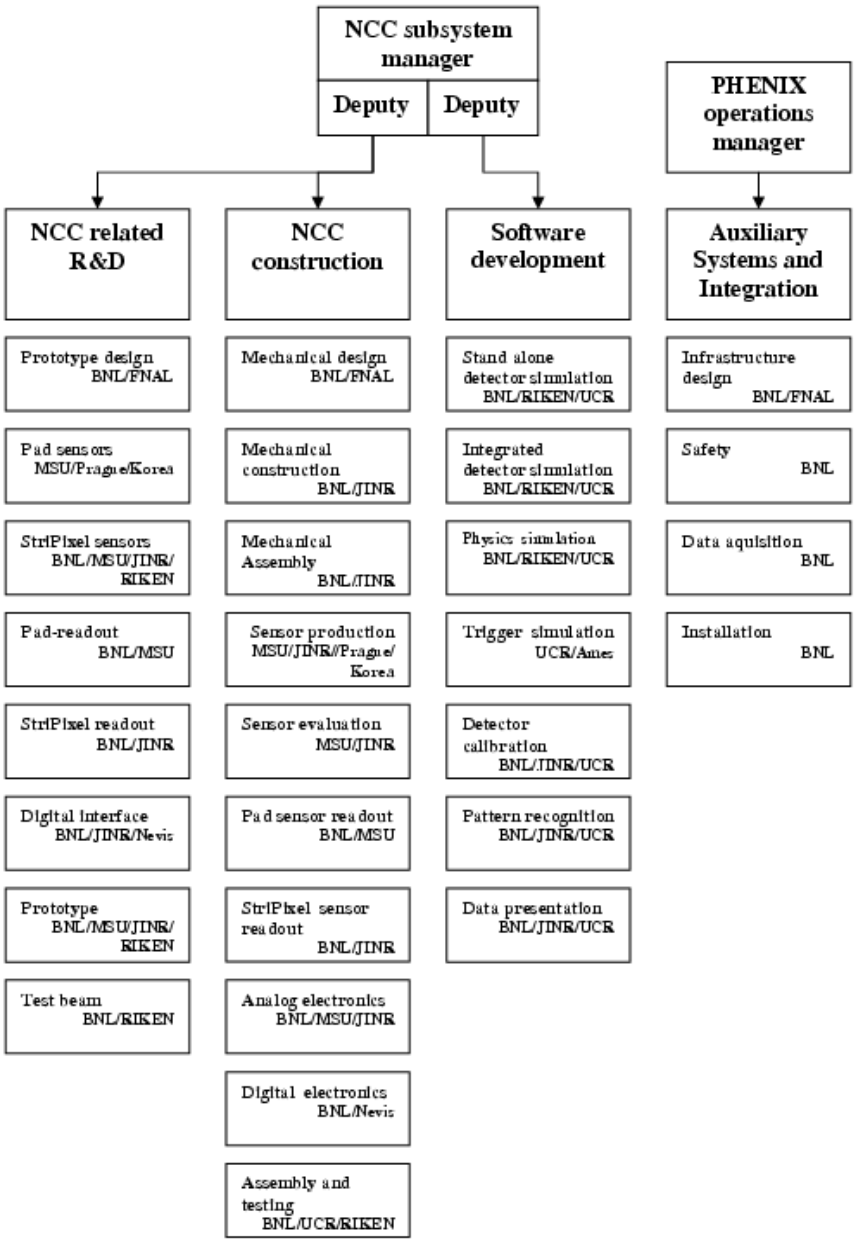

Figure 4.1: Management chart of the NCC project. The institutions participating in each task are shown.

4.2.4.2 DAQ System

- Data collection modules for calorimeters and position detectors (PS and SM): **BNL**
- Software development for data collection, monitoring and analysis: **BNL/UCR/RIKEN**

4.2.4.3 Auxiliary Systems and Integration

- System support requirements specified, including heat loads, power distribution, mechanical tolerances and grounding scheme: **BNL/UCR/FNAL**
- Ancillary systems operational, including power distribution and cooling system: **BNL**
- Installation and integration:**BNL**
- Commissioning of full detector system: **BNL/UCR/RIKEN**

4.3 Institutional Involvement

4.3.1 U.S. Based Institutions

Currently 20 institutions with over 70 individuals are involved in the NCC project. The different institutions bring in diverse research backgrounds, physics interests and expertise, which form a broad base to carry out the proposed project. Each group assumes specific responsibilities and will participate actively in the NCC project. According to their expertise and interests these groups will be involved in construction, installation, commissioning, operation, and data analysis. Formal commitments of the involved institutions will be specified in Memoranda of Understanding (MoU). Many of these groups have been already been actively involved in the R&D effort through institutional contributions, while others have joined the project only recently. Below are brief descriptions of expertise and potential involvement of the institutions.

University of California at Riverside and has made major contributions to R&D related to this proposal and will specify their specific responsibilities in the future. The BNL Instrumentation Division, Fermi National Laboratory and EWHA University in Japan join the NCC project because of their interest in the technological development, but are not members of the PHENIX collaboration.

The PHENIX group at University of California, Riverside has taken primary responsibility for Simulations and Software development, and is heavily involved with ongoing NCC related R&D. As the subsystem manager, UCR group leader Richard Seto has played a leading role in the management of the NCC, and was instrumental in bringing the project to the proposal stage.

The PHENIX Group from the BNL Physics Department provides infrastructure and technical support as part of Systems Engineering and Integration (SE&I) for the entire PHENIX experiment. It has a staff of mechanical and electrical engineers and a group of

experienced technicians who are intimately familiar with the detector, and work closely with the BNL Collider-Accelerator Department for operations and any modifications to its present design. They designed much of the infrastructure for the baseline detector, including racks, cable trays, electrical power, cooling, access, safety systems and numerous other services, and carried out the installation of all of the present subsystem detectors. This group will now be closely involved with the design of the infrastructure and support for the PHENIX Forward Calorimeters, and with its installation into PHENIX.

The BNL physics group is joined by physicists associated with Physics Department and Chemistry Department (former PHOBOS experiment). The two groups bring management and physics experience and broad experience with silicon detector technology. Individual group members bring specific technical skills that will be important for the successful construction, installation, commissioning and operation of a silicon detector in the RHIC environment. Edouard Kistenev of BNL will serve as the DOE contract project manager (CPM). He has taken a leading role in developing the concept and design of the NCC project.

BNL's Instrumentation Division's Silicon Detector Development and Processing Laboratory (SDDPL) will be involved in the development of silicon strip detectors for PHENIX Upgrades. The activity will include detector simulation, design, and processing of prototype detectors. SDDPL will also be involved in laser scan tests of those prototypes, these tests will be carried out in close collaboration with the BNL Physics Department and RIKEN. BNL Instrumentation Department proposed the solution based upon hybrid amplifiers earlier developed for ATLAS experiment at CERN to serve as a basis for the analog signal processing for NCC. The further activities will involve modification to the schematics for the amplifiers to work with positive polarity signals, compactification of the layout, testing and participation in production.

PHENIX group from Iowa State University (group leader John Lajoie) will take responsibility for the design, implementation, construction, and support of the NCC Level-1 trigger system (similar to their earlier work on the design, construction and maintenance of the PHENIX Level-1 trigger system).

The BNL PHENIX group has primary responsibility for a number of major subsystems. These include Electronics Facilities and Infrastructure (EF&I), Online Computing Systems (ONCS) and Offline Computing. These groups will participate in the electronic integration and readout of the NCC detector into the PHENIX data acquisition system, and will be involved with track reconstruction and offline data analysis.

The BNL PHENIX group will also serve a host institution for the project and will provide the lab space for the final detector assembly and testing.

4.3.2 International Participation

The Moscow State University group has internationally recognized expertise in silicon detectors and their application in experimental physics. MSU contributed to the ZEUS experiment at DESY (silicon hadron rejector), the D0 experiment at FNAL (central tracker), and a number of smaller projects. Together with JINR, RIKEN, BNL and UCR the MSU group built and tested a "proof-of-principle" NCC prototype, which demonstrated robustness of

the technology. MSU will bare the major responsibility for production and evaluation of pad-structured sensors for the calorimeter, the design and testing of StriPixel sensors, development, and the production and testing of all pad-structured readout layers.

The Joint Institute for Nuclear Research in Dubna has a variety of expertise in all aspects of experimentation in Nuclear and particle physics. The JINR PHENIX group can draw on expertise of their local and international collaborators in mechanics, electronics and sensor development. The group has already contributed to the initial design of NCC mechanical structure, will continue this work in collaboration with group from FNAL, and will take major responsibility for production of major mechanical components for NCC. Together with BNL Chemistry Department the JINR group works on data collection design for StriPixel detectors and is planning to assume major responsibility for assembling StriPixel layers.

The Korean groups at Yonsei University and Ewha University have become involved in the work on Silicon pad-structured sensors. Ewha has built the Silicon detector for the CREAM balloon project working together with industrial partners SENS Technology - a small company specializing in Silicon detectors. The group is currently working on prototyping the NCC pad detectors on 8" wafers - a major development since this would significantly reduce the cost.

The Czech Republic group involves physicists from the Institute of Physics, Charles University and the Czech Technical University, who are primarily interested in the PHENIX spin physics program and silicon detector development. The Czech group has a history of collaboration with groups from JINR, Dubna and an established relationship with the major silicon processing plant in the Czech Republic (ON Semiconductors). As part of their contribution to NCC project, Prague collaborators have already initiated the first round of sensor prototyping at ON Semiconductors, this development will allow to better estimate potential benefits of sensor production in Czech republic and to coordinate the sharing of silicon production efforts between MSU, Korea, and ON Semiconductors.

4.4 Acknowledgements

We thank our PHENIX collaborators for the support and encouragement of the proposed NCC upgrade and for fruitful discussions. We acknowledge R&D and participant funding support from the Department of Energy, Office of Science, Office of Nuclear Physics, the National Science Foundation, and the Research Foundation of SUNY (U.S.), Ministry of Education, Culture, Sports, Science, and Technology and the Japan Society for the Promotion of Science (Japan), Ministry of Education, Youth and Sports (Czech Republic), Korea Research Foundation, Center for High Energy Physics, and Korea Science and Engineering Foundation (Korea), and Ministry of Education and Science, Rassia Academy of Sciences, Federal Agency of Atomic Energy (Russia).

Chapter 5

Budgets and Schedule

5.1 Overview

The PHENIX Forward Calorimetry Upgrade Project naturally splits into three subprojects namely:

- W-Si Calorimetry R&D to culminate in construction of a W-Si calorimeter system prototype in 2007;
- Construction and installation of DOE funded NCC staring in 2008 and ready for physics in the fall of 2010;
- Construction and installation of a second NCC starting in 2009 and ready for physics in 2011.

The project is based on a cost sharing between the DOE Office of Nuclear Physics and the PHENIX NCC Group, as introduced in this Proposal. The group is jointly responsible for funding the ongoing W-Si Calorimetry R&D program, which is planned for completion in 2007 with construction and beam testing of the Calorimeter System Prototype. The DOE Construction funding is expected to start in 2008 and continue for three years with peak funding in 2009.

The PHENIX NCC Group is planning to collect among its members other then US enough funds (R&D and Construction) to cover the cost of the second PHENIX NCC unit.

In what follows we discuss cost and scheduling issues related to the DOE Construction Project to allow implementing the proposed upgrade in the minimal configuration consisting of a single calorimeter unit. The decision to deploy this unit as an upgrade to North or South muon arms will depend on RHIC running schedule and configurations for collisions of different ion species.

The cost and schedule for the NCC Upgrade project has been developed using engineering estimates, vendor quotes and experience from the construction of silicon detectors from participating Institutions. The two subprojects (First and Second NCC) are not totally independent, and unless extra production capacity is identified the starting date for the

Second Calorimeter Project will be constrained by the rate of production of Si sensors at the ELMA (Russia) and ON Semiconductors (Czech Republic) facilities. While the estimated base costs of the North and South detectors are identical, the real cost to the PHENIX NCC Group can be different depending on accounting practices specific to collaborating countries. In this section, we outline only those costs which concern the DOE.

5.2 Contingency Analysis

In order to estimate the necessary contingency we have taken the following approach:

- For all tasks that require the production of prototypes, contingency is taken to be 100% of the cost of one extra design plus prototype cycle.
- For all testing, assembly, and installation tasks, we assume that the contingency is 50% of the costs.
- For purchases based on vendor information, 20% of the cost is included as contingency.
- For all other purchases, the contingency is 30% of the costs.

5.3 Overhead Estimate

The overhead applied to funds requested from the DOE we assume an 18% rate which is the current practice for capital construction projects at BNL. This 18% overhead is included into "Cost to Project" in our budget tables. The additional overheads charged by local institution is not listed separately. However, these costs are included in the budget table via cost estimates for item ordered in foreign countries through collaborating institutions. In particular, all manpower costs are fully burdened costs, including overhead.

5.4 Tungsten-Si Calorimeter R&D

The ongoing collaboration funded R&D efforts is aimed at confirming design ideas developed in he course of earlier 2005 R&D and at constructing and testing a full scale brick-wide prototype of the W-Si calorimeter including the SM and PS layers. When this portion of the project is completed the Collaboration will be in possession of

- the final design and production documentation for DC-coupled pad-structured Si sensors developed to NCC specifications;
- the final design and production documentation for the pixilated strip Si sensors (StriPixels) developed to NCC specification;
- the final design and production documentation for the pad-structured readout units. The design documentation for readout unit components (carrier and interconnect boards) will be ready for submission to pc-board production house;

- the final design and production documentation for the pixilated strip readout units including sensor-end hybrids, brick-end receiver boards and front-end modules interfacing the NCC to PHENIX DAQ;

- a full size prototype of W-Si calorimeter brick assembled and tested in a test beam.

The completion of this the R&D program is a major mile stone and is necessary to address the challenges of this Upgrade Project. It is important for the collaboration to accumulate test beam data using detector in all essential aspects identical to one the Collaboration proposes to build. Exposing this detector to high energy particle test beam will confirm performance expectations, and provide the experience and test-data necessary for successful use in the PHENIX experiment.

This R&D program will be supported by the Collaboration with major funding provided by BNL (BNL Generic R&D funds) and other collaborating institutions in US and Japan, and in-kind and man-power contribution from other collaborating Institutions. Most of the funding required to carry this program in 2006 is already committed. Fig. 5.1 below lists the major costs associated with R&D project.

R&D 2006-2007: Development	2006(k$)	2007(k$)	Total(k$)
Pxilated strip sensors (StriPixels)	26,300		26,300
Pad-structured readout units	18,565		18,565
Strip-structured readout units	5,000	12,000	20,000
Pad readout analog elecronics		15,200	15,200
Pad readout digital electronics	3,000	5,813	8,813
StriPixel readout electronics	4,000	8,250	12,250
R&D 2006-2007: Design and Prototyping			
Si wafers		39,950	39,950
Pad-structured sensors	70,000	22,531	92,531
Pad-structured ROU's	5,000	19,323	24,323
Electronics for pad-structured layers	10,000	27,500	44,063
Pixilated strip sensors (StriPixels)		10,540	10,540
StriPixel ROU's and electronics		18,185	21,121
Mechanical Structure	5,000	8,850	15,863
Testing (bench and Test beam)		17,038	17,038
2006-2007 funding request	**146,865**	**205,179**	**366,554**

Figure 5.1: Major Costs associated with research and development related to PHENIX NCC Project.

5.5 NCC Construction

The total cost of the Nose Cone Calorimeter Construction Project to DOE including contingencies and overhead is **3.94 million $US**. This number is detailed in the table below where the base cost estimates (including spares), contingency requests and overheads are first quoted separately. We have also separated the costs directly related to construction of a single NCC unit and those for ancillary systems (PHENIX DAQ, infrastructural and installation costs).

The funding from the DOE will cover

-the construction of a single Calorimeter unit comprising two fine electromagnetic and one coarse hadronic pad-structured segments, PreShower and ShowerMax detectors in 2008-2010;

- an upgrade to the PHENIX infrastructure to allow for installation of this detector in 2010;

- installation and commissioning of a single Nose Cone Calorimeter in 2010.

Costs (k$) / Year:	2008	2009	2010	Base Cost	Contin-gency	Over-head	Total
NCC Construction (k$)	900	1800	1007	2331	827	549	3707
Ancillary Systems (k$)			236	160	48	28	236
Total DOE Construction (k$)	900	1800	1243	2491	875	577	3943

Figure 5.2: Profile of DOE cost estimates for first NCC.

As indicated in Fig. 5.2, the first NCC unit is planed to be ready for physics for the RHIC run that begins in the fall of 2010. Below are the budgetary and scheduling details.

The major cost item and the critical item in the project are silicon sensors. The two kinds of sensors used in the calorimeter are responsible for nearly half of the unit cost. The other half is spread relatively uniformly among mechanics and electronics. The production of sensors drives the schedule. At this time we have identified three suppliers, Russia(ELMA), Czech Republic (ON Semiconductors) and in Korea (SENS), interested in producing Si sensors following our design. ELMA and ON Semiconductors both have an experience with production of sensors close to NCC specifications, hence cost estimates and schedules presented in this proposal are based upon quotations from ELMA. It will take two years to produce sensors for a single NCC unit if all production is done at ELMA. To shorten this time down to the 18 months reserved for this task in our schedule we will have production running both at ELMA and ON Semiconductors.

A Korean option is also being investigated. The major issue is availability of large size wafers (8"), which are prerequisites for keeping the production price in Korea competitive to that in Russia and Czech Republic.

In 2008 funding is required to purchase silicon wafers, start sensor production and to set assembly areas at collaborating institutions. Funding in 2009 covers all major purchases including tungsten plates and electronics components (US Industry), most of the Si (foundries

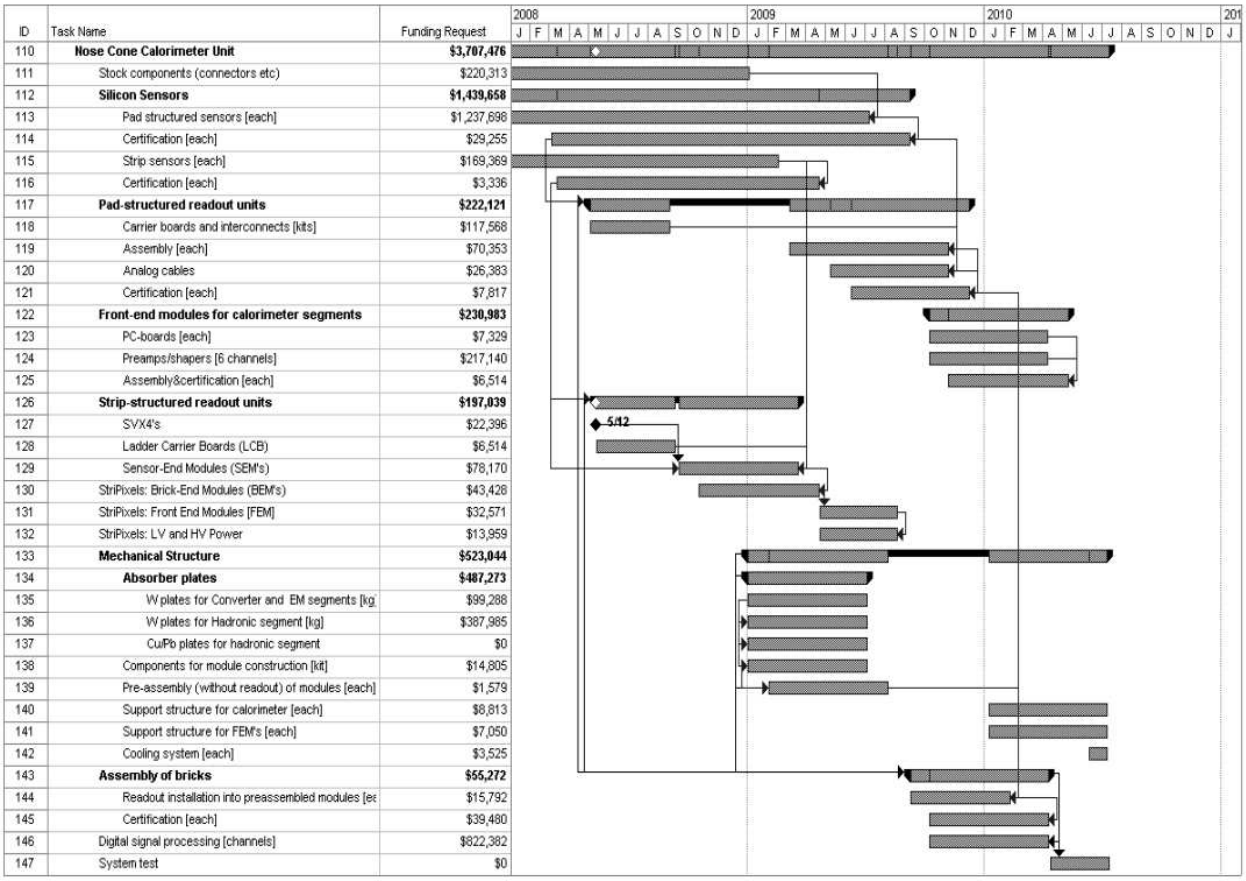

ID	Task Name	Funding Request
110	**Nose Cone Calorimeter Unit**	**$3,707,476**
111	Stock components (connectors etc)	$220,313
112	**Silicon Sensors**	**$1,439,658**
113	Pad structured sensors [each]	$1,237,698
114	Certification [each]	$29,255
115	Strip sensors [each]	$169,369
116	Certification [each]	$3,336
117	**Pad-structured readout units**	**$222,121**
118	Carrier boards and interconnects [kits]	$117,568
119	Assembly [each]	$70,353
120	Analog cables	$26,383
121	Certification [each]	$7,817
122	**Front-end modules for calorimeter segments**	**$230,983**
123	PC-boards [each]	$7,329
124	Preamps/shapers [6 channels]	$217,140
125	Assembly&certification [each]	$6,514
126	**Strip-structured readout units**	**$197,039**
127	SVX4's	$22,396
128	Ladder Carrier Boards (LCB)	$6,514
129	Sensor-End Modules (SEM's)	$78,170
130	StriPixels: Brick-End Modules (BEM's)	$43,428
131	StriPixels: Front End Modules [FEM]	$32,571
132	StriPixels: LV and HV Power	$13,959
133	**Mechanical Structure**	**$523,044**
134	**Absorber plates**	**$487,273**
135	W plates for Converter and EM segments [kg]	$99,288
136	W plates for Hadronic segment [kg]	$387,985
137	Cu/Pb plates for hadronic segment	$0
138	Components for module construction [kit]	$14,805
139	Pre-assembly (without readout) of modules [each]	$1,579
140	Support structure for calorimeter [each]	$8,813
141	Support structure for FEM's [each]	$7,050
142	Cooling system [each]	$3,525
143	**Assembly of bricks**	**$55,272**
144	Readout installation into preassembled modules [ea	$15,792
145	Certification [each]	$39,480
146	Digital signal processing [channels]	$822,382
147	System test	$0

Figure 5.3: Budgetary and scheduling details covering major tasks involved in construction of the first NCC unit (extracted from the project file).

in collaborating countries) and detector assembly (collaborating institutions). We are planning for the last task to be carried mainly in the students laboratories in collaborating Universities.

5.6 Additional NCC to Complement the DOE Construction project

As stated above, the PHENIX Collaboration is pursuing the design and construction of a complementary second PHENIX NCC to (a) avoid RHIC running time losses when running asymmetric collision species, (b) to double the yield of rare probes (thereby reducing RHIC running time), and (c) to access the production kinematics resulting in associated production of prompt leptons in forward-backward directions (for example, electrons from Z-decays).

While the details of how to finance the second NCC are not yet clear, its base cost is below 3 million $US and will be limited to production costs. Ancillary system costs are already covered in the first DOE funded stage of the Project. The PHENIX collaboration is actively

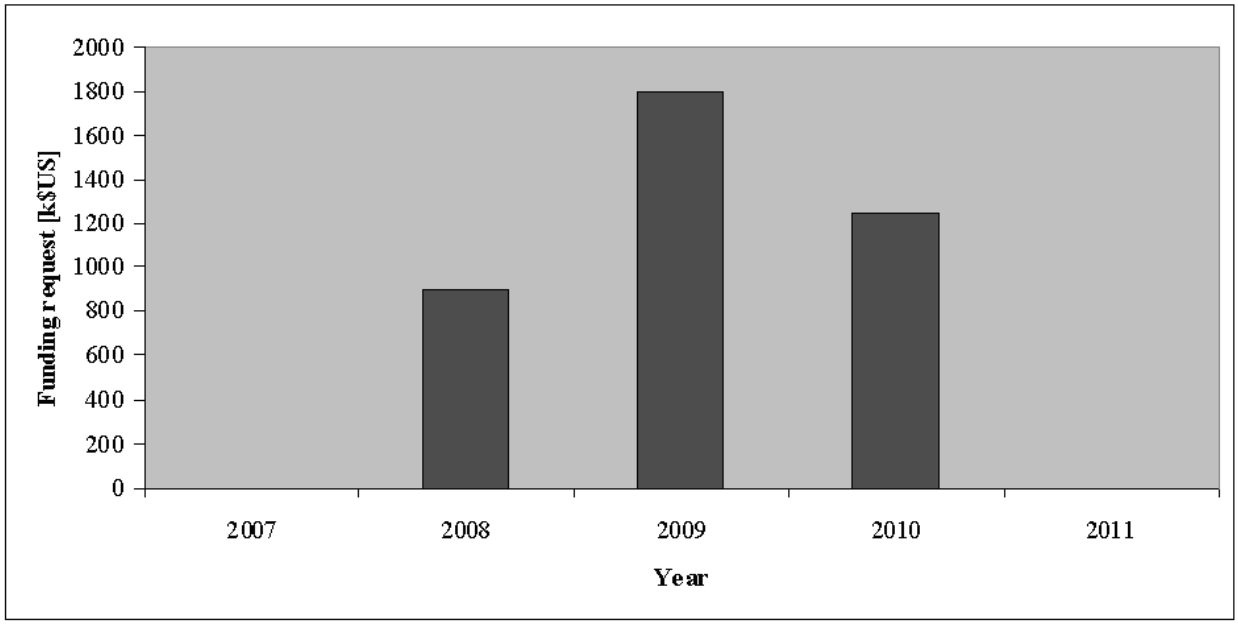

Figure 5.4: Proposed funding profile for DOE Construction project (also see first three columns in Fig. 5.3.

persuing now all possible venues for funding this part of the project through international contributions.

Appendix A

Event Rates

In this section we estimate the event rates of selected physics processes corresponding to some of the major goals of the NCC detector. All rates are for a single NCC. We start with expected luminosities for RHIC II from the BNL Collider Accelerator Division (CAD). We then assume a 50% duty factor for the RHIC machine, and a 60% up time for the PHENIX detector during a 12 week run to obtain an integrated luminosity (see table A.1).

There are several typical losses in efficiency from our experience in the first 5 years of data taking. These are listed in table A.2. The first arises from a vertex cut, which we take to be ± 20 cm from the nominal collision point. We assume 55% efficiency from losses due to the spread of the beam. Secondly, the minimum bias trigger uses the Beam-Beam Counters (BBC) located up and downstream of the collision point. In the high multiplicity environment of heavy ion collisions - this trigger is almost 100% efficient. However in low multiplicity p+p and p+A collisions, the efficiency drops since in some cases, no particles actually trigger the BBC. Finally we have taken 80% for the reconstruction efficiency, a reasonable number from our experience in the last several years.

Pythia was used to obtain p+p cross sections for direct photons, π^0's, W's, and the χ_c. To obtain heavy ion yields we assumed a point-like cross section - that is the cross sections were scaled by the product of the atomic weights of the incoming nuclei. For π^0's and the χ_c a suppression factor was assumed consistent with the data from Runs 1-5 or about a factor

Table A.1: Luminosity guidance from CAD for RHIC II. We assume a 50% duty cycle for RHIC to give a weekly integrated luminosity. We then assume a 12 week run and a 60% uptime for PHENIX to give an total integrated luminosity.

Species Collision E	p+p 200 GeV	500 GeV 500 GeV	p+Au 200 GeV	Cu+Cu 200 GeV	Au+Au 200 GeV
luminosity ($s^{-1}cm^{-2}$)	1×10^{32}	5×10^{32}	2.5×10^{29}	8×10^{28}	7×10^{27}
luminosity/week ($\text{pb}^{-1}\text{week}^{-1}$)	33	166	0.083	0.025	0.0025
Integrated Luminosity (pb^{-1})	238	1195	0.6	0.18	0.018

Table A.2: Efficiency factors added into the rate calculations. In the analysis we typically require that the vertex be within 20 cm of the nominal collision point, which results in a loss of 0.55. For A+A collisions the minimum bias trigger formed by the Beam-Beam counters are essentially 100% efficient, however in p+p and p+A collisions there is some loss.

Species	p+p 200 GeV	p+p 500 GeV	pAu	CuCu	Au+Au
vertex cut	0.55	0.55	0.55	0.55	0.55
min bias trigger efficiency	0.75	0.75	0.90	1.0	1.0
reconstruction efficiency	0.80	0.80	0.80	0.80	0.80
total efficiency factor	0.33	0.33	0.40	0.44	0.44

of 2 for minimum bias collisions. Tables A.3 and A.4 give the yields for a 12 week run for pp, pA, Cu+Cu and Au+Au collisions for a single NCC.

We are studying the effect of triggering as described in section 3.14. A simple 8x8 tile trigger should be sufficient for p+p and p+A collisions given a DAQ bandwidth of 8kHz. However, at present a simple 8x8 trigger will be ineffective in heavy ion collisions giving rejections of less than 2. Using a minimum bias trigger for heavy ion collisions results in substantial loss of a e.g. a factor of 6 in Au+Au collisions and 30 in Cu+Cu collisions. This does not affect the χ_c since this depends on a dimuon trigger and will not come from triggering using the NCC. The work on the trigger is in its very early stages and more sophisticated trigger schemes will be explored. In addition improvements are envisioned to the DAQ to increase its rate by a factor of 2 or more.

Table A.5 gives a summary of the physics program addressed by the Nosecone Calorimeter. Rates for direct photons and π^0's are typically about 5 times that which will be available in the central EMC in A+A collisions. Without the NCC the χ_c would be impossible. The rate into the central EMC is simply too small. The NCC, by contrast utilizes the large acceptance of the muon arms to detect the J/ψ, and is itself a large acceptance detector. For both p+p and p+A collisions, the crucial aspect of the NCC is the forward rapidity coverage which allows one to reach low x.

Table A.3: Yields in p+p collisions of various processes into the acceptance of a single NCC for a 12 week run.

Species	process		Yield
pp 200 GeV	π^0 production	$p_T(\pi^0) > 5$ GeV	62M
		$p_T(\pi^0) > 10$ GeV	260K
		$p_T(\pi^0) > 15$ GeV	8K
		$p_T(\pi^0) > 20$ GeV	450
pp 200 GeV	direct photon production	$p_T(\gamma) > 5$ GeV	1M
		$p_T(\gamma) > 10$ GeV	33K
		$p_T(\gamma) > 15$ GeV	2.6K
		$p_T(\gamma) > 20$ GeV	280
pp 200 GeV	W$\rightarrow e + \nu_e$	$p_T(e) > 5$ GeV	16
		$p_T(e) > 10$ GeV	11
		$p_T(e) > 20$ GeV	5
pp 200 GeV	$\chi_{c1} \rightarrow \gamma J/\psi \rightarrow \gamma\mu\mu$		26K
	$\chi_{c2} \rightarrow \gamma J/\psi \rightarrow \gamma\mu\mu$		42K
pp 500 GeV	π^0 production	$p_T(\pi^0) > 5$ GeV	1300M
		$p_T(\pi^0) > 10$ GeV	17M
		$p_T(\pi^0) > 15$ GeV	1.3M
		$p_T(\pi^0) > 20$ GeV	190K
pp 500 GeV	direct photon production	$p_T(\gamma) > 5$ GeV	24M
		$p_T(\gamma) > 10$ GeV	1.7M
		$p_T(\gamma) > 15$ GeV	270K
		$p_T(\gamma) > 20$ GeV	65K
pp 500 GeV	W$\rightarrow e + \nu_e$	$p_T(e) > 5$ GeV	4.9K
		$p_T(e) > 10$ GeV	4.4K
		$p_T(e) > 20$ GeV	2.8K
pp 500 GeV	$\chi_{c1} \rightarrow \gamma J/\psi \rightarrow \gamma\mu\mu$		790K
	$\chi_{c2} \rightarrow \gamma J/\psi \rightarrow \gamma\mu\mu$		1.1M

Table A.4: Yields in pAu, Cu+Cu and Au+Au collisions of various processes into the acceptance of a single NCC for a 12 week run.

Species	process		Yield
pAu 200 GeV	π^0 production	$p_T(\pi^0) > 5$ GeV	37M
		$p_T(\pi^0) > 10$ GeV	150K
		$p_T(\pi^0) > 15$ GeV	4.7K
		$p_T(\pi^0) > 20$ GeV	270
pAu 200 GeV	direct photon production	$p_T(\gamma) > 5$ GeV	610K
		$p_T(\gamma) > 10$ GeV	20K
		$p_T(\gamma) > 15$ GeV	1.5K
		$p_T(\gamma) > 20$ GeV	170
pAu 200 GeV	$\chi_{c1} \to \gamma J/\psi \to \gamma\mu\mu$		10K
	$\chi_{c2} \to \gamma J/\psi \to \gamma\mu\mu$		16K
CuCu 200 GeV	π^0 production	$p_T(\pi^0) > 5$ GeV	130M
suppressed		$p_T(\pi^0) > 10$ GeV	545K
		$p_T(\pi^0) > 15$ GeV	16K
		$p_T(\pi^0) > 20$ GeV	942
CuCu 200 GeV	direct photon production	$p_T(\gamma) > 5$ GeV	4.1M
		$p_T(\gamma) > 10$ GeV	130K
		$p_T(\gamma) > 15$ GeV	10K
		$p_T(\gamma) > 20$ GeV	1.1K
CuCu 200 GeV	$\chi_{c1} \to \gamma J/\psi \to \gamma\mu\mu$		40K
suppressed	$\chi_{c2} \to \gamma J/\psi \to \gamma\mu\mu$		65K
AuAu 200 GeV	π^0 production	$p_T(\pi^0) > 5$ GeV	100M
suppressed		$p_T(\pi^0) > 10$ GeV	440K
		$p_T(\pi^0) > 15$ GeV	13K
		$p_T(\pi^0) > 20$ GeV	1.1K
AuAu 200 GeV	direct photon production	$p_T(\gamma) > 5$ GeV	4M
		$p_T(\gamma) > 10$ GeV	130K
		$p_T(\gamma) > 15$ GeV	10K
		$p_T(\gamma) > 20$ GeV	1.1K
AuAu 200 GeV	$\chi_{c1} \to \gamma J/\psi \to \gamma\mu\mu$		43K
suppressed	$\chi_{c2} \to \gamma J/\psi \to \gamma\mu\mu$		70K

Table A.5: The coverage by the NCC of some of relevant kinematical variables given the rates mentioned previously.

Process	Species	Physics Goal	
π^0 production	pAu 200 GeV	saturation	$1< y <3$; p_T ~15 GeV
	p+p 200 GeV	"CGC"	$1< y <3$; p_T ~15 GeV
direct photon production	pAu 200 GeV	saturation	$1< y <3$; p_T ~15 GeV
	p+p 200 GeV	"CGC"	$1< y <3$; p_T ~15 GeV
π^0 production	Au+Au 200 GeV	parton energy loss	$1< y <3$; p_T ~15 GeV
Heavy Ions	Cu+Cu 200 GeV		$1< y <3$; p_T ~15 GeV
	pAu 200 GeV		$1< y <3$; p_T ~15 GeV
	p+p 200 GeV		$1< y <3$; p_T ~15 GeV
direct photon production	Au+Au 200 GeV	jet tomography	$1< y <3$; p_T ~15 GeV
"photon-jet"	Cu+Cu 200 GeV		$1< y <3$; p_T ~15 GeV
Heavy Ions	pAu 200 GeV		$1< y <3$; p_T ~15 GeV
	p+p 200 GeV		$1< y <3$; p_T ~15 GeV
$\chi_{c1} \rightarrow \gamma J/\psi \rightarrow \gamma\mu\mu$	Au+Au 200 GeV	confinement	$1< y <2$
Heavy Ions	Cu+Cu 200 GeV		$1< y <2.5$
	pAu 200 GeV		$1< y <3$
	p+p 500 GeV		$1< y <3$
π^0 production	p+p 200 GeV	$A_{LL}(p_T)$	
Spin	p+p 500 GeV		
direct photon production	p+p 200 GeV	$\Delta G(x)$at low x	$x \sim 3 \times 10^{-3}$
Spin	p+p 500 GeV		$x \sim 1 \times 10^{-3}$
W$\rightarrow e + \nu_e$ *Spin*	p+p 500 GeV	$\Delta\overline{q}$	
Spin			

Appendix B

Simulations

This appendix outlines the progress made in understanding the capabilities of the NCC in the study of a variety of physics topics. The physics analysis topics addressed by the NCC require:

- The measurement of π^0 spectrum to 30 GeV (15 GeV $p_\perp$) in AA, pA, and p+p collisions.
- The measurement of the direct photon spectrum in AA, p+A and p+p collisions, and correlations of direct photons and high momentum π^0's.
- the measurement of jets in p+p collisions for extraction of Bjorken x.
- the ability to use isolation cuts to identify direct photons and leptons from W bosons and heavy quarks in p+p and dAu events on an event-by-event basis.

In what follows, all plots assume the luminosities stated in Appendix A.

As mentioned previously, electromagnetic calorimetry in the central region ($-0.35 < y < 0.35$) has been a very powerful tool for the PHENIX detector. The purpose of the NCC is to extend these measurements to higher rapidity, and to increase the statistics for low event processes such as direct photon events. The increase in statistics can be rather large. RHIC II gives us a factor of 10 increase in luminosity while a single NCC will give us an increase in acceptance of about 5. Theoretically this leads to an increase in yield of a factor of 50. Practically however, the increase is somewhat less than this since the p_T spectrum drops off as a function of rapidity. As an example, the NCC will see about 3 times as many direct photons in AuAu collisions above a p_T of 5 GeV than the central EMC.

The increase in statistics is critical for many measurements. For example for correlation measurements in the case of photon-jet events in Au+Au collisions- we wish to divide the event sample into bins of transverse momentum and rapidity in order to be able to reconstruct the energy loss of partons as a function of momentum as well as the energy density of the collision.

For the signals we are interested in for heavy ion collisions, namely the χ_c, high momentum direct photons, and π_0's, we have tools we can use to isolate the signal. For the χ_c the

tool is the invariant mass difference $m_{\gamma\mu\mu} - m_{\mu\mu}$. For the direct photon measurements in Au+Au and dAu we will use the method of looking at the comparison of the γ to π^0 ratio measured vs expected, where we must make a very good measurement of the π^0 spectrum. This method was used to generate the direct photon signal shown in Fig. B.1. In p+p and p+A collisions, for event-by-event measurements of the direct photon to measure x_{BJ}, we will use higher momentum photons and isolation cuts. In what follows we assume RHIC II luminosities as shown in table A.1.

B.1 Direct Photons

The method used in this the PHENIX data analysis to extract the direct photon signal (Fig B.1) makes use of the fact, that we can measure the precise π^0 spectrum. We will use the same method in the NCC - this will be possible because the PS/SM detectors should give us a good identification of showers associated with π^0's as explained in section 3.4.4. Once a π^0 spectrum is measured, the direct photon analysis proceeds as follows: A simulation is used to calculate the expected γ to π^0 ratio using the measured π^0 spectrum, putting in all known sources except direct photons. In the simulation a ratio is made between the photon spectrum and the π^0 spectrum. The same is done in the data and a double ratio is made i.e.

$$R = \frac{(\gamma/\pi^0)_{measured}}{(\gamma/\pi^0)_{expected}} = \frac{(\frac{\gamma_{\pi^0}+\gamma_{direct}}{\pi^0})_{measured}}{(\frac{\gamma_{\pi^0}}{\pi^0})_{expected}} \sim 1 + \frac{\gamma_{direct}}{\gamma_{\pi^0}}$$

This method cancels many systematic errors. In particular overlapping showers will cancel in the ratio if the simulation is done correctly. Fig. B.1 shows the the statistical errors which will be reached in such an analysis in Au+Au collisions.

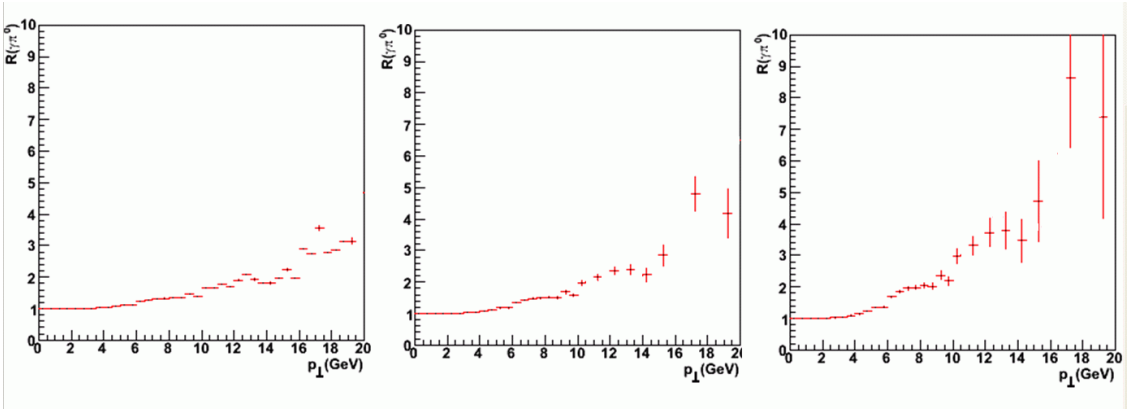

Figure B.1: Simulation of the direct photon signal, i.e. the ratio $R = \frac{(\gamma/\pi^0)_{measured}}{((\gamma/\pi^0)_{expected})}$ as measured by the NCC. R in p+p collisions[left] ; R in p+Au collisions[center]; R in Au+Au collisions [right]. Our final analysis will require a comparison of all three systems. Error bars are from the statistics we expect to get in the experiment. The fluctuations of the points arises from lack of statistics in the simulation.

In a single run at RHIC II luminosities the NCC should be able to make measurements of the direct photon spectrum to 15 in p_T at rapidities between 1 and 3 nicely complementing the results to be obtained at central rapidity.

The study of direct photons opposite a high momentum hadron allows for a study of a calibrated jet since the photon does not undergo any quenching. While the process is most easily visualized on an event by event basis, in practice it is done using correlation functions where the angular correlation between photons and high momentum π^0's are plotted. The combinatorial background is subtracted using a mixed event technique. Using the technique of recognizing showers which actually arise from the decay of π^0 described in section 3.4.4 a background sample of decay photons opposite high momentum π^0's can be constructed and subtracted from the original distribution to yield a correlation function of direct photons and hadrons. As was mentioned in 2.1 such studies can be done as a function of the reaction plane to enable a 3-D tomography of the system.

It is well known that isolation criteria can be used in p+p collisions to identify direct photons. Fig. B.2, left panel shows the yield of photons from decays in QCD events (blue) and direct photons (red) in 500 GeV p+p collisions. After requiring a separation criteria, $E_{cone}/E_{direct-photon} < 0.1$, where E_{cone} is the amount of electromagnetic energy in a cone of size $\Delta\eta\Delta\phi$=0.8, the direct photons dominate over decay photons above a p_T of 7 GeV. See fig. B.2 (right panel).

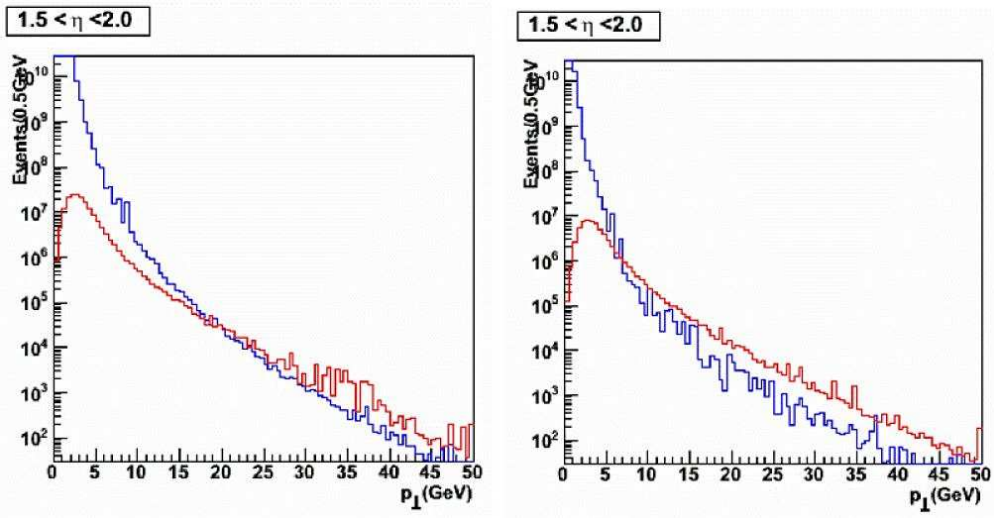

Figure B.2: Yield of photons between $1.5 < \eta < 2$ from decays in QCD events (blue) and direct photons (red) in 500 GeV p+p collisions [left]; Yield of photons between $1.5 < \eta < 2$ from decays in QCD events (blue) and direct photons (red) in 500 GeV p+p collisions after an isolation cut as explained in the text [right].

The method works in p+A collisions as well since the photon is generally separated from the bulk of the produced particles. Fig. B.3 shows the yield of photons from decays in QCD events (blue) and direct photons (red) in pAu collisions. Of course, one can also use a method similar to that used in heavy ion collisions and obtain the direct photon

spectrum on a statistical basis, which would then allow one to go to low p_T. An important point, mentioned previously is that in the case of suppression due to the initial state - i.e. the CGC, direct photons should should experience a similar suppression as the hadrons. Photons, which to first order, do not interact via the strong interaction, should not be sensitive to final state effects - i.e. nuclear matter or any sQGP and should be clean indication of suppression due to initial state effects.

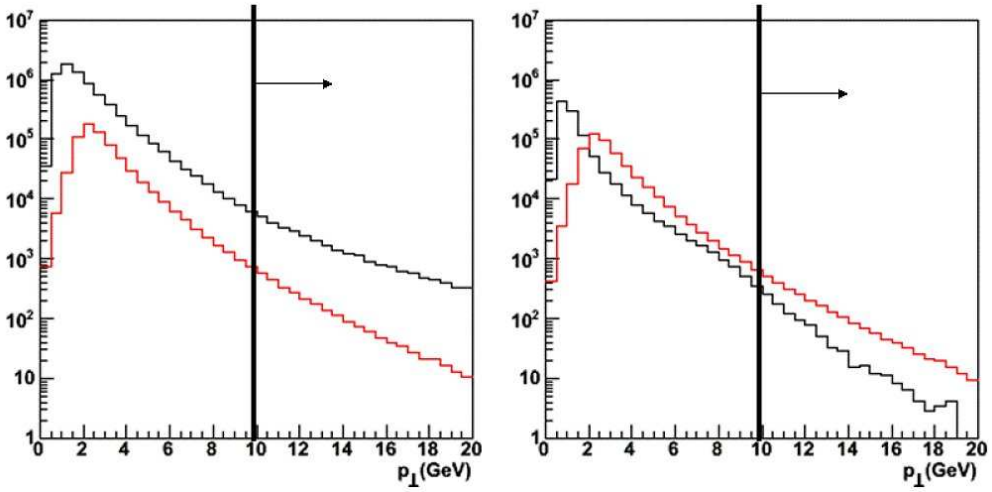

Figure B.3: (left) Photons from decays in QCD events [black] and direct photons [red] in pAu collisions between $1 < \eta < 3$. (right) For the QCD background, only the highest energy photon in each event is plotted. Photons between $1 < \eta < 3$ from decays in QCD events [black] and direct photons [red] in pAu collisions after an isolation cut in which $E_{cone}/E_{direct-photon} < 0.1$, where E_{cone} is the amount of electromagnetic energy in a cone of size $\Delta\eta\Delta\phi$=0.8. Unlike the other figures in this section, the simulation was done using a heavy ion event generator HIJING. For the generation of QCD background events a cut of 10 GeV was made on the hard scattering of partons, hence one should look at the region to the right of the line in these plots.

B.2 The χ_c

The χ_c decays into a J/ψ and a photon. We first identify the J/ψ via its di-muon decay - it may also be possible to use the di-electron channel as well. For χ_c's in which the muons are detected in the muon arms - the photon is accepted in the NCC more than 60% of the time(Fig. B.4). In order to see the χ_c one reconstructs the $\mu^+\mu^-\gamma$ invariant mass and subtracts off the $\mu^+\mu^-$ invariant mass where the dimuon mass is required to be in the J/ψ peak. The χ_c should show up as a peak at the χ_c-J/ψ mass difference of about 400-500 MeV. There are actually 2 χ_c states which decay with large branching ratios to the J/ψ with masses 3511 and 3556 MeV, however our resolution will now allow us to separate these two states. Note that the resolution is now primarily due to the resolution of the photon and not the resolution of the muon spectrometer.

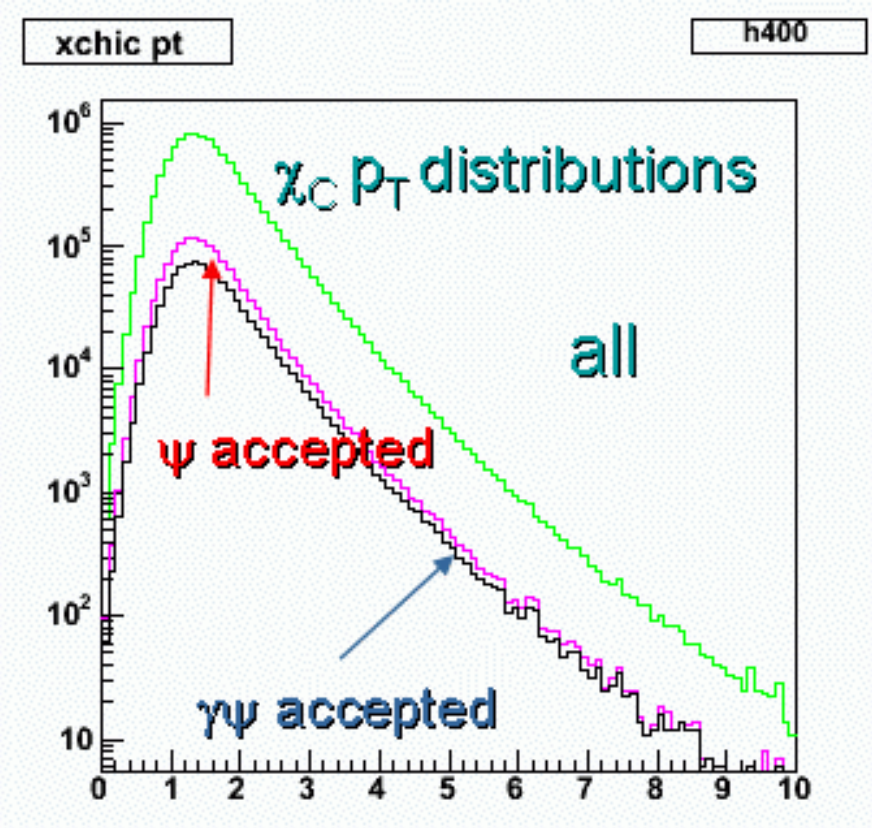

Figure B.4: p_T distributions for the χ_c. Green-all, red-J/ψ accepted in the muon spectrometer, blue-χ_c decay photon accepted in NCC and J/ψ accepted in the muon spectrometer.

A simulation was done in which single χ_c events were generated using PYTHIA which were overlaid on a background of photons corresponding to a variety of cases from p+p collisions to central Au+Au collisions. The S/B on the J/ψ was taken from present data, where we have assumed an improvement in resolution and background rejection of decay muons from the FVTX. In the case of central AuAu collisions this lead to a S/B of about 1/5. The J/ψ was then reconstructed and paired will all photons in the event to form a γJ/ψ invariant mass distribution. We assumed that the background could be subtracted using a mixed background technique.

As an example fig. B.5 shows the invariant mass difference for simulated full events in p+p collisions for rapidity between 2 and 2.5. The background distribution is shown in black with a subtracted spectrum shown on the right. The resolution is about 120 MeV. Note that the typical energy of the photons is about 1 GeV. The energy resolution for showers contained in in EM1 and EM2 is $0.03 + \frac{0.18}{\sqrt{(E)}}$. When higher energy showers greater than 10 GeV enter the HAD compartment however, the resolution becomes $0.03 + \frac{0.27}{\sqrt{(E)}}$. We believe that out estimate of the calorimeter resolution is reasonable. If however, the calorimeter resolution is much worse the χ_c can still be reconstructed, at least in p+p events. Fig. B.6 shows the

resolution if the resolution is degraded to $\frac{0.50}{\sqrt{(E)}}$.

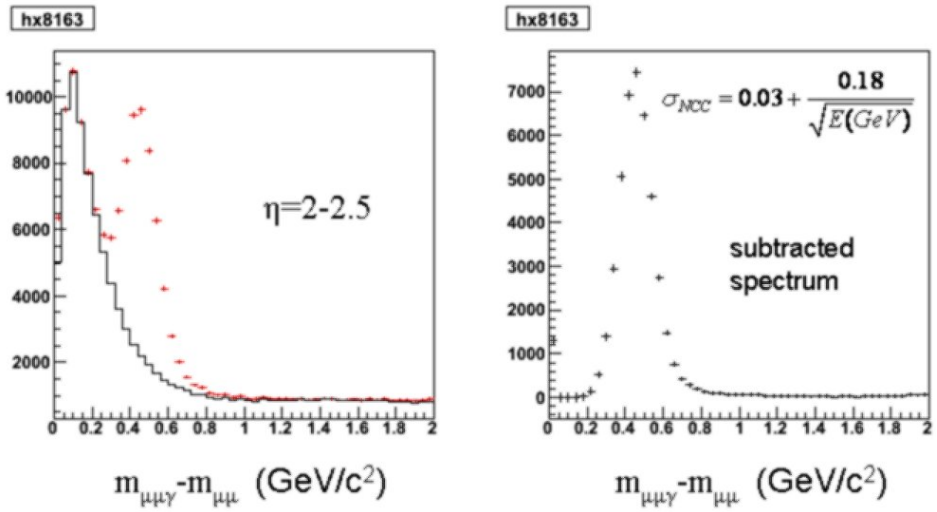

Figure B.5: The $M_{\gamma\mu\mu} - M_{\mu\mu}$ invariant mass distribution in p+p events. The left plot shows the raw mass difference spectrum (red) and background (black). The right shows the subtracted spectrum.

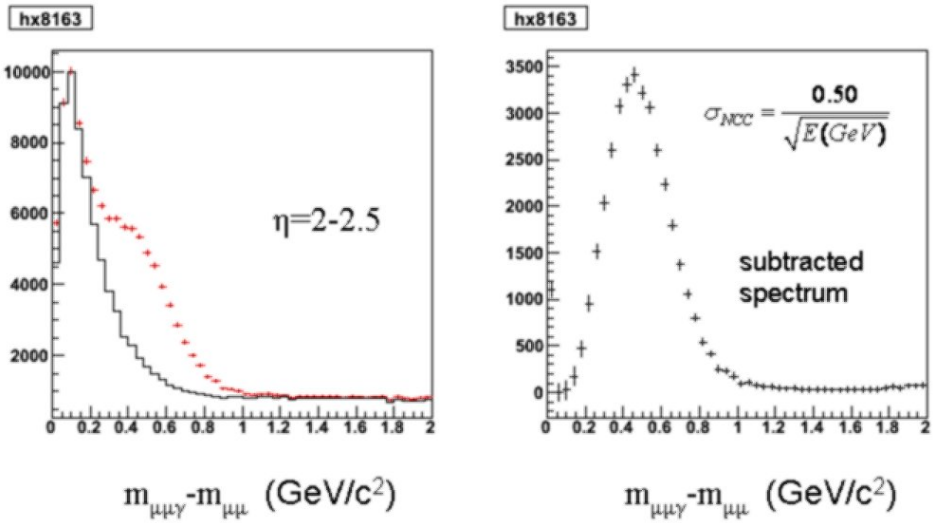

Figure B.6: Same as the previous figure with the resolution of the NCC degraded to $\frac{0.50}{\sqrt{(E(GeV))}}$

In heavy ion collisions, the combinatorial background is considerably larger. Fig. B.7 and B.8 show the χ_c signal for the top 10% ccentrality in Cu+Cu and Au+Au events. Even in central Au+Au events, the signal at rapidities 1-2 should be clear.

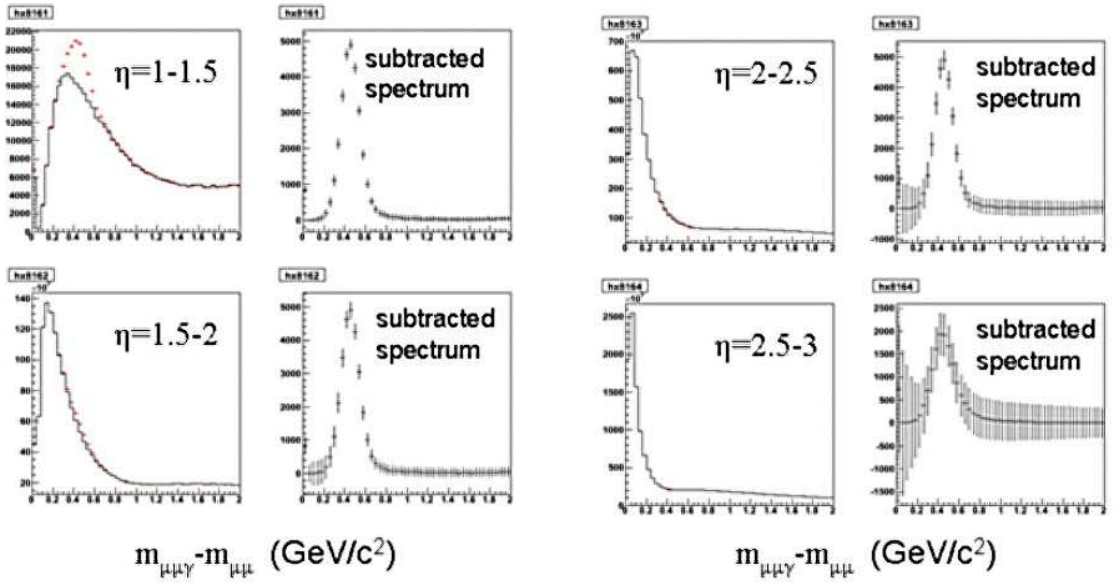

Figure B.7: Central 10% Cu+Cu events at various rapidities. The left plot of each pair show the raw mass difference, the right plot shows a background subtracted distribution.

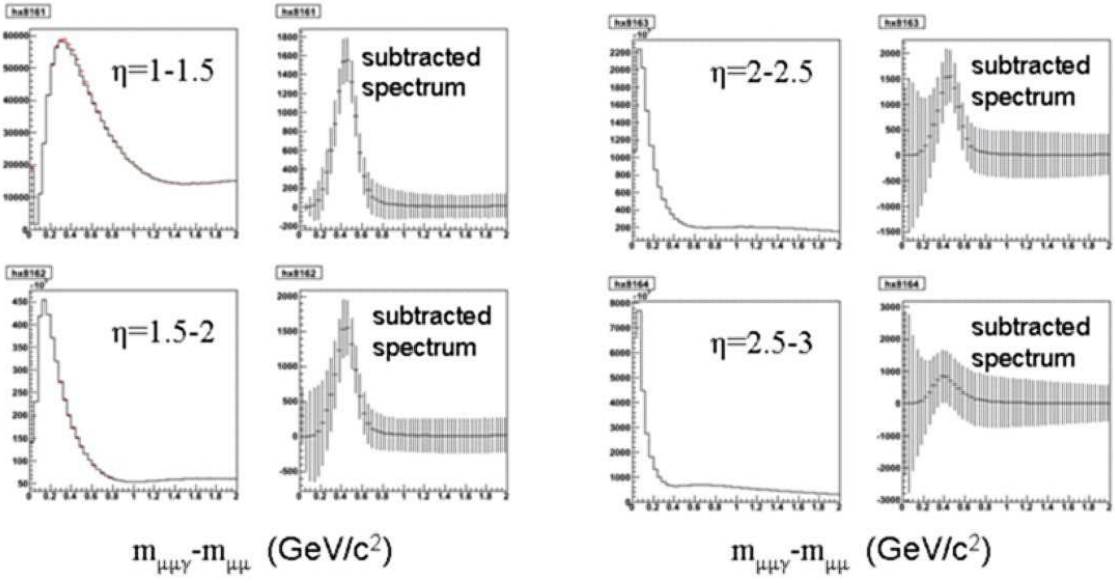

Figure B.8: Same as the previous plot for central Au+Au events.

B.3 Spin Simulations

The double longitudinal spin asymmetry A_{LL} for direct photon events gives the most theoretically clean access to the gluon polarization of the nucleon $\Delta g(x)$ because it is dominated by a single subprocess (Fig 2.x) and because one does not need to include the effects of fragmentation into a leading hadron. Jet events, if they can be reliably isolated, also allow one to avoid fragmentation uncertainties, but at the cost of a larger number of subprocesses which contribute to the asymmetry. Given a limited experimental acceptance, the asymmetry for production of a high p_T particle will typically yield the highest statistical precision, but one loses information about the particular kinematics of each event, in other words, the momentum fractions x_g of the gluon and x_q of the quark.

The present PHENIX spectrometer is only instrumented to detect photons and hadrons in the central rapidity region $\eta < |0.35|$, allowing an excellent measurement of A_{LL} with single photon and π^0 detection, but with limited ability to determine jet kinematics. The central rapidity is most sensitive to the gluon polarization at intermediate x. Given that the unpolarized gluon distribution is larger at somewhat lower x_g, there is strong interest to explore the gluon polarization to as low x_g as possible. The addition of the NCC immediately extends the range x accessible at PHENIX by nearly an order of magnitude lower, just by extending the acceptance for single photons. At the same time, it expands the range in rapidity for "jet" (or at least leading hadron) detection, thus giving a significant range over which the parton event kinematics, and hence x_g, can be determined. This range is further extended if the central (VTX) and end cap (FVTX) silicon vertex detectors are included.

In photon-jet events, assuming the dominance of the leading order graphs, one can measure x_g on an event-by-event basis by assuming that the lower x is that of the gluon and by measuring the angle of the jet, for example, as follows:

$$x_q = \frac{x_T}{2}\left(e^{+\eta_\gamma} + e^{+\eta_{Jet}}\right)$$

$$x_g = \frac{x_T}{2}\left(e^{-\eta_\gamma} + e^{-\eta_{Jet}}\right)$$

where

$$x_T = \frac{2p_{\gamma T}}{\sqrt{s}}$$

using the γ to determine p_T (this assumes intrinsic k_T effects are negligible in the kinematics).

In the following, we present the results of simulations of the accessible kinematics of the PHENIX spectrometer instrumented with the NCC, and assuming hadron detection for $\eta <\sim |2.5|$ (actually, the recoil parton η); this assumes therefore the inclusion of the VTX barrel and FVTX. Studies were performed for collision energies $\sqrt{s}$ of 200 and 500 GeV. The event generation is performed by PYTHIA using GRSV98 parton distribution functions Polarization effects are added by hand using the parton polarizations determined in AAC. The hard scattering asymmetry is calculated from the parton kinematics to leading order only. We have further applied a 10 GeV/c cut in p_T to photons.

The x_g range of the events are shown Fig. B.9, the number of gluon Compton scattering events which are detected as a function of $\log_{10} x_g$. The red points display the events with only

the existing (central) PHENIX photon detection, while the green points show the extension provided by the NCC. The black points provide a reference for the case in which there was full photon acceptance up to an η of 3. There are also clear regions of overlap between the NCC and central detectors which should allow crosschecks of the measurement of the gluon polarization.

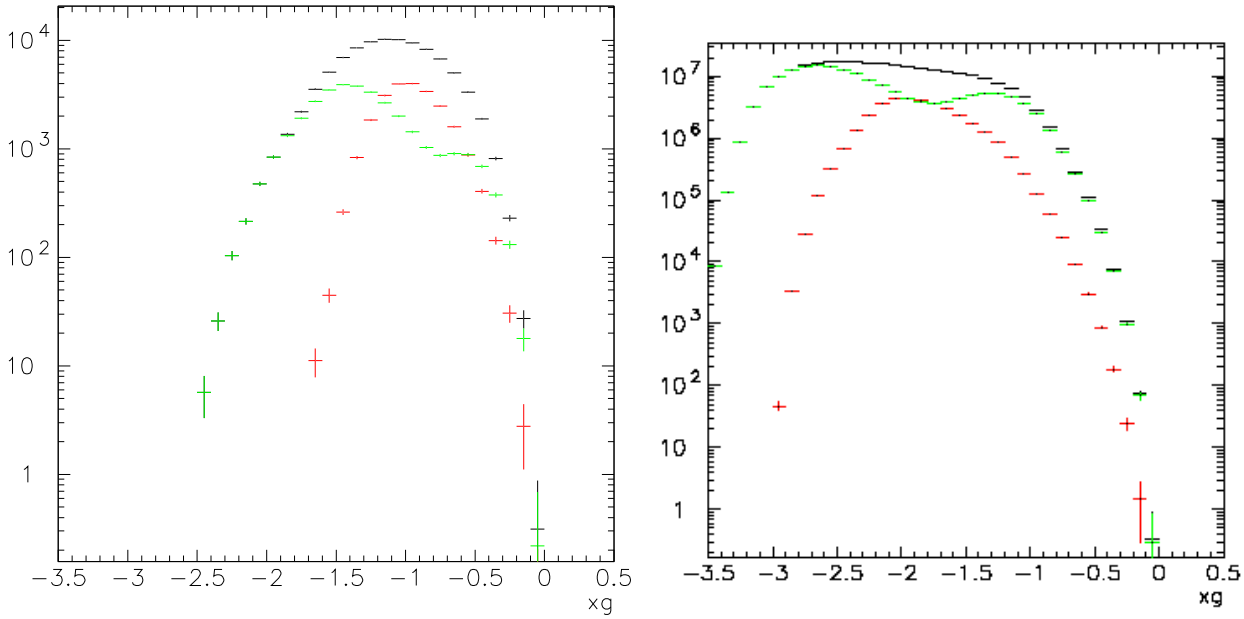

Figure B.9: Distribution of direct photon events at $\sqrt{s}$ of 200 (left) and 500 GeV (right). Red points refer to photons in the central detectors ($\eta < |0.35|$), while green points include the addition of the NCC ($1 < \eta < 3$). Black points show a hypothetical full acceptance ($\eta < |3|$).

This is where the power of the full PHENIX spectrometer will come into play. Using the tracking in the central SVX, the FVTX and the NCC PHENIX should be able to measure the jet angle over a large range. This together with the central EMC and the large acceptance of the NCC will give a measurement of both the photon and the jet over a nearly 5 units of rapidity giving access to $x_g \sim 10^{-3}$. It may be also be possible to disentangle events where the gluons are carrying a large momentum fraction to measure the spin structure functions at large x as well.

The actual double spin asymmetry as a function of photon p_T is shown in Fig. B.10, for $\sqrt{s} = 200$ GeV. The left panel shows the asymmetry measured in the central detectors, while that on the right shows the asymmetry for photons detected in the NCC. The simulation allows us to replot the asymmetry as a function of $\log_{10} x_g$, shown in Fig. B.11, clearly showing the range to which each acceptance is sensitive. One can directly see the range of $\Delta g(x_g)$ accessed (again via the simulation) in Fig. B.12.

Results of the simulation for $\sqrt{s} = 500$ GeV are shown in Figs. B.13. As expected, these measurements are sensitive to even lower x_g.

Further studies are underway to determine the effects of smearing from the actual photon

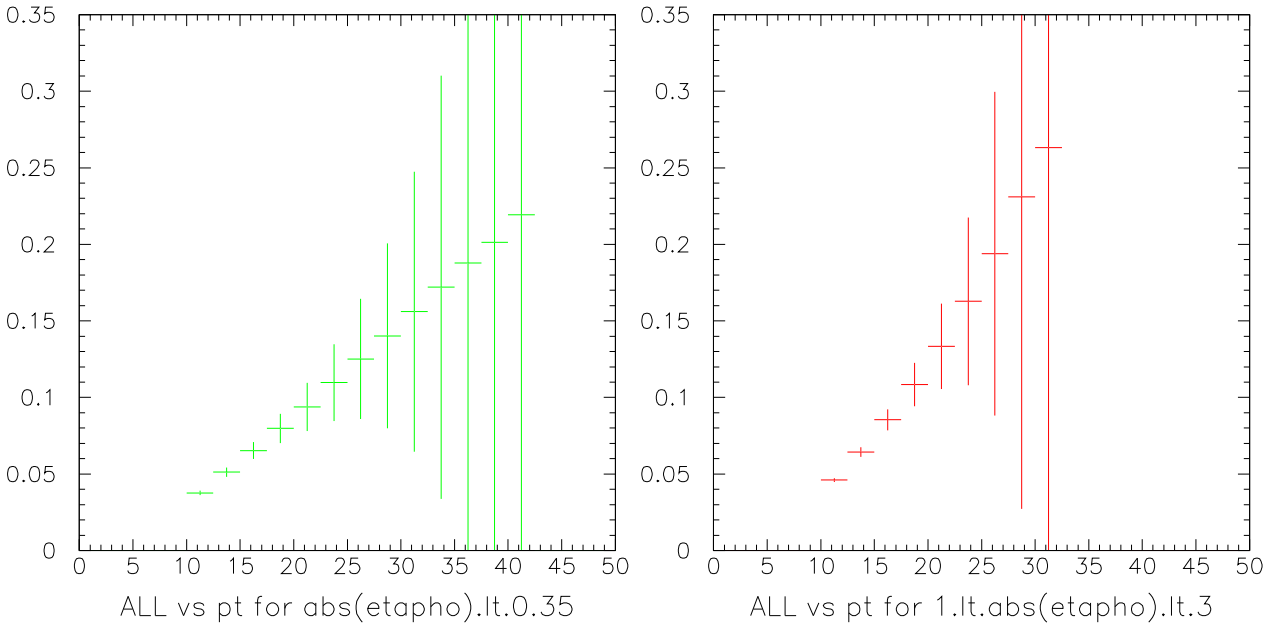

Figure B.10: Double longitudinal spin asymmetry for direct photon events at $\sqrt{s}$ of 200 GeV, as a function of photon p_T. The left panel shows the direct photon asymmetry measured by the central detectors ($\eta < |0.35|$), while the right panel shows the asymmetry measured by the NCC ($1 < \eta < 3$).

detection and jet angle resolutions for different detector configurations.

B.3.1 W Boson Isolation Cuts: The Quark Structure of the Nucleon.

While a cut on the pt of the muon can select W events, isolation cuts are traditionally used to clean up the signal offline. This is particularly important if there are fake muons coming from hadrons or hadron decays in the muon spectrometer. The isolation cut has been traditionally used to suppress the QCD background. Fig. B.14 shows that the one can get a suppression of the QCD background by a factor of 10, while loosing only 20

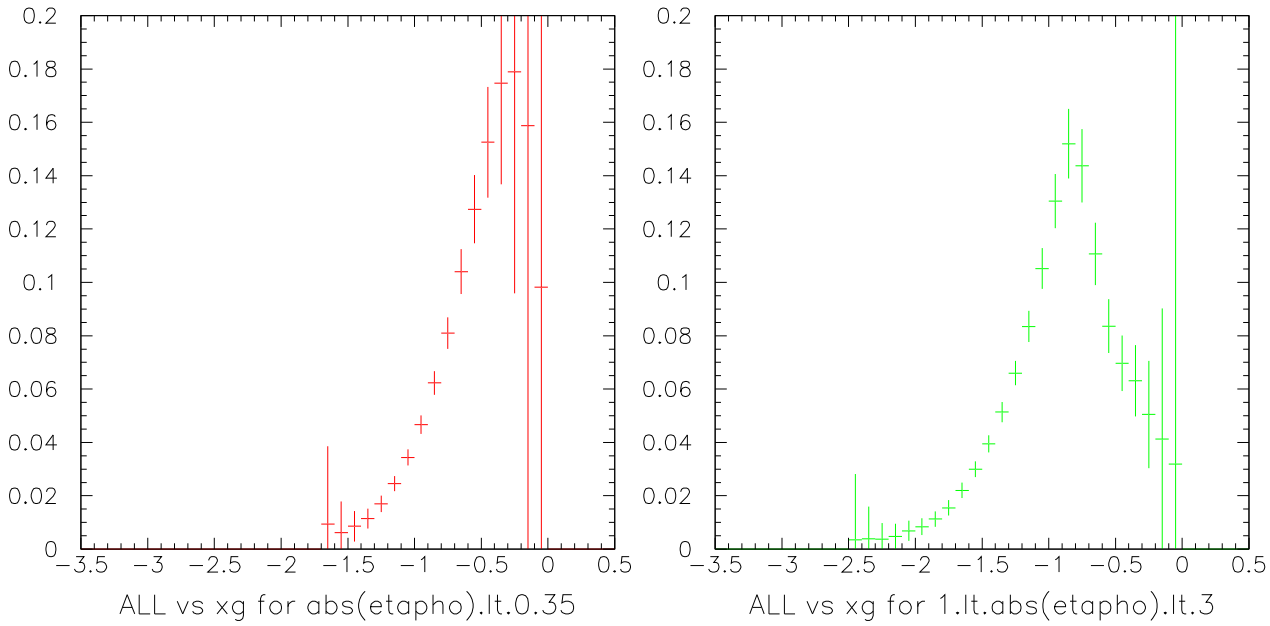

Figure B.11: Double longitudinal spin asymmetry for direct photon events at $\sqrt{s}$ of 200 GeV, as a function of $\log_{10} x_g$, as determined from the simulation. The left panel shows the direct photon asymmetry measured by the central detectors ($\eta < |0.35|$), while the right panel shows the asymmetry measured by the NCC ($1 < \eta < 3$).

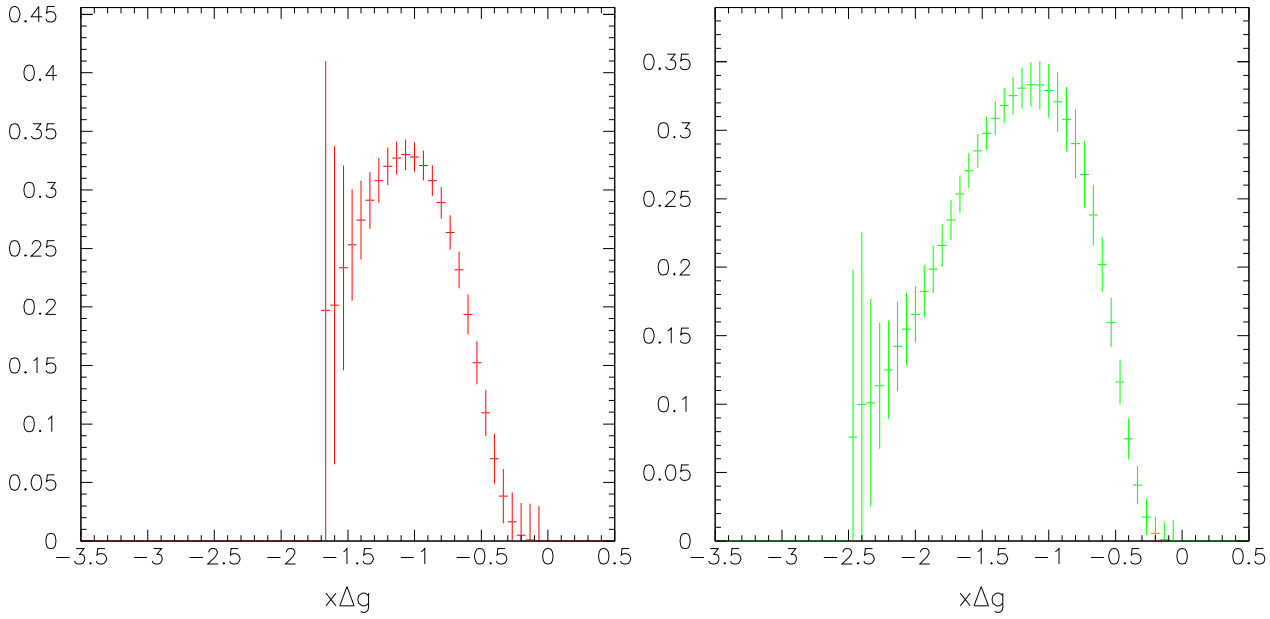

Figure B.12: Polarized gluon distribution function Δg for direct photon events at $\sqrt{s}$ of 200 GeV, as a function of $\log_{10} x_g$, as determined from the simulation. The left panel shows Δg measured by the central detectors ($\eta < |0.35|$), while the right panel shows Δg measured by the NCC ($1 < \eta < 3$).

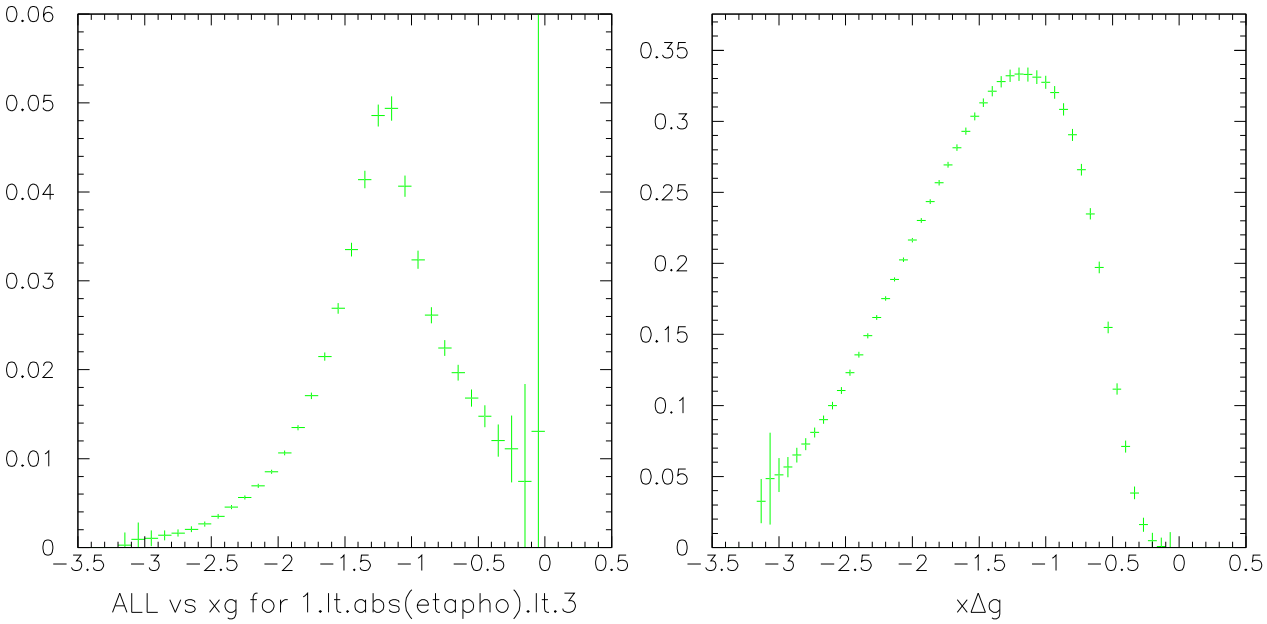

Figure B.13: Distributions for direct photon events at $\sqrt{s}$ of 500 GeV measured by the NCC ($1 < \eta < 3$) showing the reach to $x_g \sim 10^{-3}$. Double longitudinal spin asymmetry as a function of photon x_g (left). Δg (right).

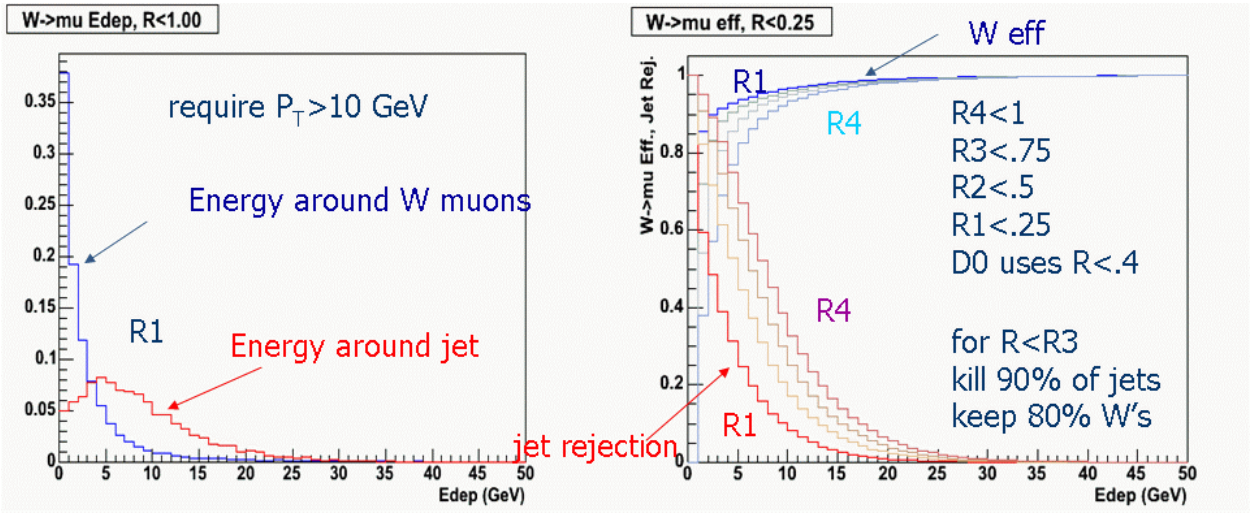

Figure B.14: (left) energy deposited around the muon in W events and jet events. (right) Suppression of background via isolation cuts.

B.4 Looking for a Colored Glass Condensate - a Simple Model

As an exercise, a model of the saturated gluon function [79] was used to understand what one might see in the simplest cases for the direct photon signal in d+Au collisions. Other models are now on the market with parameterizations that can used for such studies. However, the GBW model is simple in that it simply flattened out the Gluon distribution below some value of x, depending on the value of the saturation scale for the particular centrality and rapidity in question. Fig. B.15 shows an example.

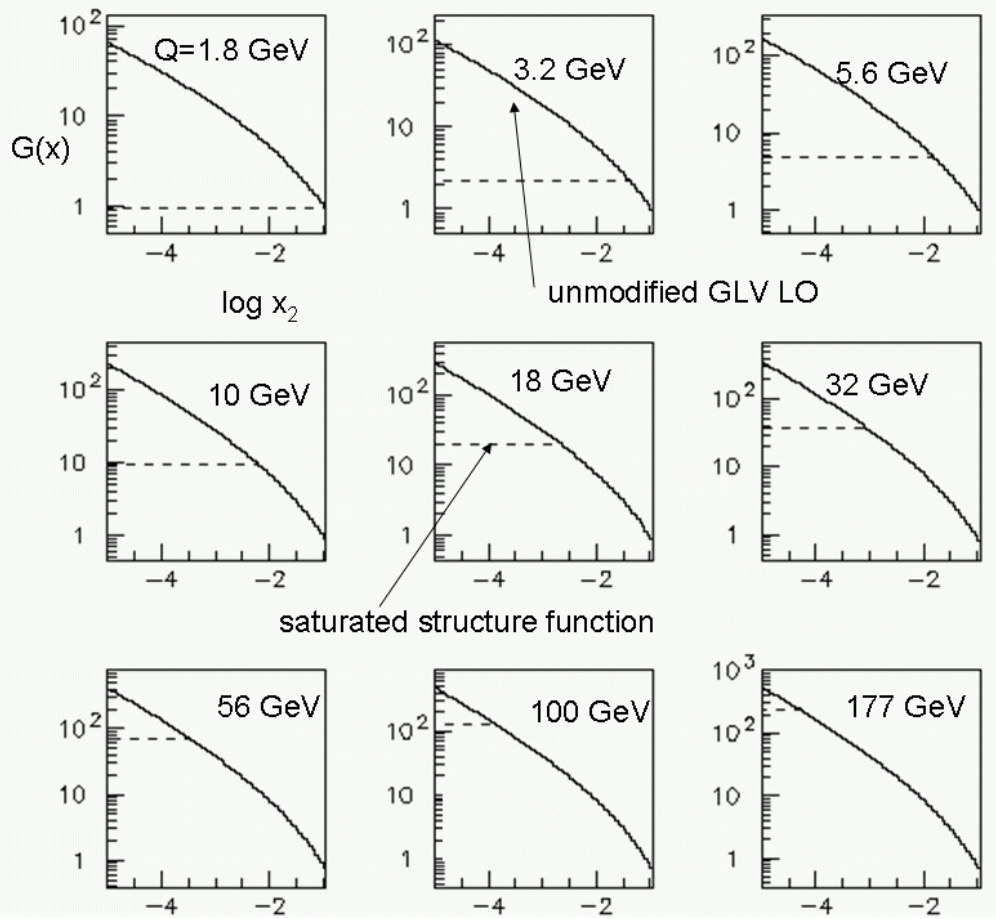

Figure B.15: Modified gluon structure function

R_{dAu} was then generated with these new distributions and checked against the measured values of R_{dAu} as measured by the PHENIX and Brahms collaborations for consistency. R_{pA} is defined similarly to R_{AA}

$$R_{pA} = \frac{dN_{pA}}{< N_{coll} > \times dN_{pp}} \tag{B.1}$$

where dN_{pA} is the differential yield for a point-like process in a p+A collision, and dN_{pp} is the differential yield for the same process in nucleon-nucleon collisions. The new gluon

distributions were then used in Pythia for the production of direct photon events and a ratio R_{pA} was constructed from the simulated data. Note that in Pythia there is no Cronin enhancement. Fig. B.16 shows R_{pA} as a function of η in various bins of p_T.

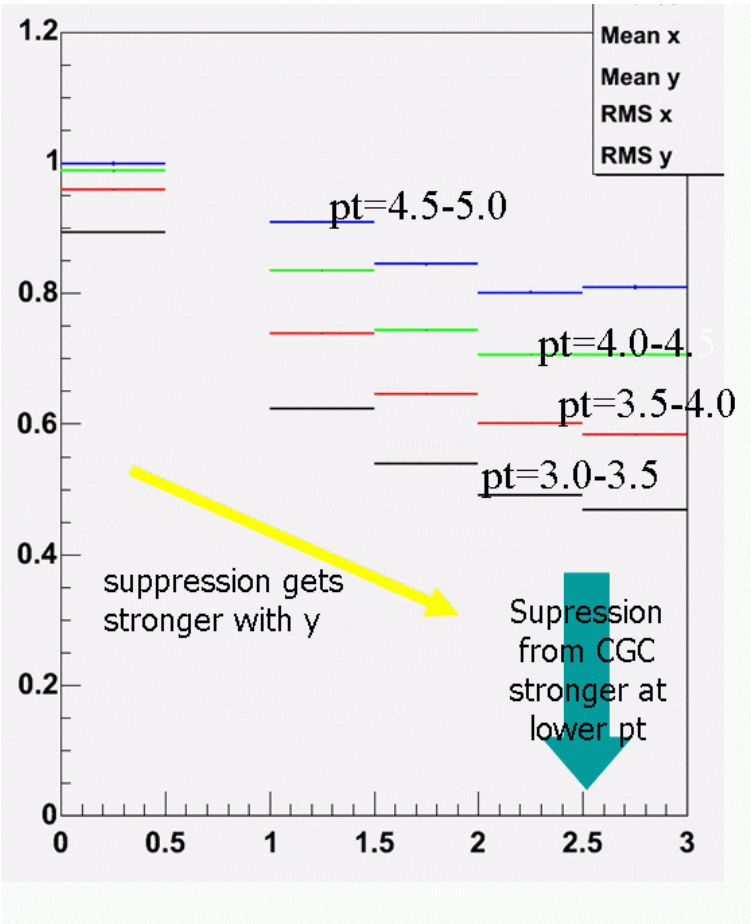

Figure B.16: R_{pA} shown as a function of η for various values of pt using a particular modified gluon structure function [79].

There are two characteristics that one sees: (1) The suppression increases for increasing rapidity, which makes sense because forward rapidity implies lower x. (2) The suppression is stronger at low p_T.

B.5 A Simulation Study of the Reaction Plane by the NCC

When two nuclei collide slightly off-center, the initial high-density volume has the shape of their overlap region during the collision. That region is elongated along an axis perpendicular to the reaction plane–that is, the plane defined by the beam direction and the line between the centers of the two nuclei as they collide. This asymmetry gives a natural way to vary the distance a parton travels in the collision volume before escaping. Using the correlated direct photon-high p_T particle measurements versus the reaction plane will give information on the energy loss as a function of the distance traveled in the medium. A measure of the reaction plane resolution is $< cos\psi >$ where $< cos\psi >$ is the correction factor of the reaction plane resolution and is simply called the "reaction plane resolution". Measurements are as a function of reaction plane are diluted by a factor $(\frac{1}{<cos\psi>})^2$. Hence larger values of $< cos\psi >$ refer to a better reaction plane resolution. Present measurements using the Beam-Beam counters have a reaction plane resolution of $< cos\psi >$=0.4. A reaction plane detector is being proposed to increase this to $< cos\psi >$=0.7. The NCC will have a reaction plane resolution $< cos\psi >$=0.9. The following explains the simulation work to obtain this resolution.

The NCC detector is defined and installed in PISA GEANT simulation to replace the entire nosecone. Using the given geometry, a single particle simulation with charged and neutral pion was performed to prepare a mapping file, which covers full phase space (rapidity, p_T, ϕ) with uniform distribution. The mapping file is then used in the 2^{nd} step of simulation, which include realistic multiplicity (charged pion and π^0) and flow (v_2) depending on the p_T and rapidity. Therefore, the backgrounds from other detector elements as well as NCC itself are included. Fig. B.17 shows an overlay of several single track events.

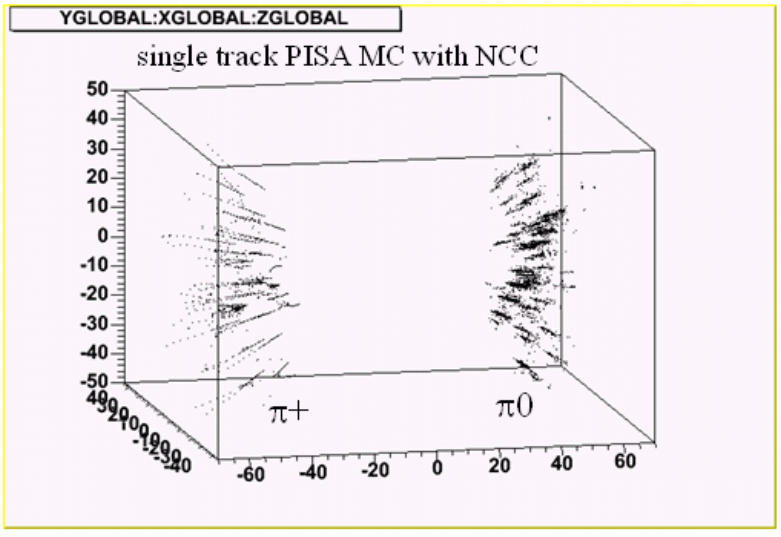

Figure B.17: An overlay of GEANT events in the NCC

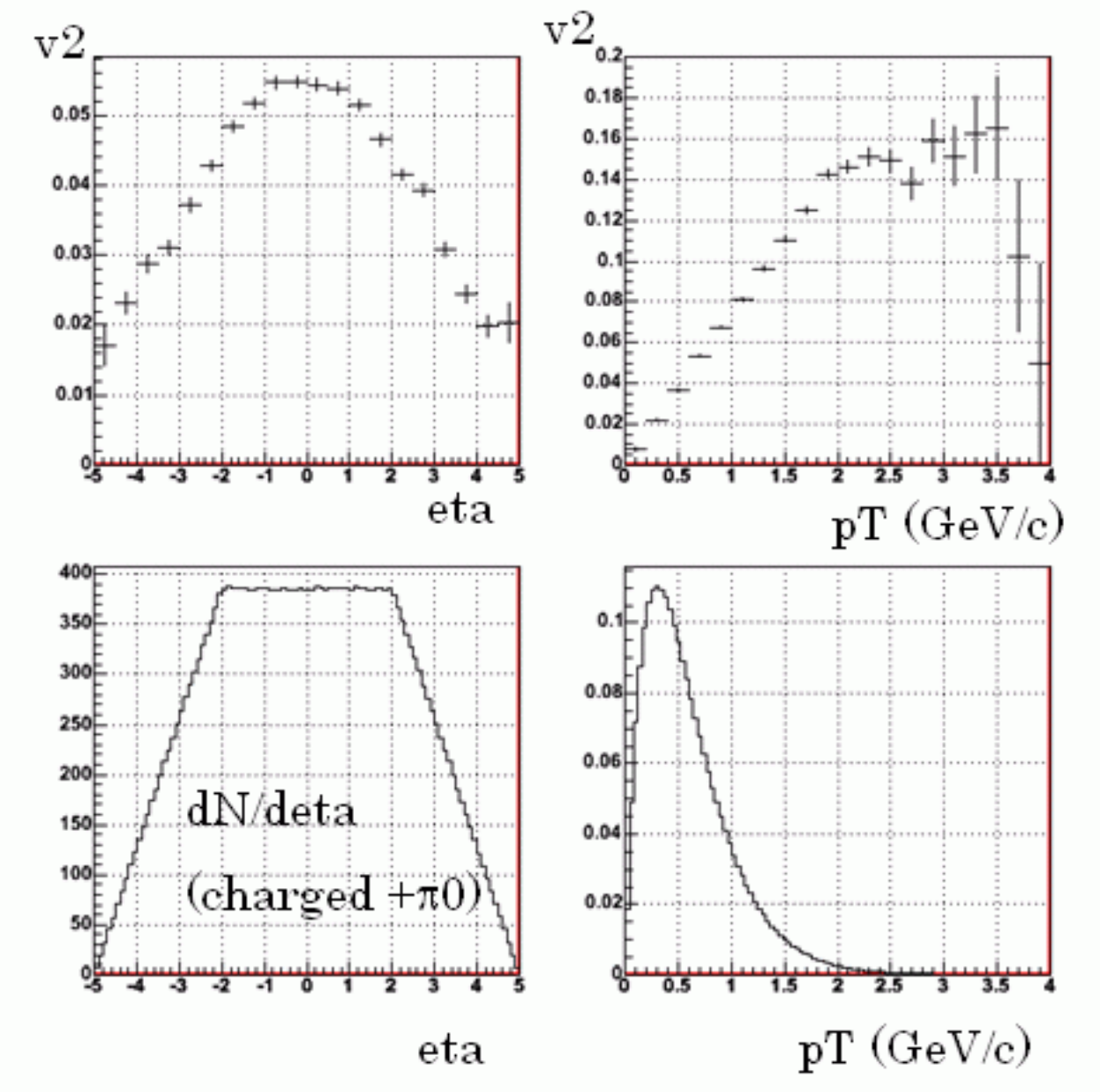

Figure B.18: Input flow (v_2) values as a function of η and p_T used in the simulation [top two panels]. η and $p_T$distributions used in the simulation [bottom two panels].

Input flow values and multiplicity used in the 2^{nd} step of simulation are shown in Fig. B.18. The top 3 panels in Fig. B.19 show the hit position in x-y on the NCC detector for 3 different z sectors, the first electro-magnetic sector (EM1) and the second electro-magnetic sector (EM2) after SM ID strip layer and the third hadronic sector (HAD). The radial hit distribution, azimuthal hit distribution with respect to the generated primary track and azimuthal hit distribution with respect to the simulated reaction plane orientation are shown in the bottom three panels in Fig. B.19.

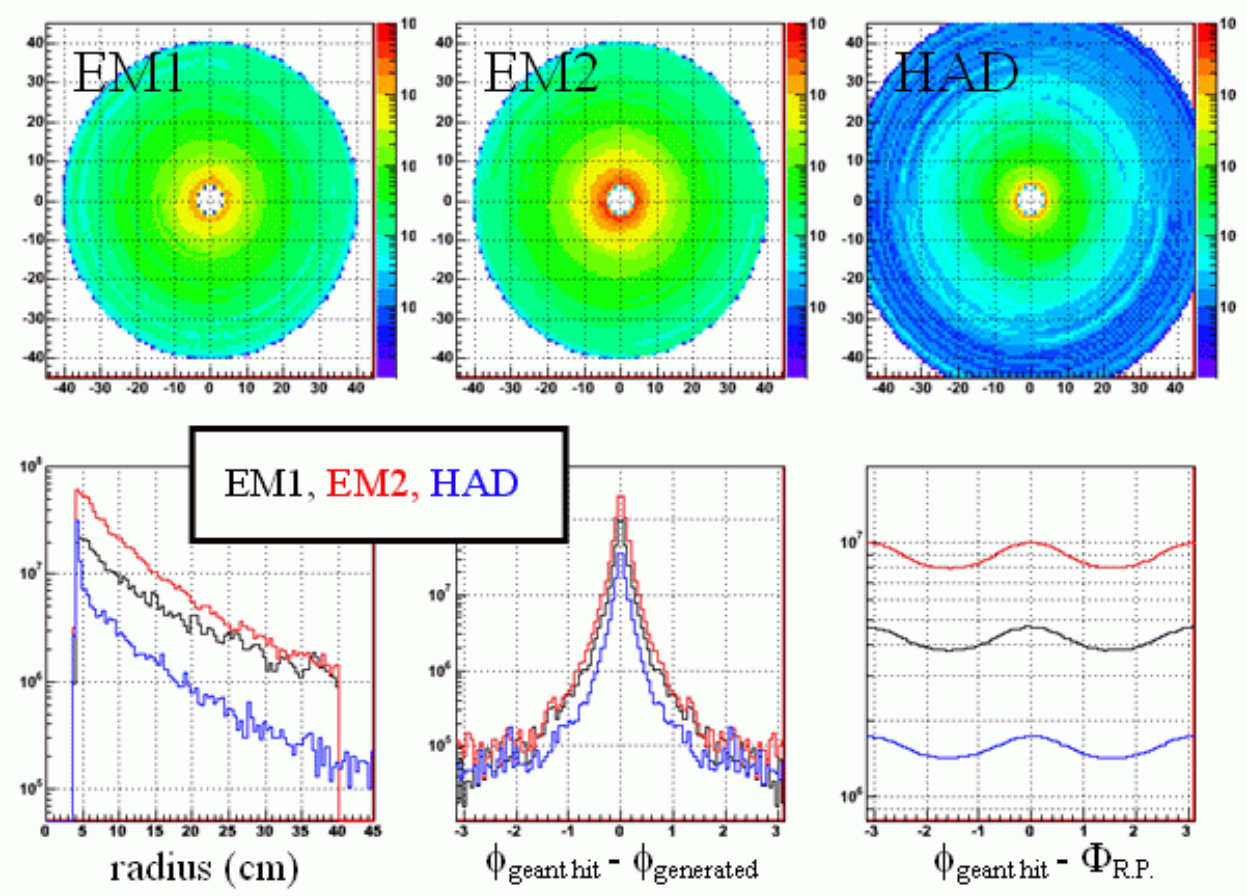

Figure B.19: Hit position in x-y on the NCC detector for in EM1, EM2, and HAD(top 3 panels). Radial hit distribution, azimuthal hit distribution with respect to the generated primary track and azimuthal hit distribution with respect to the simulated reaction plane orientation(bottom 3 panels).

Fig. B.20 shows the reaction plane distribution ($\Phi_{calc} - \Phi_{true}$) with different weighting methods described in the figure caption. The bottom panel shows the reaction plane resolution with different cases as described in the figure caption. The resolution goes up from about 0.8 in the case (2) with charged particle alone to about 0.9 case (7) by including $\pi 0$ conversion, dE/dx weighting and optimizing the weight. The three regions in the bottom panel show the radial dependence of the reaction plane resolution for each z sector, the pink dashed lines show parameterized function of radial dependence of resolution, which is used to weight each reaction plane to get the best resolution in the case (7).

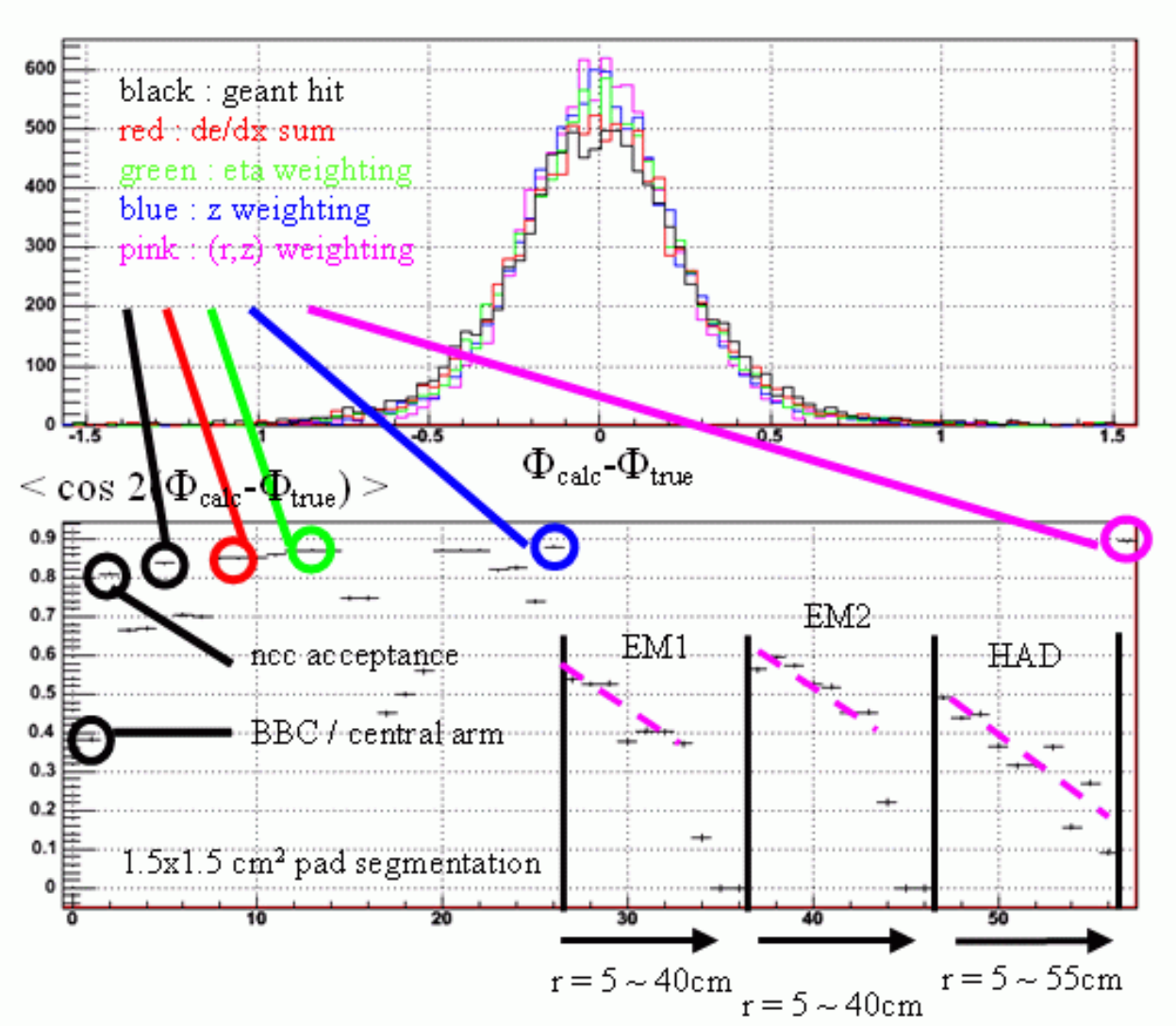

Figure B.20: (top) The reaction plane distribution ($\Phi_{calc} - \Phi_{true}$) with different weighting methods. (Bottom) Reaction plane resolution for different cases, where the conditions marked with circle are described in the following. (1:black) BBC or central arm reaction plane resolution is about 0.4, (2:black) use all charged particles in NCC acceptance, (3:black) use all GEANT hits in NCC, (4:red) weighting all the GEANT hits with dE/dx, (5:green) v2 weighting according to eta dependence of v2 in addition to (4), (6:blue) z sector depending weight in addition to (5), (7:pink) 2 dimensional r, z weight in addition to (5). The resolution goes up from about 0.8 in the case (2) with charged particle alone to about 0.9 case (7) by including π^0 conversion, dE/dx weighting and optimizing the weight.

B.6 Muons and Background

In addition to the topics covered in the main text, the NCC can be used together with other detectors to solve some problems - in this case the identification of muons.

The major sources of hard muons are

1. the semi-leptonic decay of heavy flavored quarks in the intermediate p_T (transverse momentum) range of $2 \sim 15$ (GeV/c),

2. the decays of W bosons above very high p_T of above 20 (GeV/c).

Heavy flavor production and W boson productions at RHIC are of great interest. As an example, the major focus of the ongoing muon trigger upgrade is to understand spin structure of the protons through very high p_T muon measurement. With the luminosity upgrade and the muon trigger upgrade, we will reach very high p_T regime beyond our current statistical limit.

Beyond the statistical limitation, one of the major challenges in achieving high p_T muon measurement is a fake high p_T background. The background originates from a small fraction of the soft light hadrons, $\pi^{\pm}$ and $K^{\pm}$ which penetrate the front absorber composed of the NCC and magnet yoke, and subsequently decay into muons between muon tracking station 1 and station 3 , and are reconstructed by chance. The rigidities of the reconstructed trajectories are determined by the bend angle between tracking station 1 and tracking station 3. Decays can fool this rigidity determination and generate seemingly hard tracks with a rare, but significant occurrences. Fig. B.21 shows the reconstructed p_T distribution from various p_T ranges of the light hadrons generated with realistic multiplicity for p+p collisions at $\sqrt{s} = 500GeV$. For each range, a small fraction (10^{-3} to 10^{-4}) contributes to the fake hard p_T distribution. Due to the large multiplicity, low p_T hadrons dominate the real muon contribution from W decays even at very high p_T.

The NCC is positioned between the collision location and the tracking station 1, and measures crossing locations of the reconstructed trajectories at the accuracy of about 150 μm at two independent planes - PS and SM. While real high p_T tracks travel along a straight line trajectory between the collision location and the tracking station 1, fake high p_T tracks do so with large deflections inversely proportional to the momenta. So, for a chosen momentum or p_T, we can select a narrow window of possible deflection ranges and reject fake high p_T tracks with large deflections my matching hits in the PS or SM of the NCC. Fig. B.22 shows the reconstructed p_T distribution similar to Fig. B.21, but with a window optimized for $p_T \sim 25$ (GeV/c). According to a preliminary study, the finite NCC occupancy in p+p collisions at $\sqrt{s} = 500$ GeV does not degrades the performance, but performance degradation due to the large occupancy in Au+Au collisions must be investigated.

In conclusion, nose cone calorimeter (NCC) can reject fake high p_T tracks effectively, and will help prompt muon measurements.

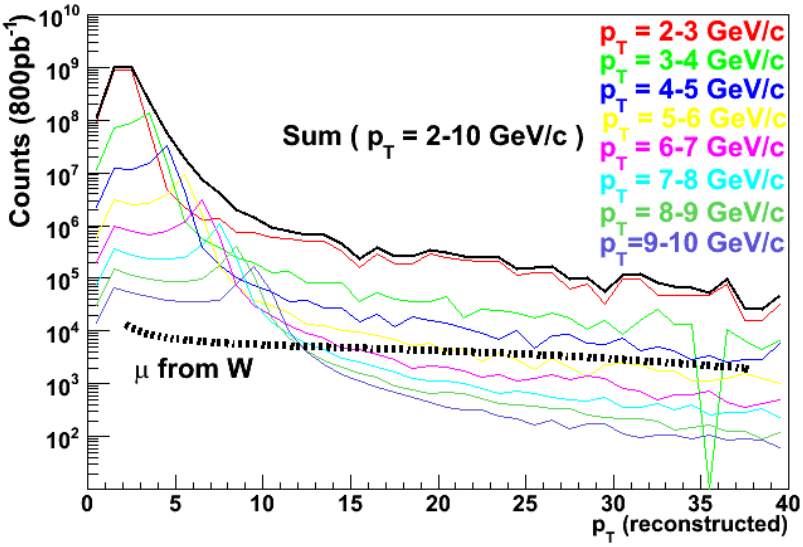

Figure B.21: . Reconstructed p_T distribution from various p_T intervals of produced light hadrons. Muons from W boson decays are also shown.

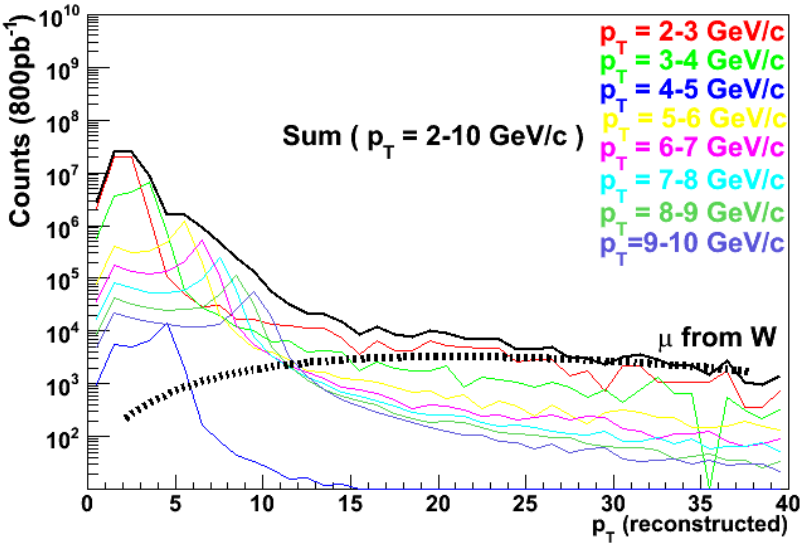

Figure B.22: Distribution similar to Fig. B.21, but with the background suppression by matching tracks from the muon spectrometer to the NCC.

Appendix C

NCC Silicon Strip Sensors

As described in Chapter 3, we plan to instrument the preshower and shower max layers of the NCC with silicon strip detectors of a novel design. The sensors developed by the BNL Instrumentation Division provide two-dimensional position sensitivity. The readout of sensors is based on SVX4 chips, which were developed for silicon strip detectors by FNAL and LBL. In the final readout system the SVX4 chips would be arranged on readout cards SRC's and mounted directly on the sensors.

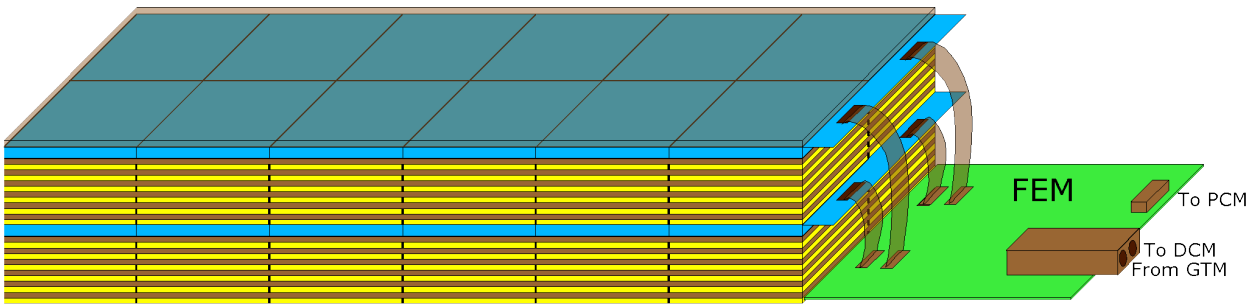

Figure C.1: Conceptual layout of the NCC electromagnetic brick. Blue layers are silicon-strip planes (preshower and shower max); brown layers are tungsten plates, yellow layers – silicon-pad readout planes. Both silicon strip planes are read by FEM board located inside the bricks envelope. The FEM sends data to PHENIX DCM boards over optical fiber. Power and ground are distributed from a PCM board located near the detector.

C.1 Design

The sensor is segmented detector with 0.5mm x 0.5mm pixels. Fig. C.2 shows that each pixel region has two comb-shaped metal strips that collect charge produced by an ionizing particle transversing the silicon. Each hit by an ionizing particle deposits charge on two combs. The vertical combs are connected by metal strips, and the horizontal combs are connected by polysilicon strips. The readout pads are arranged on two edges of the sensor.

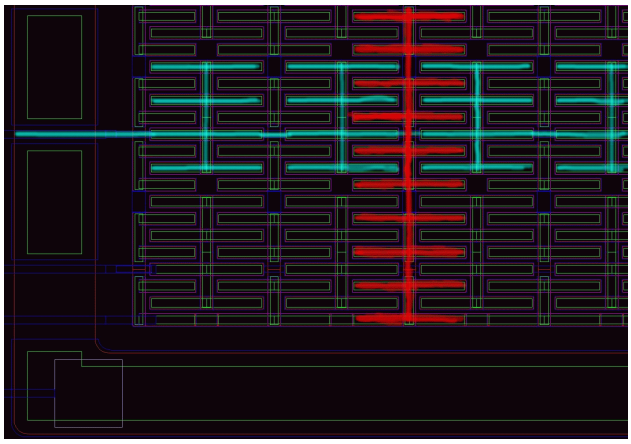

Figure C.2: The lower left corner of the silicon strip-pixel sensor. One of the horizontal combs is highlighted in blue and a vertical comb in red. The width of both combs is 0.5 mm.

FigureC.3 shows the wafer fabrication mask of the pre-prototype strip sensors. The total size of the sensor is 60mm x 60mm. The first batch of these sensors have been fabricated in October 2005 but did not pass the tests. The new set of masks is now prepared and scheduled for fabrication.

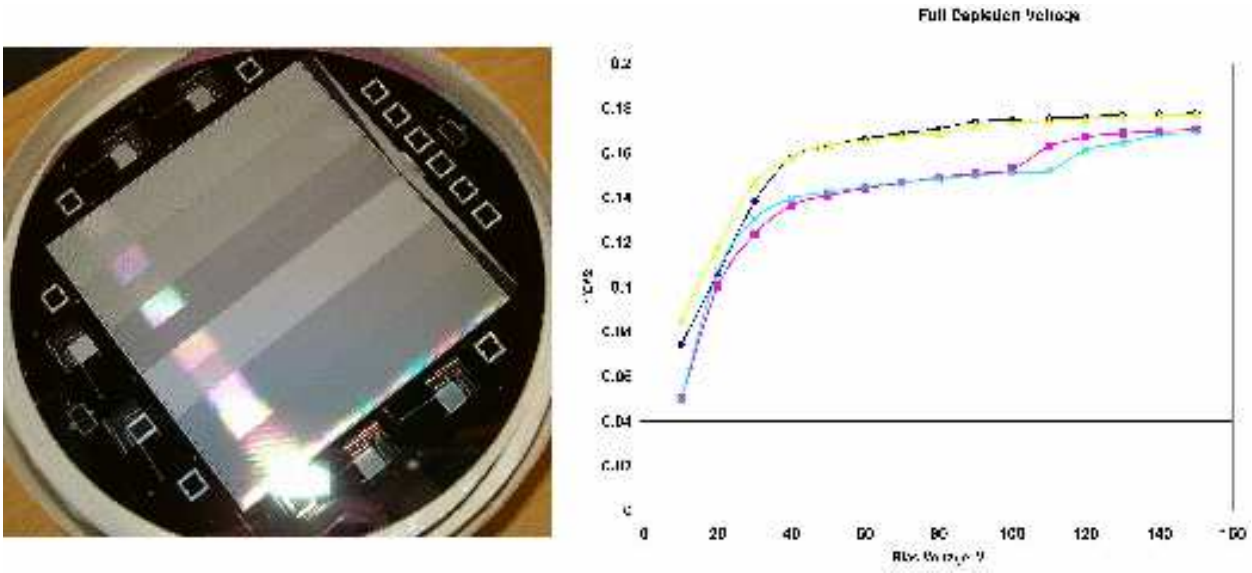

Figure C.3: Pre-prototype silicon wafer and IV curve of the test diode structures.

C.2 SVX4 Readout Chip

The strips will be read out with the SVX4 chip developed by FNAL/Berkeley collaboration. The SVX4 is implemented in the 0.25 μ TSMC process and is inherently rad-hard. It is a

128-channel chip with a 46-deep pipeline cycled by the beam-crossing clock, thus providing the LVL1-latency required by the PHENIX DAQ. LVL1-accepted events are stored for future pipelined readout. The SVX4 allows up to 8 bits of analog information, although the number of bits are programmable. Several pedestal-subtraction steps offer robust protection against common-mode noise. On-board zero suppression is provided for, but can be turned off (see discussion below). The SVX4 also provides for four-deep multi-event buffering required by the PHENIX DAQ.

C.3 Sensor Readout Module (SRM)

The sensor readout module shown in Fig. C.4 consist of two silicon stripixel sensors and a Sensors Readout Card (SRC) mounted on top of them. Sensors are wire bonded to the edges of the SRC. The SRC is a 0.25 mm thick PCB board manufactured with minimal line width of 75 μgnd minimal line space of 75 μu The board hosts 4 SVX4 chips.

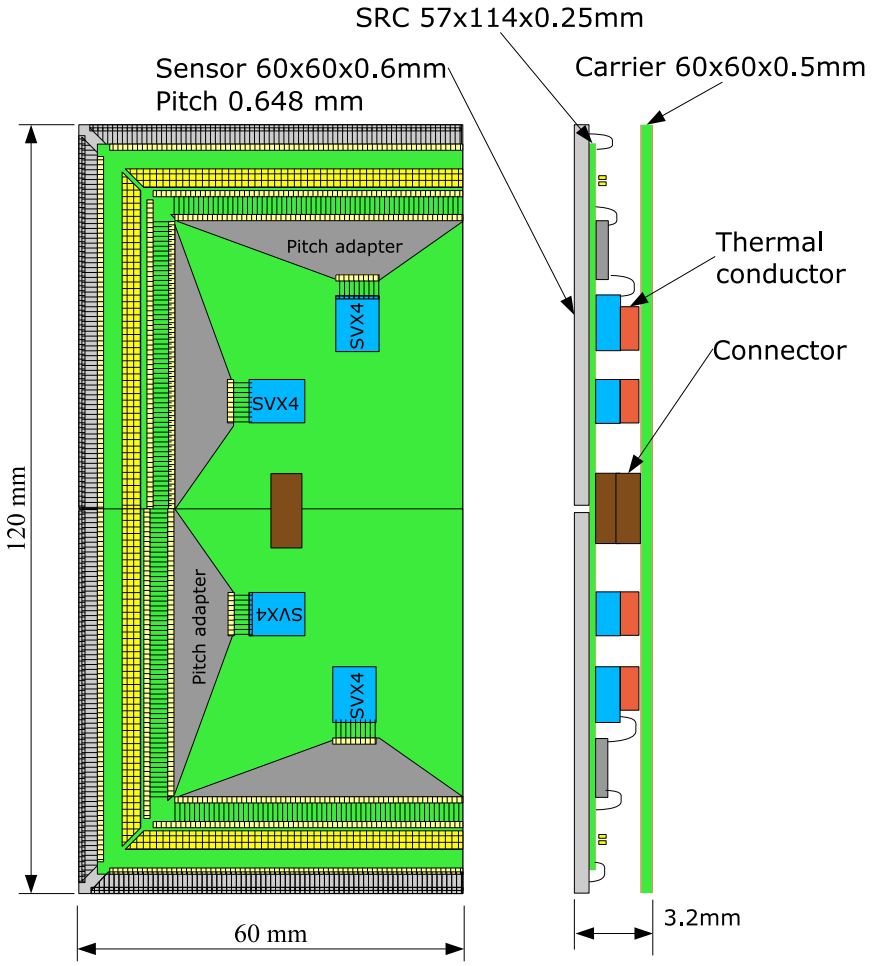

Figure C.4: Sensor Readout Module.

We decided to manufacture the silicon sensors as **DC-coupled** based on following considerations:

1. Higher production yield,
2. Higher reliability during operation and
3. 25% lower cost.

At the same time we plan to integrate biasing resistors directly on the sensors. This will help us to greatly simplify the production tests and characterization procedures by allowing simultaneous biasing of all strips. Connection of DC-coupled sensors to SVX4 chips requires an AC-decoupling network. This network is build using SMT 0201 type capacitors. We have manufactured a prototype PCB with wire bonding pads on one edge. The RC decoupling network occupies an area of 38mm x 9mm.

Fig. C.5 shows the layout of the prototype SRC capacitor network for the final PCB (with wire bondingpads on two edges), illustrating that it is feasible to include all components.

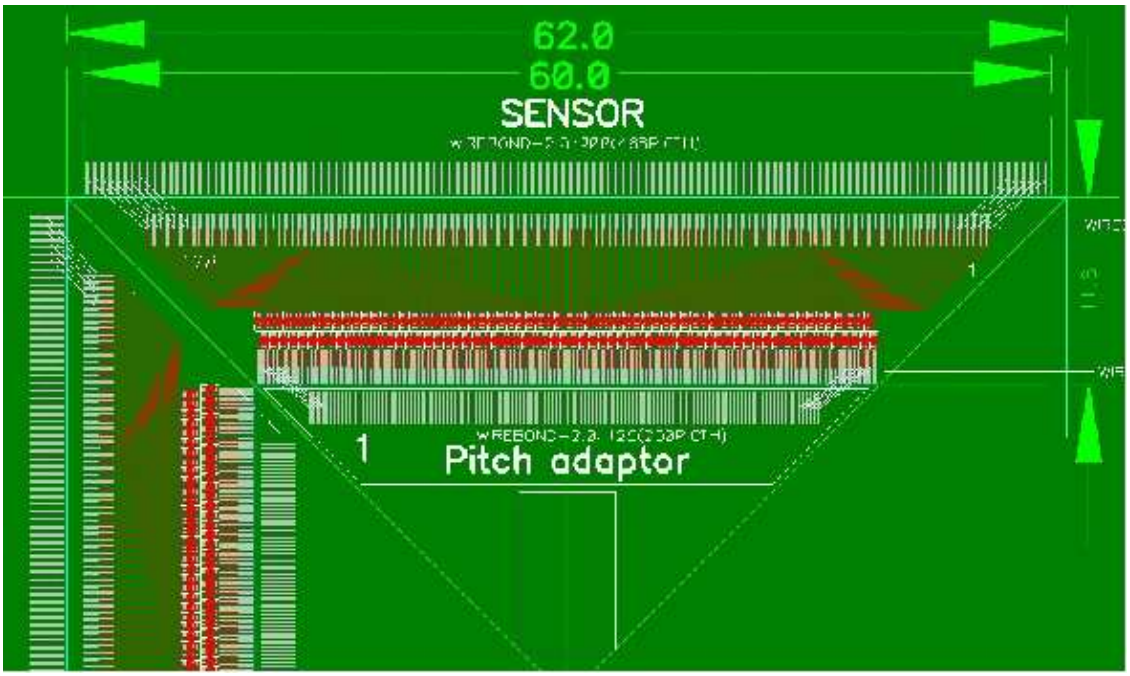

Figure C.5: Layout of the prototype SRC.

The pitch adapter is metal-on-silicon bare die produced from the same wafers as sensors.

The sensor readout modules are mounted on a Carrier board – a 0.5 mm thick PCB which distributes power supply, ground and bias voltage. It also contains 4 readout chains for SRC. The Carrier board provides heat transfer for SVX4 chips. The Carrier board can host 5,6 or 7 SRMs.

The slow control and monitoring of the SRM is done using 1WIRE devices. The following parameters are monitored:

1. Temperature (it is easy to monitor it in several locations). DS18B20X chip.
2. Leakage current
3. 3 control voltages. DS2450 chip.

The setup voltages for SVX4 like VTH and VCAL are also controlled by 1WIRE devices (DS2890).

Power consumption The main power consumption sources on the SRM are SVX4 chips. The average load current per chip is 52mA from AVDD and 13 mA from DVDD, which correspond to 0.22W. The AVDD load depends on the preamp current setting and can reach 90 mA. The average power dissipation per silicon-strip plane is expected to be of the order of 10W.

C.4 Front-End Module (FEM)

The FEM has 4 readout chains for the SVX4. Figure C.6 shows the block diagrap and Fig. C.7 shows the dimensions.

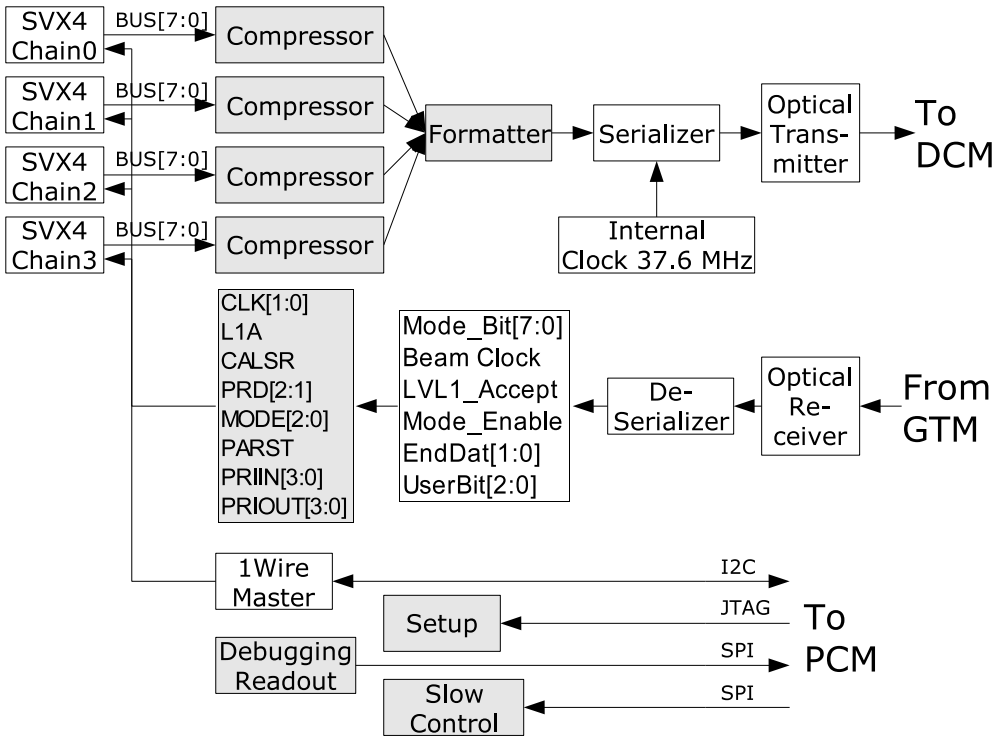

Figure C.6: FEM Block Diagram. Shaded boxes show the elements implemented in the FPGA.

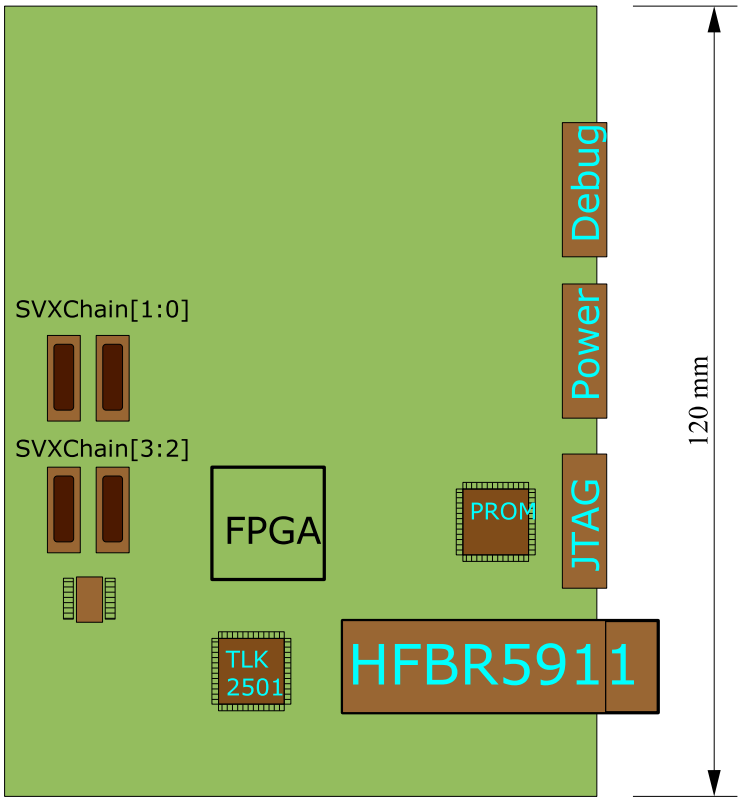

Figure C.7: FEM Dimensions

The LVDS data busses are independently fed into a SPARTAN FPGA. The FPGA buffers the event into an input buffer, compresses the data stream using Huffman Coding, stores the result in the output buffer and sends it through the optical transceiver to the PHENIX DCM. The PHENIX DAQ requires that all subsystem should be able to buffer at least 5 events. The SVX4 chips on the SRC have internal buffering for 4 events; the FEM will provide at least one additional buffer.

The FEM connects to the PHENIX DAQ over a small-form-factor (SSF) optical transceiver, the receiving part of which is connected to a PHENIX GTM module, and the transmitter part is connected to a PHENIX DCM module.

These signals are de-serialized using a SerDes chip. The clock is defined by a Phenix GTM; it is four times the Beam Clock, i.e. 37.6 MHz. This clock is recovered by the SerDes chip; the clock jitter is guaranteed to be less than 40 ps. The transceiver and SerDes are mounted on a small mezzanine board and will be compatible with the optical protocol of the latest DCM.

C.4.1 Time budget

The digitization at 37.4 MHz Front-End clock will be finished in 1.7 us. It is important to keep this time as short as possible because the SVX4 chip cannot do digitization and readout simultaneously.

Phenix Synchronization Signals	
Mode_Bit[7:0]	8
Beam Clock 9.4 Mhz	1
LVL1_Accept	1
Mode_Enable	1
EndDat[1:0]	2
UserBit[2:0]	3
Reserved[3:0]	4
Total	20 Bit

Figure C.8: Signals received by the FEM from the GTM

Figures C.9 and C.10 show the Digitization Readout Times and the Data Transfer Times.

Digitization and Readout Time		
SVX4 Front-End Clock	37.6	Mhz
Digitization time	1.7	us
Longest SVX4 chain	16	
Number of SVX4 chains per FEM	4	
SVX4 Back-End Readout Clock	37.6	Mhz
Chain size for calibration run	4128	Bytes
Receiving time for calibration run	54.89	us
Occupacy	5%	
Average chain size	236.8	Bytes
Average Readout Time	3.15	us

Figure C.9: Digitization and Readout Times

The longest chain has 16 SVX4 chips assuming a 5% occupancy. The size of the average chain will be 237 bytes with averagte reaout time of 3.15 μs. During this time the SVX4's are open to aquire up to 4 new triggers.

For normal data taking with pedestal suppression and Huffman compression (we expect that Huffman coding of pedestal suppressed data can achieve compression factor of 3:1) the estimated data size from the whole brick is 276 bytes. With DCM clock of 40 MHz this data will be transferred in **7.35** μ**s**. This fits safely into the PHENIX DCM data-taking window (ENDAT) of **40** μ**s.**

The optical transmitter will be clocked by an internal clock generator to eliminate uncontrolled jitter of the beam related clocks, which could result in high probability of data losses.

Note. Even for calibration runs when pedestal suppression is switched off the data size will be reduced from 14.5 Kbytes to 3.0 KB by removing ChannelID bytes from the SVX4

Data Transfer Time		
Input data size, without pedestal suppression	14448	Bytes
Output data size, without pedestal suppression	7284	
Compression factor for unsuppressed data	2.5	
Compressed output data, calibration run	2914	Bytes
Hit occupancy	5%	
Output data size, pedestal suppressed	829	Bytes
Compression factor for suppressed data	3	
Output data size, suppressed & compressed	276	Bytes
DCM receive clock	37.6	Mhz
Data transfer time, calibration run	77.49	us
Data transfer time pedestal-suppressed and compressed	7.35	us

Figure C.10: Data Transfer Times

data and applying Huffman compression. The data transfer time in this case will be 77.5 μs, which can be handled by a single DCM by occupying two ENDAT windows of the DCM.

C.4.2 FPGA Selection

C.4.2.1 Memory Requirements

BEM Memory Requirements		
Number of ladders in brick	2	
Max Number of SEM in a Ladder	7	
Number of SVX4 in SEM	4	
Max Number of SVX4	56	
Number of channels	7168	
Max data size per SVX4	258	Bytes
Max input data size	14448	Bytes
Number of input buffers	1	
Output data size unsuppressed	7284	Bytes
Compression factor for unsuppressed data	2.5	
Output data compressed	2914	Bytes
Hit occupancy	5%	
Output data size, pedestal suppressed	829	Bytes
Compression factor for suppressed data	3	
Output data size, suppressed & compressed	276	Bytes
Size of the pedestal memory	7168	Bytes
Size of the Huffman coding map	512	Bytes
Total memory requred	**29412**	**Bytes**
	235296	**Bits**

Figure C.11: BEM Memory Requirements

FPGA	Dist RAM [Kbits]	Block RAM [Kbits]	DCM	FT256 IO USER	FT256 IO DIFF	Price	Source
XC3S500E	73	360	4	190	77	?	
XC3S1200E	136	504	8	190	77	?	
XC3S400	56	288	4	173	76	$27.76	digikey
XC3S1000	120	432	4	173	76	$47.87	digikey

Figure C.12: Spartan FPGA

The XC3S400 has sufficient memory resources for our application.

C.4.2.2 Number of LVDS pairs.

According to table 3 the FEM should process data from four SVX4 chains in parallel. This will require

1. Data transfer bus 4 x 9 = 36 LVDS pairs.
2. Common clocks BECLK, FECLK. = 2 LVDS pairs
3. PRIOUT[0] 4 x 1 = 4 LVDS pairs
4. Optional PIOUT[3:1] 4 x 3 = 12 LVDS pairs

In total it is 42 obligatory and 12 optional pairs

The XC3S500E is most attractive and it could be less expensive in near future but as of today the SPARTAN3E FPGA have very long lead time and still more expensive than SPARTAN3. Both the FPGA XC3S400 and XC3S1000 meet all requirements, are not expensive, and are readily available.

C.4.3 FEM Ports

C.4.3.1 SVX4_Chain[3:0] ports

These ports carry signals only; the power, bias voltage and ground for SVX4 will be routed separately on the Carrier board. The longest SVX4 chain has 16 SVX4 chips, see table 2. For better reliability the chain control signals, PRIIN and PRIOUT, are broken into four groups (PRIIN3:0, PRIOUT3:0), each serving one SEM module. This adds flexibility to bypass any group for configuration or readout.

The JTAG_COMMON port connects PCM (Power and Control Board) to all FEMs in parallel. JTAG_IN and JTAG_OUT are daisy chained.

The debug port controls the FEM boards from the PCM and provides:

SVX4Chain Port			
Pin	Signal	Pin	Signal
1	PRIIN1	2	PRIOUT1B
3	PRIOUT2B	4	PRIOUT1
5	PRIOUT2	6	PRIOUT0B
7	PRIIN2	8	PRIOUT0
9	1WIRE	10	BUS7B
11	1VDD	12	BUS7
13	BECLKB	14	BUS6B
15	BECLK	16	BUS6
17	L1A	18	BUS5B
19	CALSR	20	BUS5
21	PRD2	22	BUS4B
23	PRIIN0	24	BUS4
25	FEMODE	26	BUS3B
27	PRD1	28	BUS3
29	BEMODE	30	BUS2B
31	CHMODE	32	BUS2
33	PARST	34	BUS1B
35	PRIOUT3B	36	BUS1
37	PRIOUT3	38	BUS0B
39	PRIIN3	40	BUS0
41	AGND	42	ODBVB
43	DVDD	44	ODBV
45	DVDD	46	GND
47	DVDD	48	FECLKB
49	GND	50	FECLK

Figure C.13: The SVX4 Chain Ports

JTAG_COMMON Port		
1	VCC	
2	GND	
3	TCK	
4	TDI	Connected to
5	TDO	Connected to
6	TMS	

JTAG_IN Port	
1	TDI

JTAG_OUT Port	
1	TDO

Figure C.14: The JTAG Ports

DEBUG Port			
1	SCL	1	I2C Clock
2	SDA	1	I2C Data
3	I2C_CS	1	I2C Chip Select.
4	CLKOUT	1	
5	QSPI_CLK	1	
6	QSPI_DIN	1	
7	QSPI_DOUT	1	
8	QSPI_CS[2:0]	3	
11	IRQ	1	

Figure C.15: The Debug Ports

1. I2C link to 1WIRE Master chips on all FEM modules
2. QSPI link to set and read internal registers of all FEM modules.

The debug port will be used for data taking during sensor testing when DCM and GTM are not available. The readout will be done using QSPI link to PCM at rate of 2 MBPS.

C.5 Zero Suppression and Data Compression

The SVX4 allows for on-chip zero suppression. However, the PHENIX DAQ is not designed to handle zero-suppression prior to the DCM because the pipelined architecture assumes a fixed length data packet. However, the use of this feature has significant advantages.

Fig. C.10 above shows that without zero suppression the event size from the brick will be 14448 bytes The compressor will remove the Channel ID bytes reducing the size to 7284 bytes.

Assuming 40 MHz 16-bit optical data link, this data will be sent in 92 μs, which does not fit the 40 μs ENDAT window. To handle this amount of data we will need triple number of DCM links. Fig. C.10 also shows that if we allow on-chip zero suppression, assuming 5% occupancy the data size will be reduced to 829 bytes, which is manageable by a single DCM.

We plan to further compress data using Huffman Coding of the zero-suppressed data inside FPGA. Based on experience at PHOBOS we expect a compression factor of 3. This leads to average data size from one brick of the order of 300 bytes.

C.6 Power and Control Module (PCM)

The Power and Control Module provides the low voltage power and bias voltage to FEMs. One PCM serves one half-disk of NCC, i.e. 7 bricks; it is located close to the detector. During

the initial stage of the project the PCM will also be used for slow control and monitoring of the front-end electronics as well as for remote configuration of the FPGAs. The module hosts a M5235BCC – a credit-card-size CPU board with ColdFire 64-bit 100 MHz CPU, 32 MB of memory, ethernet connection and I2C and QSPI ports. We have successfully tested the board running uCLinux and QUADROS+OPENTCP OS.

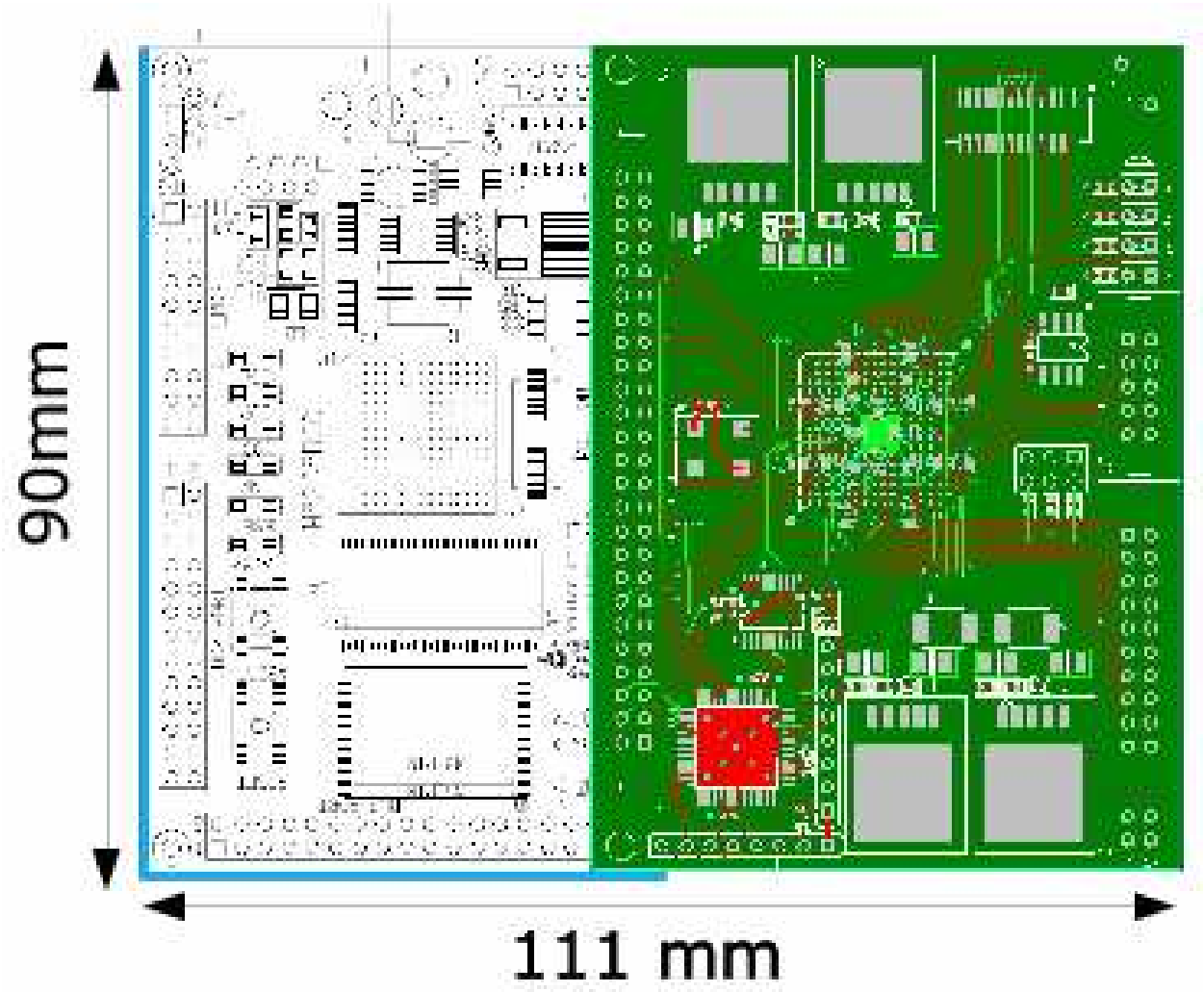

Figure C.16: Power Control Module

C.7 Si Strip Production, Testing, and Assembly

The Si strip wafers will be manufactured by a commercial vendor; ELMA of Russia, ON of Czech Republic are currently under consideration. At the vendor the wafers will undergo resistance and doping tests and then be diced into sensors. Further quality assurance (QA) includes IV and CV curves, laser pulse tests of each strip and sensor uniformity response.

The QA tests will be carried out at BNL and SBU (using facilities that are currently used for SVTX QA) and JINR(LPP) (Nikolai Zamiatin group).

The design and layout of all electronics boards will be done by JINR(LHE) (Sergey Basilev group). The manufacturing of prototype boards will be done at BNL ID and the volume production at a private company.

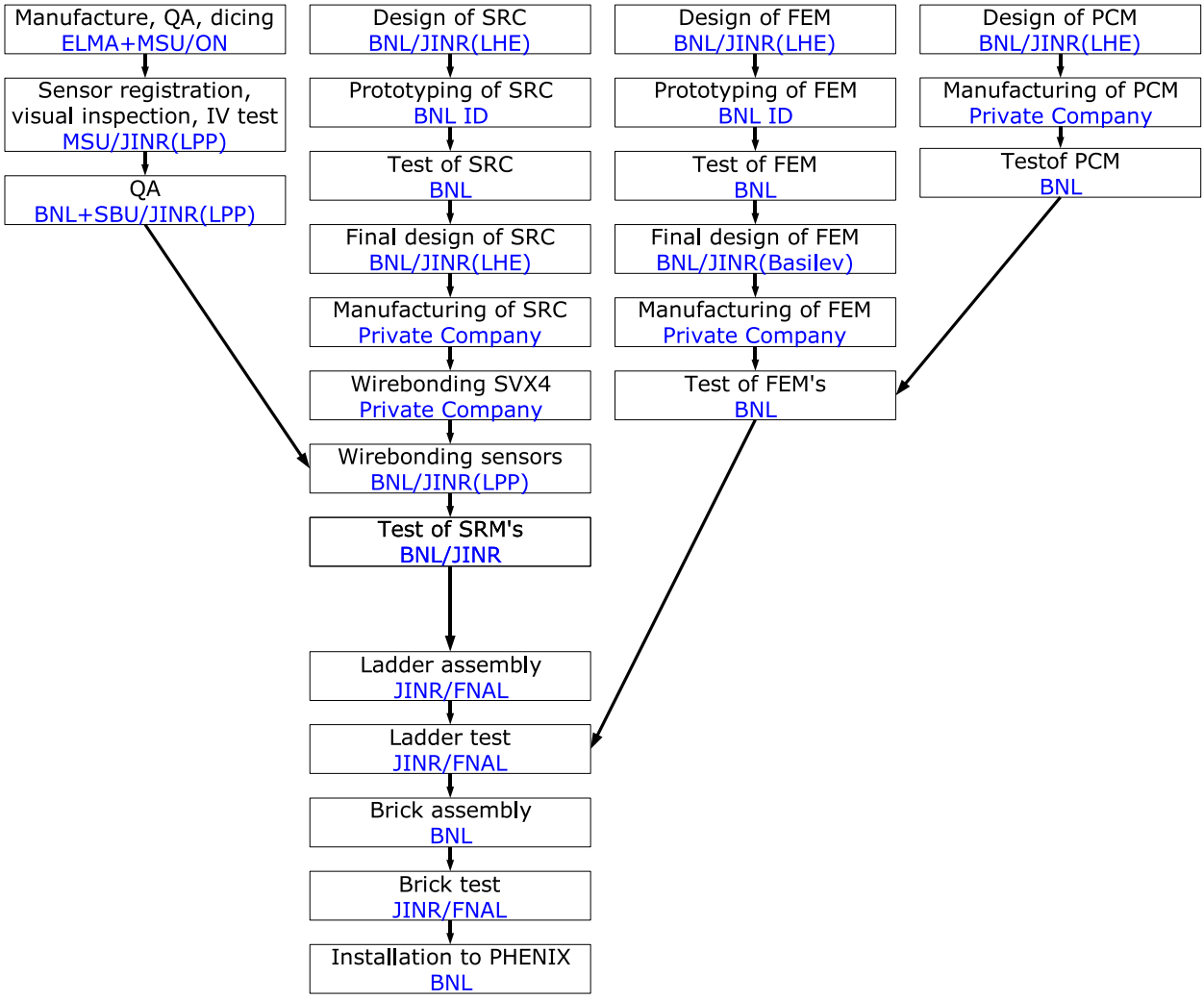

Figure C.17: Strip detector production flow chart.

C.8 Radiation Tolerance of Front-End Electronics

C.8.1 Inside the Calorimeter

The components, which are subject to radiation damages inside the calorimeter are the silicon sensors, SVX4 chips and 1Wire sensors (DS18B20X, DS2890, DS2450).

The estimates based on total energy flow simulation predict the Total Ionization Dose (TID) of 100 kRad (in Si) that correspond to the fluence of 3 x 10^{12} equivalent neutrons per cm^2 over the period of 10 years (assuming p+p interaction at 200 GeV with luminosity $\sim$ 2 x $10^{32} cm^{-2}$ s^{-1}). The leakage current for a 300μ sensor after this irradiation will be of the order of 120 μA/sensor. This corresponds to 0.5μA per strip. This current poses no problem provided the strip is AC decoupled from the SVX4 chip.

The SVX4 chip is radiation hardened and should sustain the expected TID. Little is known about the radiation tolerance of 1Wire devices; the usage of the 1Wire devices for ionization measurement in space (LAZIO experiment) has been reported The radiation tolerance of the 1Wire devices will be tested after completeness of the full prototype of readout chain.

C.8.2 Outside the Calorimeter

The components, which are subject to radiation damage outside the calorimeter are the components of the FEM boards: FPGA (Xilinx XC3S1000), optical transceiver and SerDes, clock oscillators and voltage regulators.

The TID estimation for this region for Au+Au collisions is obtained from [80] and is summarized in table 9.

	RHIC I	**RHIC II**
R = 53 cm	0.79 rad 2.4*10^7 cm^{-2}	7.9 rad 2.4*10^8 cm^{-2}
R = 250 cm	0.17 rad 5.1*10^6 cm^{-2}	1.5 rad 4.5*10^7 cm^{-2}

Figure C.18: Mean total ionizing dose (TID) for RHIC I and RHIC II fills, for two positions: 53 and 250 cm from the interaction region in rads/fill and equivalent neutrons per cm^2 per fill.

Assuming running periods of 30 weeks per year with 3 shifts per day, the expected dose for 10 years of running RHIC II will be of the order of 50 krad or 1.5 x 10^{12} n cm^{-2} (for 53 cm).

The ALICE collaboration presented results of the radiation tolerance tests of similar components in [81], which are summarized below.

- **: Clock Oscillators and Voltage Regulators.** The clock oscillators PL75108A, SDB0149N, CFPIQXO-71C, PLE5144A where tested. All the oscillators found to be tolerant to the gamma irradiation up to 100 krad. The voltage regulator of Linear Technology LT1663 family passed the tests.

- **Optical Transceiver and SerDes:** The all Small Form Factor (SFF) optical transceivers which have been tested (HFBR5910E, HFBR5921L, HFBR5920E, V23818-K305-L57, V23818-N305-B57) as well as SerDes (TLK2501, VSC7211) all passed the irradiation test with 10^{12} n cm^{-2}.

- **FPGA**

It was found that the cross section of bit flips in application memory is acceptable, but the cross section for errors in configuration memory is too high. Translated to 50 krad TID it corresponds to 12000 of lost configuration for SRAM-based FPGA (Xilinx Virtex II). The flash-based FPGA (ACTEL ProASIC+) did not show any degradation.

Therefore the only unacceptable tolerance we may expect is in the configuration memory of the SRAM-based FPGA. There are two solutions to that:

1. Use flash-based FPGA (ACTEL ProASIC+), which is little bit slower than Xilinx

2. Monitor the configuration error and reconfigure the FPGA when necessary, the expected rate of such reconfigurations is once per store.

List of Figures

List of Tables

References

[1] PHENIX, 1993. PHENIX Conceptual Design Report 1993 (PX20, BNL48922, internal report),.

[2] **PHENIX** Collaboration, K. Adcox *et. al. Nucl. Phys.* **A757** (2005) 184–283 [nucl-ex/0410003].

[3] J. D. Bjorken, *Energy loss of energetic partons in quark - gluon plasma: Possible extinction of high p(t) jets in hadron - hadron collisions*, 1982. FERMILAB-PUB-82-059-THY.

[4] M. Gyulassy and M. Plumer *Phys. Lett.* **B243** (1990) 432–438.

[5] X.-N. Wang, M. Gyulassy and M. Plumer *Phys. Rev.* **D51** (1995) 3436–3446 [hep-ph/9408344].

[6] X.-N. Wang and M. Gyulassy *Phys. Rev. Lett.* **68** (1992) 1480–1483.

[7] R. Baier, Y. L. Dokshitzer, S. Peigne and D. Schiff *Phys. Lett.* **B345** (1995) 277–286 [hep-ph/9411409].

[8] R. Baier, Y. L. Dokshitzer, A. H. Mueller and D. Schiff *Phys. Rev.* **C58** (1998) 1706–1713 [hep-ph/9803473].

[9] M. Gyulassy, P. Levai and I. Vitev *Phys. Rev. Lett.* **85** (2000) 5535–5538 [nucl-th/0005032].

[10] M. Gyulassy, P. Levai and I. Vitev *Nucl. Phys.* **B594** (2001) 371–419 [nucl-th/0006010].

[11] **PHENIX** Collaboration, K. Adcox *et. al. Phys. Rev. Lett.* **88** (2002) 022301 [nucl-ex/0109003].

[12] **PHENIX** Collaboration, K. Adcox *et. al. Phys. Lett.* **B561** (2003) 82–92 [nucl-ex/0207009].

[13] **PHENIX** Collaboration, S. S. Adler *et. al. Phys. Rev. Lett.* **91** (2003) 072301 [nucl-ex/0304022].

[14] **PHENIX** Collaboration, S. S. Adler *et. al. Phys. Rev.* **C69** (2004) 034910 [nucl-ex/0308006].

[15] **PHENIX** Collaboration, S. S. Adler *et. al. Phys. Rev. Lett.* **91** (2003) 072303 [nucl-ex/0306021].

[16] E. Wang and X.-N. Wang *Phys. Rev. Lett.* **89** (2002) 162301 [hep-ph/0202105].

[17] **PHENIX** Collaboration, S. S. Adler *et. al. Phys. Rev. Lett.* **91** (2003) 172301 [nucl-ex/0305036].

[18] T. Matsui and H. Satz *Phys. Lett.* **B178** (1986) 416.

[19] O. Kaczmarek, F. Karsch, P. Petreczky and F. Zantow *Phys. Lett.* **B543** (2002) 41–47 [hep-lat/0207002].

[20] M. Asakawa and T. Hatsuda *Phys. Rev. Lett.* **92** (2004) 012001 [hep-lat/0308034].

[21] S. Datta, F. Karsch, P. Petreczky and I. Wetzorke *Phys. Rev.* **D69** (2004) 094507 [hep-lat/0312037].

[22] C.-Y. Wong *Phys. Rev.* **C72** (2005) 034906 [hep-ph/0408020].

[23] F. Karsch *Eur. Phys. J.* **C43** (2005) 35–43 [hep-lat/0502014].

[24] **PHENIX** Collaboration, H. Pereira Da Costa nucl-ex/0510051.

[25] **NA50** Collaboration, M. C. Abreu *et. al. Phys. Lett.* **B521** (2001) 195–203.

[26] **NA60** Collaboration, R. Arnaldi *et. al. Eur. Phys. J.* **C43** (2005) 167–172.

[27] Y. V. Kovchegov, *Isotropization and thermalization in heavy ion collisions*, 2005.

[28] S. Mrowczynski *Acta Phys. Polon.* **B37** (2006) 427–454 [hep-ph/0511052].

[29] R. Venugopalan hep-ph/0511117.

[30] D. Kharzeev, E. Levin and K. Tuchin hep-ph/0602063.

[31] L. D. McLerran and R. Venugopalan *Phys. Rev.* **D49** (1994) 2233–2241 [hep-ph/9309289].

[32] L. D. McLerran and R. Venugopalan *Phys. Rev.* **D49** (1994) 3352–3355 [hep-ph/9311205].

[33] L. D. McLerran and R. Venugopalan *Phys. Rev.* **D50** (1994) 2225–2233 [hep-ph/9402335].

[34] H. Kowalski and D. Teaney *Phys. Rev.* **D68** (2003) 114005 [hep-ph/0304189].

[35] **New Muon** Collaboration, P. Amaudruz *et. al. Nucl. Phys.* **B441** (1995) 3–11 [hep-ph/9503291].

[36] D. F. Geesaman, K. Saito and A. W. Thomas *Ann. Rev. Nucl. Part. Sci.* **45** (1995) 337–390.

[37] D. M. Alde *et. al. Phys. Rev. Lett.* **64** (1990) 2479–2482.

[38] **NuSea** Collaboration, M. A. Vasiliev *et. al. Phys. Rev. Lett.* **83** (1999) 2304–2307.

[39] L. L. Frankfurt, M. I. Strikman and S. Liuti *Phys. Rev. Lett.* **65** (1990) 1725–1728.

[40] B. Z. Kopeliovich, J. Nemchik, I. K. Potashnikova, M. B. Johnson and I. Schmidt *Phys. Rev.* **C72** (2005) 054606 [hep-ph/0501260].

[41] D. Boer and W. Vogelsang *Phys. Rev. D* **69** (2004) 094025.

[42] C. Adloff *et. al. Eur. Phys. J.* **C19** (2001) 289–311.

[43] H. Lai *et. al. Eur. Phys. J.* **C12** (1999) 375–392.

[44] A. Martin, R. Roberts, W. Stirling and R. Thorne *Eur. Phys. J.* **C39** (2005) 155–161.

[45] M. Gluck, E. Reya, M. Stratmann and W. Vogelsang *Phys. Rev.* **D53** (1996) 4775–4786.

[46] Y. Goto *et. al. Phys. Rev. D* **69** (2004) 054021.

[47] E. Laenen, G. Sterman and W. Vogelsang *Phys. Rev. Lett.* **84** (2000) 4296–4299.

[48] E. Laenen, S. G. and W. Vogelsang *Phys. Rev. D* **63** (2001) 114018.

[49] J. Ashman *et. al. Nucl. Phys.* **B328** (1989) 1–35.

[50] G. Baum *et. al. Phys. Rev. Lett.* **51** (1983) 1261–1265.

[51] G. Bunce *et. al. Phys. Rev. Lett.* **36** (1976) 1113–1116.

[52] D. Adams *et. al. Phys. Lett. B* **265** (1991) 462–466.

[53] J. Adams *et. al. Phys. Rev. Lett.* **92** (2004) 171801.

[54] L. Bland hep-ex/0602012.

[55] L. C. Bland *et. al. Eur. Phys. J.* **C43** (2005) 427–435 [hep-ex/0502040].

[56] D. Sivers *Phys. Rev.* **D41** (1990) 83.

[57] J. Collins *Nucl. Phys.* **B396** (1993) 161.

[58] J. P. Ralston and D. E. Soper *Nucl. Phys.* **B152** (1979) 109.

[59] J. Qiu and G. Sterman *Phys. Rev. D* **59** (1998) 014004.

[60] A. Airapetian *et. al. Phys. Rev. Lett.* **84** (2000) 4047–4051.

[61] A. Airapetian *et. al. Phys. Rev. Lett.* **94** (2005) 012002.

[62] K. Abe *et. al.* `hep-ex/0507063`.

[63] J. Collins, S. Heppelmann and G. Ladinsky *Nucl. Phys.* **B420** (1994) 565.

[64] H. Collaboration `hep-ex/0512019`.

[65] P. Mulders and R. Tangerman *Nucl. Phys.* **B461** (1996) 197–237.

[66] A. Bacchetta, C. Bomhof, P. Mulders and F. Pijlman *Phys. Rev. D* **72** (2005) 034030.

[67] M. Anselmino *et. al. Phys. Rev. D* **73** (2006) 014020.

[68] A. Airapetian *et. al. Phys. Rev. D* **71** (2005) 012003.

[69] C. Bourrely and J. Soffer *Phys. Lett.* **B314** (1993) 132–138.

[70] P. Nadolsky and C.-P. Yuan *Nucl. Phys.* **B666** (2003) 35.

[71] M. Harrison, T. Ludlam and S. Ozaki *Nucl. Instrum. Meth.* **A499** (2003) 235–880.

[72] R. K. Seto `nucl-ex/0204003`.

[73] E. Iancu, A. Leonidov and L. McLerran `hep-ph/0202270`.

[74] L. McLerran *Pramana* **60** (2003) 575–786 [`hep-ph/0202025`].

[75] I. Golutvin *et. al.*, 1992. A Silicon Hadron Calorimeter module operated in a strong magnetic field with VLSI read out for LHC, CERN-DRDC-91-54, CERN-DRDC-P-34.

[76] J. Adams *et. al.*, 2001. The Silicon Matrix as a Charge Detector for the ATIC Experiment, Instrum. Exp. Tech. 44, 455-461, 2001, Prib.Tekh.Eksp. 2001 N4, 38-44, 2001.

[77] V. Bonvicini *et. al. Nucl. Instrum. Meth.* **A518** (2004) 186–187.

[78] R. Wigman, *Calorimetry, Energy Measurement in Particle Physics*. Oxford Science Publications, Oxford University Press, Great Clarendon Street, Oxford OX2 6DP, 2000.

[79] K. Golec-Biernat and M. Wusthoff *Phys. Rev.* **D59** (1999) 014017 [`hep-ph/9807513`].

[80] S. Skutnki, 2005. A scalable analytic model for single event upsets in radiation-hardened field programmable gate arrays in the PHENIX interaction region.

[81] E. Denes *et. al.*, 2004. ALICE DDL Radiation Tolerance Tests for the FPGA Configuration Loss.